Opto-electronic characterization of polycrystalline $CuInS_2$ and $Cu(In,Ga)S_2$ absorber layers by photoluminescence

Von der Fakultät für Mathematik und Naturwissenschaften der
Carl von Ossietzky Universität Oldenburg
zur Erlangung des Grades und Titels eines

Doktors der Naturwissenschaften
(Dr. rer. nat.)

angenommene Dissertation
von

Florian Heidemann
geboren am 25.09.1979 in Dinklage

Oldenburg, 29. September 2011

Gutachter:

Betreuender Gutachter: Prof. Dr. Gottfried H. Bauer (Universität Oldenburg)
Zweite Gutachterin: Prof. Dr. Susanne Siebentritt (Universität Luxemburg)

Tag der Disputation: 13.12.2010

Abstract

Photoluminescence (PL) is an established method to characterize the opto-electronic properties of solar cell absorber layers. With the help of Planck's generalized law it is in principle possible to determine the quasi-Fermi level splitting — which is the upper limit of the open circuit voltage V_{oc} — and the absorption coefficient of a solar cell before its actual completion. For large-scale measurements (mm/cm regime) this is valid for absorber layers with lateral homogeneous properties, however it is not directly transferable to polycrystalline semiconductors due to laterally fluctuating opto-electronic and structural parameters.

The lateral fluctuations in opto-electronic properties of polycrystalline $\mathrm{Cu(In_{1-\xi}Ga_{\xi})S_2}$ have been analyzed (e.g. with respect to fluctuations in quasi-Fermi level splitting, optical band-gap and sub band-gap absorbance) by measuring laterally and spectrally resolved PL on the μm-scale and providing the transition towards macroscopic PL measurements on the mm-scale. To give a comprehensive characterization, surface roughness and optical properties have been studied and methods for feature extraction have been applied.

On the microscopic scale variations in the quasi-Fermi level splitting $\triangle_{x,y}E_{Fnp}$ of about 38 meV ($\mathrm{CuInS_2}$) and 53 meV ($\mathrm{Cu(In,Ga)S_2}$) have been found. From local absorbance spectra extracted from PL measurements on $\mathrm{Cu(In,Ga)S_2}$ fluctuations in the optical band-gap E_{opt} with a full width at half maximum of $\mathrm{FWHM}_{E_{opt}} \approx$ 80 meV could be extracted, whereas band-gap fluctuations in $\mathrm{CuInS_2}$ are found to be negligible. Thus band-gap fluctuations seem to be mainly caused by a varying gallium (Ga) content. Furthermore, regions with higher E_{opt} and with it a potential higher Ga content, show a higher quasi-Fermi level splitting. As a major limiting factor for the local quasi-Fermi level splitting E_{Fnp} the local density of deep defects could be identified.

Due to low luminescence yields of $\mathrm{Cu(In_{1-\xi}Ga_{\xi})S_2}$ under AM1.5 equivalent conditions, the transition from microscopic towards macroscopic PL measurements — which allow a calibration of the experimental setup for absolute photon fluxes and with it the extraction of absolute E_{Fnp} — proves difficult. By non-linear superposition of several PL centers with fluctuations $\triangle_{x,y}E_{Fnp}$, the quasi-Fermi level splitting $E_{Fnp,macro}$ extracted from macroscopic PL measurements is overestimated. A study for gaussian shaped variations in $\triangle_{x,y}E_{Fnp}$ with standard deviation $\sigma_{E_{Fnp}}$ revealed an overestimation by the factor $\sigma^2_{E_{Fnp}}/(2kT)$. However, absolute E_{Fnp} can only be extracted with an inaccuracy higher than the error caused by incorrect averaging.

Kurzdarstellung

Photolumineszenz (PL) hat sich als Charakterisierungsmethode für Absorber von Solarzellen etabliert, durch die Formulierung vom verallgemeinertem Planckschen Strahlungsgesetz lässt sich prinzipiell die Obergrenze der offenen Klemmenspannung V_{oc} sowie die Absorption einer vollständig prozessierten Zelle unter Standardbeleuchtung (AM1.5) noch vor ihrer Fertigstellung bestimmen. Für großflächige Messungen (mm/cm-Skala) gilt dies jedoch vornehmlich für homogene Absorberschichten, auf die Analyse polykristalliner Halbleiter lässt sich dieser Ansatz aufgrund der lateral variierenden opto-elektronischen und strukturellen Eigenschaften nicht eins zu eins übertragen.

Durch die lateral und spektral aufgelöste Messung der Photolumineszenz mit sub-Mikrometer Auflösung sowie den Übergang zur makroskopischen Messung (mm-Skala) sind hier die lateralen Fluktuationen in den Eigenschaften des polykristallinen Halbleiters $Cu(In_{1-\xi}Ga_{\xi})S_2$ quantifiziert und hinsichtlich ihres Anregungszustandes (Aufspaltung der quasi-Fermi Niveaus E_{Fnp}) und ihrer Absorption (Variation in der optischen Bandlücke, Absorption über Defektzustände usw.) untersucht worden. Um eine vollständige Charakterisierung zu erhalten wurden zusätzlich Oberflächenrauhigkeiten und optische Eigenschaften analysiert sowie Methoden der Merkmalextraktion angewandt.

Auf mikroskopischer Skala wurden für Messungen mit einer Anregungdichte von 10^4 AM1.5 äquivalent Schwankungen in der quasi-Fermi Niveau Aufspaltung $\triangle_{x,y}E_{Fnp}$ von 38 meV ($CuInS_2$) bzw. 53 meV ($Cu(In,Ga)S_2$) gemessen. Über die Absorption konnten aus den PL Messungen an $Cu(In,Ga)S_2$ Fluktuationen in der optischen Bandlücke von $\mathrm{FWHM}_{E_{opt}} \approx 80\,\mathrm{meV}$ bestimmt werden, wohingegen die untersuchten $CuInS_2$ Proben so gut wie keine Bandlückenfluktuationen aufwiesen. Dies legt die Vermutung nahe, dass Änderungen in der Bandlücke hauptsächlich durch variierende Ga-Konzentration hervorgerufen werden. Absorberregionen mit hoher Ga-Konzentration wiesen zudem eine erhöhte quasi-Fermi Niveau Aufspaltung E_{Fnp} auf. Als wesentliche Begrenzung der lokalen E_{Fnp} konnte die lokale Dichte von tiefen Defekten ermittelt werden.

Generell gestaltet sich der Übergang zu Messungen auf makroskopischer Skala — für die eine Kalibrierung auf absolute Photonenflüsse und somit die Extraktion absoluter E_{Fnp} möglich ist — aufgrund geringer Lumineszenzausbeuten unter AM1.5 äquivalenten Bedingungen schwierig. Absolute E_{Fnp} lassen sich nur mit großem Fehlerbereich angeben, so dass die Überschätzung welche durch nicht-lineare

Mittellung bei Messungen auf makroskopischer Skala hervorgerufen werden geringer ausfällt als die Fehlerbereiche.

Contents

List of Figures

1. Introduction

By higher efficiencies, lower production costs and increasing climate changes photovoltaics gain more and more importance as a renewable energy source. Especially thin film absorber layers offer a high potential of cost efficient production as well as reaching high conversion efficiencies. A huge part in this progress is made by chalcopyrite based polycrystalline Cu(In,Ga)Se_2 (CIGSe) thin film solar cells with efficiencies of up to 20% [1,2]. The sulphured counterparts $CuInS_2$ (CIS) or Cu(In,Ga)S_2 (CIGS) on the other hand, are presently being considered as an alternative providing a larger band gap that more suits the solar spectrum and giving the potential of a nominal higher open circuit voltage [3, 4]. However solar cell efficiencies achieved with CIGS absorber layers have only reached $\eta \approx 13\%$ so far [5]. Because knowledge about these absorber layers is still limited a profound characterization is mandatory. Analogously to CIGSe, $Cu(In_{1-\xi}Ga_{\xi})S_2$ thin films show a high degree of lateral inhomogeneities in optical, electronic and structural properties caused by their manufacturing process which lower the efficiency of cells [6–8].

The measurement of photoluminescence (PL) of semiconductors provides various opto-electronic characterization possibilities [9–12]. A fundamental approach to theoretically describe the emitted PL is made by Planck's generalized radiation law [13], which — among others — gives access to the quasi-Fermi level splitting and with it to the upper limit of the open circuit voltage V_{oc} that can be reached in a diode. For crystalline semiconductors with homogeneous absorber parameters, e.g. silicon, the application of Planck's generalized law is well established and has been extensively studied [14–18]. However, when analyzing polycrystalline absorber layers like chalcopyrite $Cu(In_{1-\xi}Ga_{\xi})S_2$, spatially fluctuating absorber properties have to be taken into account, leading to the consequence of a laterally resolved PL characterization. In some works this has been realized on the basis of Cu(In,Ga)Se_2 absorbers [8,19,20]. Lateral band-gap fluctuations of about $\mathrm{FWHM}_{E_{opt}} \approx 11\,\mathrm{meV}$ and fluctuations in the local quasi-Fermi level splitting of about $\mathrm{FWHM}_{E_{Fnp}} \approx 13\,\mathrm{meV}$ to $18\,\mathrm{meV}$ have been found on the micrometer scale [21]. Beyond the microscopic characterization the question arises, how lateral fluctuations in opto-electronic absorber properties influence macroscopic measured PL data sets and the performance of cells. The latter has been studied in terms of band-gap fluctuations which have been found to decrease the maximum achievable cell efficiency [22].

The aim of this thesis is to apply laterally resolved PL characterization to $\mathrm{Cu(In_{1-\xi}Ga_{\xi})S_2}$ absorber layers where a special focus is given to the absorber specific properties of $\mathrm{Cu(In_{1-\xi}Ga_{\xi})S_2}$. A major topic will be the analyses of the local absorbance of the film, as both CIS and CIGS absorber layers have a pronounced defect spectrum. The PL interpretation of Ga doped samples is hampered by an additional band-gap gradient over the absorber thickness. Finally a transition towards macroscopic measured PL is made and the influence of microscopic scale fluctuations in opto-electronic absorber properties on macroscopic detected PL spectra is studied.

2. Polycrystalline $Cu(In_{1-\xi}Ga_{\xi})S_2$

Besides $Cu(In,Ga)Se_2$ — whose band-gap is below the optimum match to the solar spectrum — the sulphured counterparts $CuInS_2$ and $Cu(In,Ga)S_2$ are considered as alternatives. The higher band-gap of $Cu(In_{1-\xi}Ga_{\xi})S_2$ offers the potential of a nominal higher open circuit voltage. However cell efficiencies have only reached 11 % ($CuInS_2$) or 13 % ($Cu(In,Ga)S_2$) so far [4, 23–25].

In the following chapter a short overview on chalcopyrite absorber and the samples analyzed in this work will be given. The main attention is dedicated to the surface contour of the film as well as its reflectivity and to the transparent conductive oxide (TCO), that is, to the ZnO layer. For a more detailed description on $Cu(In_{1-\xi}Ga_{\xi})S_2$ the reader is referred to the literature [19, 26, 27].

Figure 2.1 shows a sketch of the $Cu(In_{1-\xi}Ga_{\xi})S_2$ absorber layers analyzed. The back contact is realized by a molybdenum coated soda lime glass. The average thickness $\overline{d}$ of the $Cu(In_{1-\xi}Ga_{\xi})S_2$ absorber amounts to 2 µm to 3 µm and includes a 50 nm to 80 nm CdS passivation layer. The pn-junction is nominally formed between the p-type $Cu(In_{1-\xi}Ga_{\xi})S_2$ and n-type CdS and i-ZnO/ZnO:Al TCO layer with a band-gap of about 3.3 eV and a thickness of 500 nm. The thin films are produced by rapid thermal processing (RTP) of a precursor stack in sulfur atmosphere, followed by KCN etching of the secondary CuS phase that forms at the surface during the

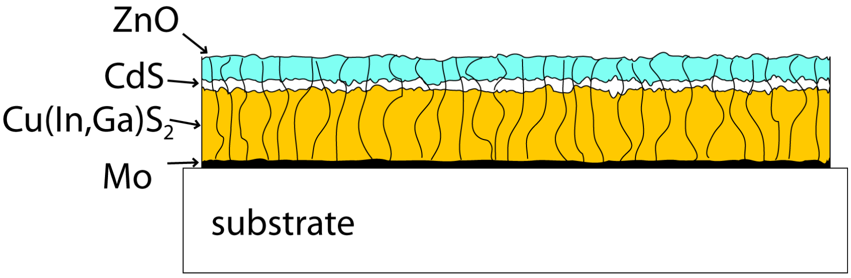

Figure 2.1.: Sketch of a $Cu(In,Ga)_2$ absorber layer deposited on a molybdenum coated glass substrate.

annealing procedure and a chemical bath deposition of CdS[1].

Polycrystalline $CuInS_2$ is a p-type I-III-VI_2 compound semiconductor that crystallizes in the chalcopyrite lattice. It has a direct band-gap E_g of approximately 1.53 eV [28] with an absorption coefficient α that can be described by the absorption of an ideal direct semiconductor

$$\alpha(\hbar\omega) = \frac{a}{\hbar\omega}\sqrt{\hbar\omega - E_g} \qquad \text{for } \hbar\omega > E_g, \tag{2.1}$$

with a in the range of $10^5(\text{eV})^{1/2}\text{cm}^{-1}$ [29]. In $Cu(In_{1-\xi}Ga_{\xi})S_2$ the band-gap depends on gallium content, where $CuGaS_2$ (for $\xi = 1$) has a band-gap of 2.5 eV [27, 30]. The band-gap of the mixed phase depends approximately linearly on ξ and is given in good approximation given by [6, 27]

$$E_g(\xi) \approx 1.5 \text{ eV}(1-\xi) + 2.5 \text{ eV}\xi. \tag{2.2}$$

The Cu(In,Ga)S_2 samples used in this work have a depth-dependent gallium content over the absorber thickness. Most of the Ga is concentrated close to the Mo back contact whereas the indium rich regimes are found in the top layer of the thin film [6].

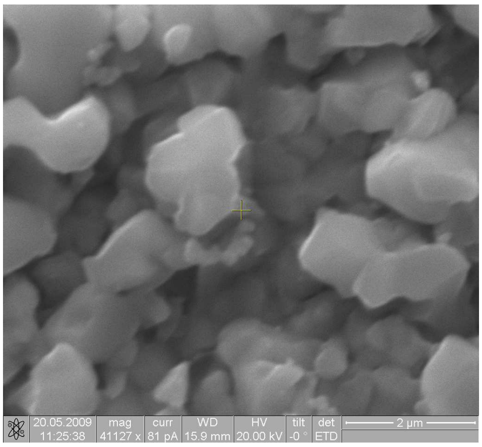

Figure 2.2.: SEM image of the surface of a Cu(In,Ga)S_2 absorber layer. ($V_{ac} = 20$ kV, $I_{SEM} = 81$ pA (sample from the same batch as Cu(In,Ga)S_2 in table 2.1).

Figure 2.2 shows a scanning electron microscope (SEM) image of 7.5 µm × 7.5 µm of a Cu(In,Ga)S_2 surface. A high variation in the absorber thickness is revealed,

---

[1] Since the preparation of absorber layers is not part of this work it is not described here in detail, more information on the growth process of layers can be found in [3, 4, 24, 26, 27].

with grain sizes in the range of a few microns. Since the data set contained in such a small image is statistically not representative, atomic force microscopy (AFM) measurements have been carried out to characterize the sample topography and its grain sizes. These measurements are presented in section 2.2.

In chapter 5.2 transparent $Cu(In_{1-\xi}Ga_{\xi})S_2$ samples deposited on soda lime glass without Mo are studied. It has to be noted, that these samples grow differently due to the lack of the Mo layer, which acts as a partial diffusion barrier between absorber layer and glass. Table 2.1 lists solar cell parameters with absorber layers from the same batch as those analyzed in this work.

Table 2.1.: Absorber layers analyzed in this work. Cell area 0.5 cm^2. All layers have been prepared by and cell characteristics have been measured at the *Helmholtz Zentrum Berlin*

sample	V_{oc} (mV)	J_{sc} (mA cm^{-2})	FF (%)	η (%)
$CuInS_2$	679 ± 9	20.5 ± 0.3	58.4 ± 1.9	8.1 ± 0.4
$Cu(In,Ga)S_2$ a	700	230	50	9
$Cu(In,Ga)S_2$ b	794	214	65	11

2.1. Transparent Front Contact — ZnO

For the study of the luminescence of an absorber coated with a ZnO:Al TCO layer influences of this layer on the detected signal have to be known. Figure 2.3a shows transmission (blue) and reflection (green) of a ZnO layer deposited on a glass substrate[2]. Only a small spectral range has a high transmittance of about 80%. Since the band-gap amounts to 3.4 eV, photons with $\lambda \lesssim 365\,\text{nm}$ are absorbed (considering a thickness of approximately 490 nm). For wavelengths $\lambda \gtrsim 1000\,\text{nm}$ the transmission decreases due to free carrier absorption of ZnO. Spectral transmission as well as reflection show interference patterns. With the analysis software *Diplot* the transmission spectrum can be reproduced. Besides band-gap $E_g \approx 3.4\,\text{eV}$, thickness $d \approx 490\,\text{nm}$ and index of refraction $n(\hbar\omega \to 0) \approx 2.0$, the absorption coefficient α as seen in figure 2.3b can be extracted. The absorption of ZnO shows a dependence of $\alpha \propto \lambda^m$ with $m = 3.4$ in the long wavelength regime. Although the Drude Theory

---

[2] The ZnO layer has been deposited at the *Helmholtz Zentrum Berlin*

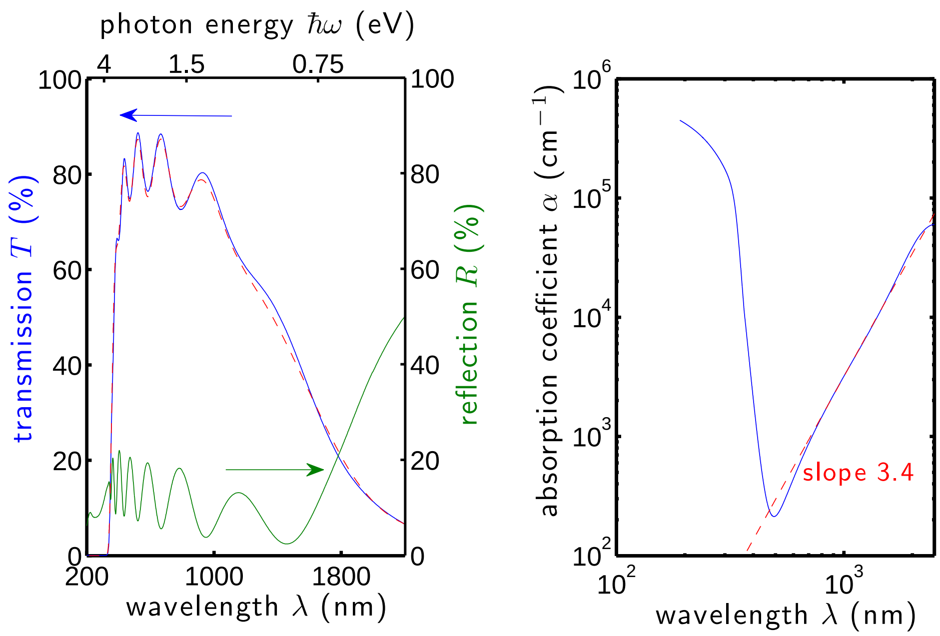
(a) Transmittance and Reflectance

(b) Absorption Coefficient

Figure 2.3.: Optical properties of ZnO, 2.3a reflection R (green), transmission (blue) and modeled transmission (dashed red). 2.3b extracted absorption coefficient α. The model yields a thickness $d \approx 490\,\text{nm}$, a band-gap $E_g \approx 3.4\,\text{eV}$ and an index of refraction $n(\hbar\omega \to 0) \approx 2.0$.

predicts an exponent of $m = 2$ for free carrier absorption, more generalized models which consider scattering mechanisms like acoustical phonon scattering, longitudinal phonon scattering or ionized impurity scattering yield exponents $m = (1.5 - 3.5)$ depending on the type of approximation [31–34]. The exponent $m = 3.4$ suggests ionized impurity scattering which corresponds to the strong Al-doping.

To exclude influences of ZnO-absorption on the PL measurements were carried out on absorber layers without ZnO.

2.2. Topography and Structure Sizes

When analyzing optoelectronic properties, the surface contour of the samples — e.g. grain sizes, surface roughness — which may have a non negligible influence on the photoluminescence signal have to be taken into account.

To get a statistically representative data set of the surface contour, atomic force microscopy (AFM) measurements with a scan area of 60 µm × 60 µm have been performed (see figures 2.4a and 2.4b). The surface profiles confirm the high surface roughness from the SEM image shown above. Both samples have similar grain sizes in the range of a few microns. The histograms of the height distribution show a full width at half maximum (FWHM) of 800 nm ± 20 nm for $CuInS_2$ and 700 nm ± 17 nm for $Cu(In,Ga)S_2$. A quantitative analysis of structure sizes can be carried out by the Minkowski opening procedure described in appendix C. For both sample types ($CuInS_2$ and $Cu(In,Ga)S_2$) structure sizes between 2 µm – 3 µm occur, with growing diameter (up to 4 µm) towards lower heights h. A correlation between both opening diagrams can be calculated according to

$$\begin{aligned} r(A,B) &= \frac{\sum_{n,m}\left[\left(A_{n,m}-\overline{A}_w\right)w_{A_{n,m}}\left(B_{n,m}-\overline{B}_w\right)w_{B_{n,m}}\right]}{\sqrt{\sum_{n,m}\left[\left(A_{n,m}-\overline{A}_w\right)w_{A_{n,m}}\right]^2\sum_{n,m}\left[\left(B_{n,m}-\overline{B}_w\right)w_{B_{n,m}}\right]^2}} \\ \forall &\quad A_{n,m}, B_{n,m} \neq 0 \end{aligned} \tag{2.3}$$

with weighting factor $w_{A_{n,m}} = \frac{A_{n,m}}{\sum_{n,m} A_{n,m}}$ and weighted arithmetic average $\overline{A}_w = \frac{\sum_{n,m} w_{A_{n,m}} A_{n,m}}{\sum_{n,m} w_{A_{n,m}}}$. Hence events are weighted with their frequency of occurrence, furthermore events with indices n, m for which $A_{n,m} = 0$ or $B_{n,m} = 0$ are also not considered in the calculation. The openings of $CuInS_2$ and $Cu(In,Ga)S_2$ (shown in figure 2.4e and 2.4f) have a correlation coefficient $r = 0.663$ which reflects the slightly smaller height variations in $Cu(In,Ga)S_2$. The grain sizes show a log-normal distribution (details can be found in appendix B), which corresponds to distributions found on $Cu(In,Ga)Se_2$ and other thin films [35, 36].

Since SEM measurements of $Cu(In_{1-\xi}Ga_{\xi})S_2$ cross sections have shown the formation of cavities between $Cu(In_{1-\xi}Ga_{\xi})S_2$ absorber layer and Mo back contact [6], which may have a non negligible influence on cell performance and on the PL signal — e.g. contributions to the variation in absorber thickness and contact to the Mo layer which may have an influence on carrier collection and recombination — the surface contour of the rear surface is also analyzed here. Figure 2.5 shows analogously to the front side, AFM topology, histogram and opening of the rear surface of $CuInS_2$ and $Cu(In,Ga)S_2$ films which have been detached from the Mo layer. Both

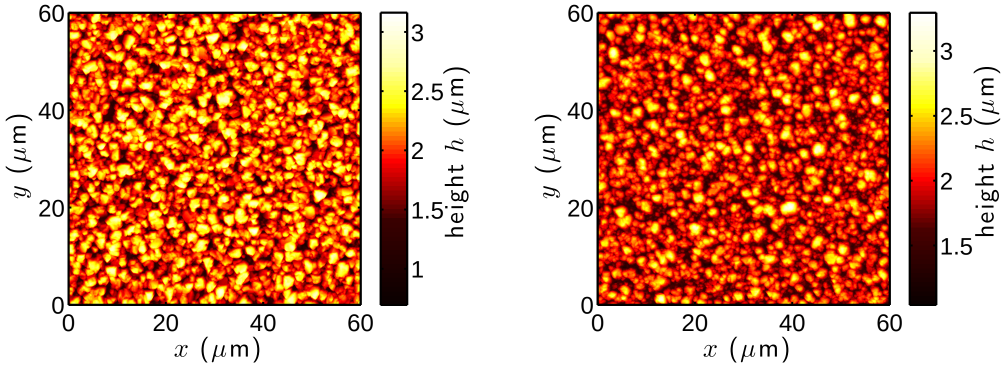
(a) Surface contour CuInS$_2$

(b) Surface contour Cu(In,Ga)S$_2$

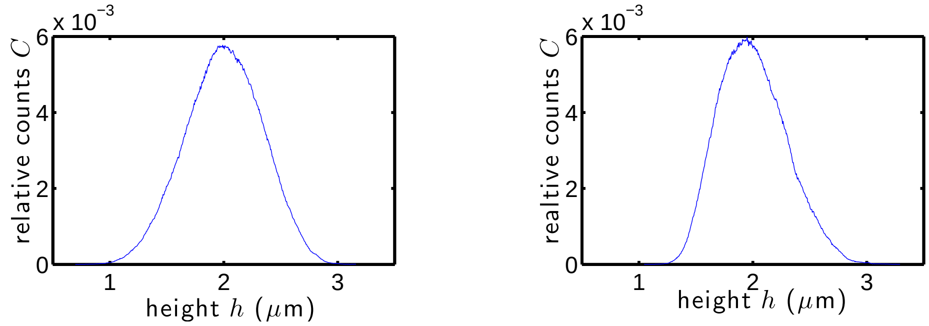
(c) Histogram CuInS$_2$

(d) Histogram Cu(In,Ga)S$_2$

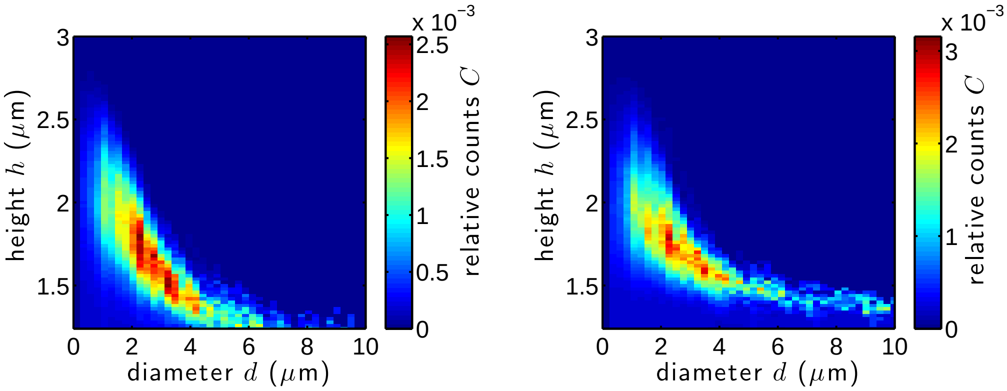
(e) Opening CuInS$_2$

(f) Opening Cu(In,Ga)S$_2$

Figure 2.4.: AFM measurements of a CIS and CIGS sample (figure 2.4a and 2.4e). Measurements have been carried out in a *WiTec* α-SNOM setup in pulsed force mode. Figure 2.4c and 2.4d show the corresponding histograms and 2.4e, 2.4f the opening diagrams (see appendix C). (samples from the same batch as CuInS$_2$ and Cu(In,Ga)S$_2$ a in table 2.1)

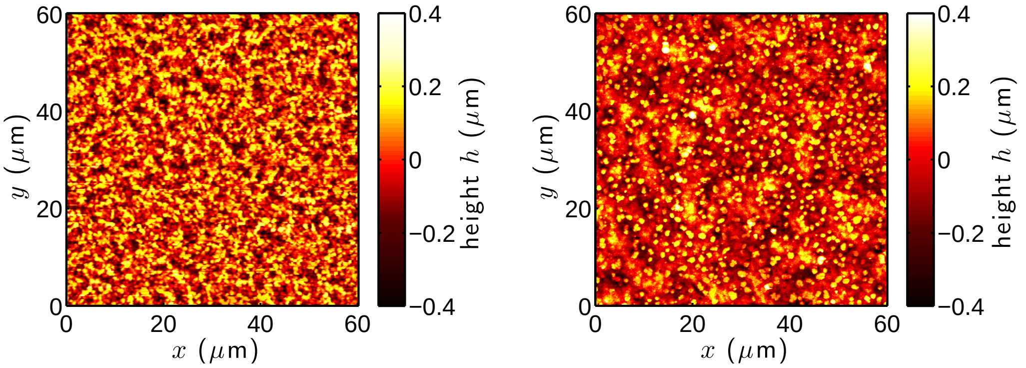

(a) Surface contour of rear surface $CuInS_2$

(b) Surface contour of rear surface $Cu(In,Ga)S_2$

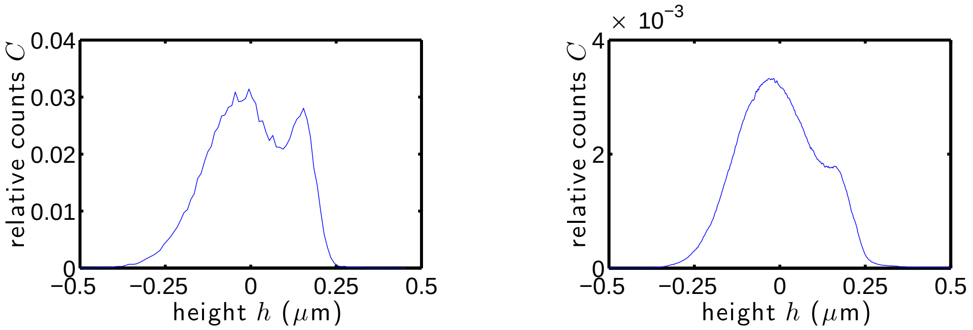

(c) Histogram $CuInS_2$

(d) Histogram $Cu(In,Ga)S_2$

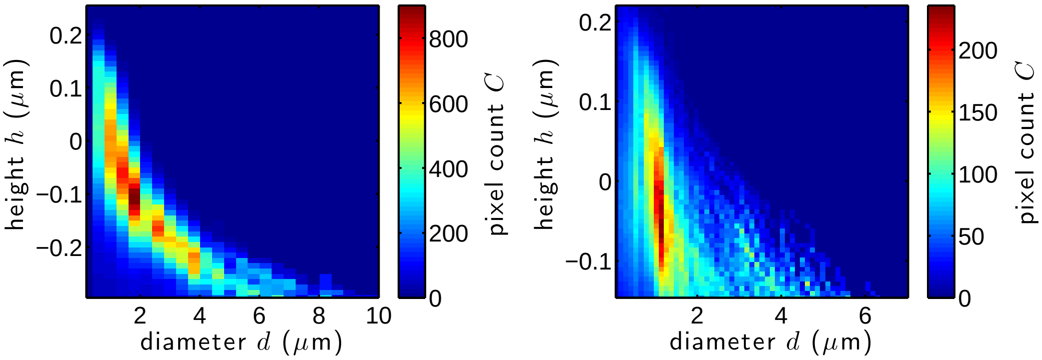

(e) Opening $CuInS_2$

(f) Opening $Cu(In,Ga)S_2$

Figure 2.5.: Surface contour of the rear surface of $CuInS_2$ and $Cu(In,Ga)S_2$ films which have been detached from the Mo layer (figure 2.5a and 2.5e). 2.5c and 2.5d show the corresponding histograms and 2.5e and 2.5f the opening diagrams.

$CuInS_2$ and Cu(In,Ga)S_2 (figures 2.5a and 2.5c) show significantly smaller structures and a smoother surface compared to the front side. The histograms (2.5c and 2.5d) reveal height variations with $\mathrm{FWHM}_{\triangle h} \approx 345\,\mathrm{nm}$ ($CuInS_2$) and $\mathrm{FWHM}_{\triangle h} \approx 320\,\mathrm{nm}$ (Cu(In,Ga)S_2). A second difference between front and rear side emerges from the form of the histograms, especially the $CuInS_2$ sample shows two superimposed gaussian distributions whereas the Cu(In,Ga)S_2 sample shows a shoulder. The origin of this distribution could not be identified but may be due to the removal from the Mo layer. Since the Mo layer is very smooth — $\mathrm{FWHM}_{Mo} < 10\,\mathrm{nm}$ — Mo fragments on the backside of the $Cu(In_{1-\xi}Ga_{\xi})S_2$ films or the other way around ($Cu(In_{1-\xi}Ga_{\xi})S_2$ on Mo) can be excluded. The opening diagrams shown in 2.5e and 2.5f clearly identify smaller structures than on the front side. In the case of $CuInS_2$ with a diameter of 1 µm – 2 µm and in the case of Cu(In,Ga)S_2 column like structures with a diameter of 1 µm.

To control the statistical representativity of the scanned area, AFM measurements have been carried out at three different sample positions. For each scan the openings have been calculated and correlated with one another according to eq. (2.3). Thereafter scan areas have been successively reduced and openings recalculated to correlate the different openings again and get a minimum scan area necessary to include statistically representative data sets. Figure 2.6 shows the correlation coefficients r versus scan area s. For large scan areas the correlation coefficient saturates around[3] $r \approx 0.8$. Below a scan area of about $900\,\mu\mathrm{m}^2$ or $30\,\mu\mathrm{m} \times 30\,\mu\mathrm{m}$ (dashed line in figure 2.6) the correlation coefficient r decreases strongly. Thus the underlying surface contour data set is no longer statistically representative if a scan area of $900\,\mu\mathrm{m}^2$ or less is used.

2.3. Macroscopic Optical Properties

Spectral reflection and — in the case of “transparent” samples, without a Mo back contact — transmission on the macroscopic scale have been measured with a *Cary 5E* spectrophotometer. Although an integrating sphere has been used, measurements turned out to be strongly influenced by scattering caused by the high surface roughness.

Figure 2.7 shows the reflection of a $CuInS_2$ (red) and a Cu(In,Ga)S_2 (blue) sample.

---

[3] It has to be noted that an ideal case of full correlation $r = 1$ can only be expected for infinitely large scan areas or correlations $r(A, A)$ — that is a correlation of the opening with itself. Furthermore noise reduces the correlation coefficient.

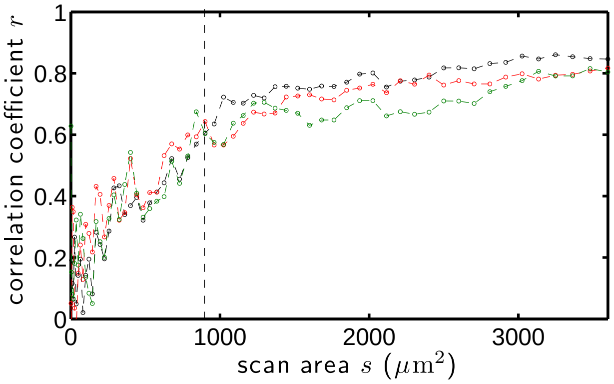

Figure 2.6.: Representativity of scan area, correlation coefficient r between openings of AFM scans at different sample positions for artificial reduced scan size s.

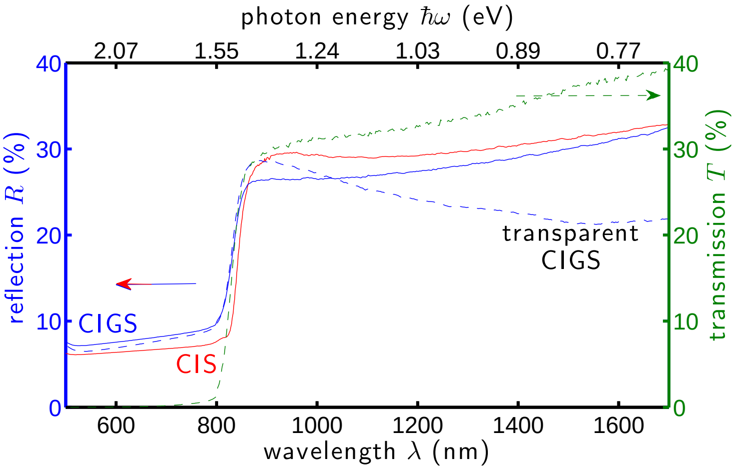

Figure 2.7.: Reflection of a $CuInS_2$ (red) and a $Cu(In,Ga)S_2$ (blue) sample, the dashed lines are reflection and transmission of a CIGS sample without Mo back contact.

Owing to high surface roughness interferences — as found in Cu(In,Ga)Se$_2$ and other thin films [21, 37] — are averaged out. Above the band-gap ($\hbar\omega > E_g$) at around 1.5 eV the reflection amounts to about 7% (CuInS$_2$) and 8% (Cu(In,Ga)S$_2$). Below the band-gap ($\hbar\omega < E_g$) it is about 30% and increases towards lower photon energies $\hbar\omega$ (or higher wavelengths λ). Due to the lack of the highly reflective Mo back contact the reflection of the transparent sample (dashed blue) in the low energy regime is considerably lower. The transmission (dashed green) shows a similar behavior and increases to about 40% in the long wavelength regime. Due to high absorption no transmission beneath the band-gap at around 1.5 eV can be measured.

A more detailed analysis of microscopic scale transmission and superposition of laterally varying absorbances A will be presented in chapters 5.2.2 and 3.1.1.

3. Photoluminescence of Polycrystalline Absorbers

In this chapter a brief overview on the theoretical principals of steady state photoluminescence from semiconductors will be given and applied on polycrystalline absorbers. For a more profound description of the theoretical background the reader is referred to literature and recent publications [9, 17, 19, 38].

3.1. Planck's Generalized Radiation Law

In an illuminated semiconductor the absorption of photons with an energy above the band-gap energy E_g creates additional electrons and holes. The energy distribution of these charge carriers in the energy bands differs from the distribution in the dark state and depends on the energy of absorbed photons. By emission and absorption of phonons the energy distribution changes rapidly and after a relaxation time of about 10^{-12} s charge carriers have a mean kinetic energy of $3/2 \cdot kT$ and a distribution that can be described by the Fermi-distribution.

The increased electron density n in the illuminated state of a semiconductor leads to a Fermi-energy $E_F = E_C - kT \ln \frac{N_C}{n}$ closer to the conduction band, where E_C is the lower edge of the conduction band and N_C is the effective density of states of the conduction band. On the other hand, because of hand the increased hole density p the Fermi-energy also has to move closer to the valence band $E_F = E_V + kT \ln \frac{N_V}{p}$, with the upper edge of the valence band E_V and the effective density of states of the valence band N_V. The solution to this inconsistency are two Fermi distributions, one for electrons with a Fermi-energy E_{Fn} and one for holes with a Fermi-energy E_{Fp} [13]. The density of electrons in the conduction band is given by (Boltzmann approximation)

$$n = N_C \exp\left(-\frac{E_C - E_{Fn}}{kT}\right), \tag{3.1}$$

that of holes in the valence band by

$$p = N_V \exp\left(-\frac{E_{Fp} - E_V}{kT}\right). \tag{3.2}$$

Therefore

$$\begin{aligned} np &= N_C N_V \exp\left(-\frac{E_C - E_V}{kT}\right)\exp\left(-\frac{E_{Fn} - E_{Fp}}{kT}\right) \\ &= n_i^2 \exp\left(\frac{E_{Fn} - E_{Fp}}{kT}\right). \end{aligned} \tag{3.3}$$

The distribution of electrons and holes in the illuminated state is accordingly given by the splitting of the quasi-Fermi levels which equals the chemical potential of the electron-hole ensemble $\mu_{eh} = E_{Fn} - E_{Fp} = E_{Fnp}$[1]. For this stationary case of a fast relaxation of the charge carriers with respect to their recombination lifetime τ, the chemical potential of the electron-hole ensemble equals the chemical potential of the photon field μ_γ [21, 38].

By describing the electron and hole distributions under illuminated conditions with different Fermi levels E_{Fn} and E_{Fp} it is possible to calculate the emitted luminescence of a semiconductor. When considering a semiconductor of thickness d with no photons incident from the outside, the continuity equation for the photon flux $\mathrm{d}j_\gamma$ flowing through the material towards the surface can be written under steady state conditions according to Würfel [13] as

$$\mathrm{div}\ \mathrm{d}j_\gamma = r_{em} - (r_{abs} - r_{st}) = r_{em} - \alpha(\hbar\omega)\mathrm{d}j_\gamma. \tag{3.4}$$

Where r_{em}, r_{abs} and r_{st} are spontaneous emission rate, absorption rate and stimulated emission rate respectively. The net absorption rate $r_{abs} - r_{st}$ is expressed by the absorption coefficient α. The spontaneous emission rate $\mathrm{d}r_{em}$ under illuminated conditions can be derived analogously to Planck's radiation law with a splitting of quasi-Fermi levels $E_{Fnp} = E_{Fn} - E_{Fp}$ and an absorption coefficient $\alpha(\hbar\omega)$ and is given by [38]

$$\mathrm{d}r_{em} = \alpha(\hbar\omega)\frac{cD_\gamma\Omega}{\exp\left(\frac{\hbar\omega - E_{Fnp}}{kT}\right) - 1}\mathrm{d}\hbar\omega, \tag{3.5}$$

with the density of states $D_\gamma = (\hbar\omega)^2/(4\pi^3c^3\hbar^3)$ and the speed of light c. The photon flux $\mathrm{d}j_{\gamma,em}$ emitted through the surface of the sample taking into account multiple reflections is found by integrating eq. (3.4) over the sample thickness d [13, 17]

$$\mathrm{d}j_{\gamma,em} = \alpha(\hbar\omega)\frac{cD_\gamma\left(1 - R_F\right)e^{-\alpha d}}{1 - R_B R_F e^{-2\alpha d}}\Omega\mathrm{d}\hbar\omega\int_0^d \frac{e^{\alpha z} + R_B e^{-\alpha z}}{\exp\left(\frac{\hbar\omega - E_{Fnp}(z)}{kT}\right) - 1}\mathrm{d}z. \tag{3.6}$$

---

[1] For abbreviation E_{Fnp} is used in this work synonymical to the quasi-Fermi level splitting $E_{Fn} - E_{Fp}$.

Under the assumption of a constant quasi-Fermi level splitting over the absorber thickness [13] — which is provided in most solar cells, since diffusion lengths of charge carriers have to be in the range of the cell thickness to guarantee proper carrier collection and a reasonable efficiency — one gets Planck's generalized radiation law which describes the emission of thermal $(E_{Fn} - E_{Fp}) = 0$ and luminescent $(E_{Fn} - E_{Fp}) \neq 0$ radiation [13]

$$\mathrm{d}j_{\gamma,em}(\hbar\omega) = A(\hbar\omega)\frac{\Omega}{4\pi^3\hbar^3c^2}\frac{(\hbar\omega)^2}{\exp\left(\frac{\hbar\omega - E_{Fnp}}{kT}\right) - 1}\mathrm{d}(\hbar\omega) \tag{3.7}$$

with

$$A(\hbar\omega) = (1 - R_F)(1 - \mathrm{e}^{-\alpha d})\frac{(R_B - R_F R_B)(\mathrm{e}^{-\alpha d} - \mathrm{e}^{-2\alpha d})}{1 - R_F R_B \mathrm{e}^{-2\alpha d}} \tag{3.8}$$

or if multiple reflection are negligible $A(\hbar\omega) = (1 - R_F)(1 - \mathrm{e}^{-\alpha d})$. In both cases phase relationships have been neglected, for details see [39].

In the case of a polycrystalline semiconductor consisting of grains with different opto-electronical and structural properties the emitted photon current depends on the lateral position $\mathrm{d}j_{\gamma,em}(x, y, \hbar\omega)$. Under the assumption that the semiconductor properties are constant over the thickness and that the lateral diffusion can be neglected eq. (3.7) becomes

$$\mathrm{d}j_{\gamma,em}(x, y, \hbar\omega) = \frac{\Omega}{4\pi^3\hbar^3c^2}\frac{A(x, y, \hbar\omega)(\hbar\omega)^2}{\exp\left(\frac{\hbar\omega - E_{Fnp}(x,y)}{kT(x,y)}\right) - 1}\mathrm{d}(\hbar\omega)\mathrm{d}A_r, \tag{3.9}$$

with surface element $\mathrm{d}A_r$.

For photon energies $\hbar\omega - E_{Fnp} \gg kT$ the Boltzmann approximation is valid and eq. (3.9) becomes

$$j_{\gamma,det}(x, y, \hbar\omega) = C \cdot \frac{A(\hbar\omega, x, y)(\hbar\omega)^2}{\exp\left(\frac{\hbar\omega - E_{Fnp}(x,y)}{kT}\right)}, \tag{3.10}$$

for the photoluminescence $j_{\gamma,det}(x, y, \hbar\omega)$ measured with a detector[2] and with $C = \frac{\Omega}{4\pi^3\hbar^3c^2}$. Thus the extraction of the quasi-Fermi level splitting $E_{Fnp}(x, y)$ and temperature $T(x, y)$ are possible via

$$\ln\left(\frac{j_{\gamma,det}(x, y, \hbar\omega)}{C(\hbar\omega)^2}\right) = \ln\left(A(x, y, \hbar\omega)\right) - \frac{\hbar\omega - E_{Fnp}(x, y)}{kT}. \tag{3.11}$$

---

[2] In the detected photon flux the spectral sensitivity of detector and optical setup has to be taken into account.

For sufficient high photon energies above the band gap of the semiconductor the absorbance approaches unity[3] $A(\hbar\omega) \approx 1$, making a description of the photoluminescence by only the Bose term $B(\hbar\omega)$ possible [40, 41]

$$\ln\left(\frac{j_{\gamma,det}(x,y,\hbar\omega)}{C(\hbar\omega)^2}\right) = -\frac{\hbar\omega - E_{Fnp}(x,y)}{kT} = B(x,y,\hbar\omega). \tag{3.12}$$

According to Daub and others [21, 42] it is possible to determine the absorbance from the photoluminescence signal

$$A(x,y,\hbar\omega) = \frac{j_{\gamma,det}(x,y,\hbar\omega)}{C(\hbar\omega)^2}\exp\left[-B(x,y,\hbar\omega)\right], \tag{3.13}$$

provided the diffusion lengths of electrons and holes are much larger than the sample thickness. Otherwise an exact knowledge of the spatial distribution of carrier concentrations is necessary.

3.1.1. Superposition of Independent Photoluminescence Centers

If the photoluminescence of a polycrystalline semiconductor is measured without sufficient resolution, the detected signal $\overline{j_{\gamma,det}}(\hbar\omega)$ is a superposition of individual PL centers $j_{\gamma,det}(x,y,\hbar\omega)$. Instead of integrating over the area A_r emitting the luminescence eq. (3.9) or eq. (3.10) is transferred into an integration over an ensemble of quasi-Fermi level splittings $\mathrm{d}P_{E_{Fnp}}$ and absorbances $\mathrm{d}P_A$

$$\overline{j_{\gamma,det}}(\hbar\omega) = C(\hbar\omega)^2\int_0^\infty\int_0^\infty A(x,y,\hbar\omega)\exp\left(-\frac{\hbar\omega - E_{Fnp}(x,y)}{kT}\right)\mathrm{d}P_{E_{Fnp}}\mathrm{d}P_A. \tag{3.14}$$

In the first approach a laterally constant absorbance $A(\hbar\omega) = A(x,y,\hbar\omega)$ is assumed. For the distribution function $\mathrm{d}P_{E_{Fnp}}$ of the quasi-Fermi level splitting a gaussian distribution according to

$$\mathrm{d}P_{E_{Fnp}} = \frac{1}{\sigma_{E_{Fnp}}\sqrt{2\pi}}\exp\left(-\frac{(E_{Fnp} - \overline{E_{Fnp}})^2}{2\sigma^2_{E_{Fnp}}}\right)\mathrm{d}E_{Fnp} \tag{3.15}$$

is used. Thus integrating eq. (3.14) with (3.15) leads to

$$\begin{aligned}\overline{j_{\gamma,det}}(\hbar\omega) &= \frac{C(\hbar\omega)^2A(\hbar\omega)}{\sigma_{E_{Fnp}}\sqrt{2\pi}}\int_0^\infty \exp\left(-\frac{\hbar\omega - E_{Fnp}}{kT}\right)\exp\left(-\frac{(\overline{E_{Fnp}} - E_{Fnp})^2}{2\sigma^2_{E_{Fnp}}}\right)\mathrm{d}E_{Fnp}\\ &= C(\hbar\omega)^2A(\hbar\omega)\frac{\frac{1}{2}\left[\operatorname{erf}\left(\frac{\overline{E_{Fnp}}}{\sqrt{2}\sigma_{E_{Fnp}}} + \frac{\sigma_{E_{Fnp}}}{\sqrt{2}kT}\right) + 1\right]}{\exp\left(\frac{\hbar\omega - \left(\overline{E_{Fnp}} + \sigma^2_{E_{Fnp}}/(2kT)\right)}{kT}\right)}\end{aligned} \tag{3.16}$$

---

[3] If the reflectivity R_F above the band-gap is not negligible, then $A = (1 - R_F)$.

So, in contrast to eq. (3.10) the detected PL signal $\overline{j_{\gamma,det}}(\hbar\omega)$ depends on the variation in quasi-Fermi level splittings via its standard deviation $\sigma_{E_{Fnp}}$. For all average quasi-Fermi level splittings $\overline{E_{Fnp}} \geq 50meV$ the error function term $\triangle_{erf} = \frac{1}{2}\left[\mathrm{erf}\left(\frac{\overline{E_{Fnp}}+\frac{\sigma^2}{kT}}{\sqrt{2}\sigma}\right)+1\right]$ becomes unity (see figure 3.1a), thus eq. (3.16) becomes

$$\overline{j_{\gamma,det}}(\hbar\omega) = C(\hbar\omega)^2 A(\hbar\omega)\exp\left(-\frac{\hbar\omega-\left(\overline{E_{Fnp}}+\sigma^2_{E_{Fnp}}/(2kT)\right)}{kT}\right). \tag{3.17}$$

In the limit of $\sigma_{E_{Fnp}} \to 0$ eq. (3.17) approaches unity and $\overline{j_{\gamma,det}}(\hbar\omega) = j_{\gamma,det}(x,y,\hbar\omega) = j_{\gamma,det}(\hbar\omega)$. Analogously to eq. (3.11) for $A(\hbar\omega) \approx 1$

$$\begin{aligned}\ln\left(\frac{\overline{j_{\gamma,det}}(\hbar\omega)}{C(\hbar\omega)^2}\right) &= -\frac{\hbar\omega-\left(\overline{E_{Fnp}}+\frac{\sigma^2_{E_{Fnp}}}{2kT}\right)}{kT} \\ &= -\frac{\hbar\omega-E_{Fnp,macro}}{kT}. \end{aligned} \tag{3.18}$$

Figure 3.1c shows the superimposed PL signal $\overline{j_{\gamma,det}}(\hbar\omega)$ for varying standard deviations $\sigma_{E_{Fnp}}$ and an average quasi-Fermi level splitting of $\overline{E_{Fnp}} = 700$ meV. It is clearly seen that a larger variation (larger $\sigma_{E_{Fnp}}$) results in a higher PL signal. Thus extracting the quasi-Fermi level splitting $E_{Fnp,macro}$ of the superposition of different PL centers with a gaussian shaped distribution of E_{Fnp} leads to an overestimation by the factor $\frac{\sigma^2_{E_{Fnp}}}{2kT}$. Figure 3.1b shows the deviation $\triangle_{av} = \frac{\sigma^2_{E_{Fnp}}}{2kT}$ between extracted and correct quasi-Fermi level splitting for the range of standard deviations expected in chalcopyrite absorber layers.

To study the influence of a laterally varying absorption coefficient $\alpha(x,y,\hbar\omega)$ the transmission $T(x,y,\hbar\omega,E_g)$ through a polycrystalline ideal direct semiconductor is calculated by

$$T(x,y,\hbar\omega,E_g) = e^{-\frac{a}{\hbar\omega}\sqrt{\hbar\omega-E_g(x,y)}d} \qquad \hbar\omega > E_g(x,y) \tag{3.19}$$

with varying band-gap $E_g(x,y)$[4]. In CuInS$_2$ the constant $a \approx 1\times 10^5\,\mathrm{eV}^{1/2}\mathrm{cm}^{-1}$ [29]. Thus analogously to eq. (3.14) the averaged transmission $\overline{T}(\hbar\omega,E_g)$ is given by

$$\begin{aligned}\overline{T}(\hbar\omega,E_g) &= \int_0^\infty e^{-\frac{a}{\hbar\omega}\sqrt{\hbar\omega-E_g(x,y)}d}\,\mathrm{d}P_{E_g} \\ &= \int_0^\infty \exp\left(-\frac{ad}{\hbar\omega}\sqrt{\hbar\omega-E_g}\right)\exp\left(-\frac{(E_g-\overline{E_g})^2}{2\sigma^2_{E_g}}\right)\mathrm{d}E_g \end{aligned} \tag{3.20}$$

---

[4] Because fluctuations in A and T should be studied the reflection R has been set to zero for simplicity. Multiple reflections are neglected because A_{id} has a steep absorption edge.

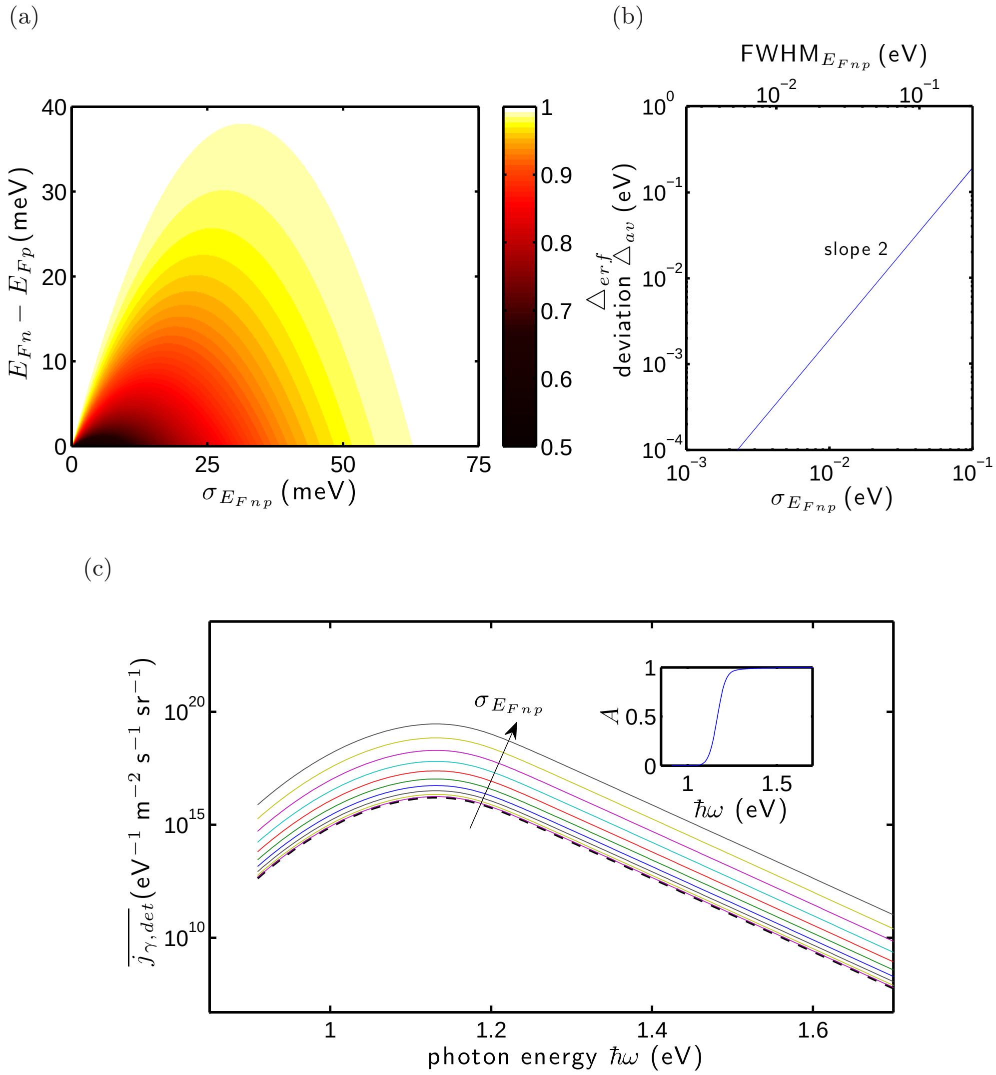

Figure 3.1.: Superposition of individual PL centers, a) shows the error function term $\triangle_{erf} = \frac{1}{2}\left[\mathrm{erf}\left(\frac{\overline{E_{Fnp}}}{\sqrt{2}\sigma_{E_{Fnp}}} + \frac{\sigma_{E_{Fnp}}}{\sqrt{2kT}}\right) + 1\right]$ of eq. 3.17 depending on average quasi-Fermi level splitting $\overline{E_{Fnp}}$ and standard deviation $\sigma_{E_{Fnp}}$, b) shows the deviation $\triangle_{av} = E_{Fnp,macro} - \overline{E_{Fnp}}$ between extracted quasi-Fermi level splitting $E_{Fnp,macro}$ of a superposition of PL signals and the correct averaged quasi-Fermi level splitting $\overline{E_{Fnp}}$ versus the standard deviation $\sigma_{E_{Fnp}}$. c) shows PL spectra calculated with a quasi-Fermi level splitting of $\overline{E_{Fnp}} = \overline{E_{Fn} - E_{Fp}} = 700$ meV, a temperature of $T = 300$ K and an hypothetical absorbance A shown in the inset.

for e.g. a gaussian shaped distribution of band-gap energies E_g with standard deviation σ_{E_g}

$$\mathrm{d}P_{E_g} = \frac{1}{\sigma_{E_g}\sqrt{2\pi}} \exp\left(-\frac{(E_g - \overline{E_g})^2}{2\sigma_{E_g}^2}\right) \mathrm{d}E_g.$$

Since this integral can't be solved analytically eq. (3.20) is numerically integrated with an absorber thickness of $d = 2.5\,\mu\mathrm{m}$ for different standard deviations σ_{E_g}.

The result (shown in fig. 3.2a) is a broadening of the absorption edge. Figure 3.2b shows the photoluminescence according to

$$\begin{aligned}\overline{j_{\gamma,det}}(\hbar\omega) &= C(\hbar\omega)^2 \overline{A}(\hbar\omega, E_g, \sigma_{E_g}) \exp\left(-\frac{\hbar\omega - E_{Fnp}}{kT}\right) \\ &= C(\hbar\omega)^2 \left(1 - \overline{T}(\hbar\omega, E_g, \sigma_{E_g})\right) \exp\left(-\frac{\hbar\omega - E_{Fnp}}{kT}\right)\end{aligned}$$

for $T = 300$ K and $E_{Fnp} = 700$ meV. A larger σ_{E_g} leads to a higher PL yield in the lower energy range, furthermore the maximum shifts to lower energies. Because of the broadened absorption edge the value where the condition $\overline{A}(\hbar\omega) \approx 1$ is met shifts to higher energies. Figure 3.2c shows the photon energy $\hbar\omega(A = 0.97)$ depending on band-gap fluctuations σ_{E_g}, this value can shift by more than 100 meV. Since chapter 2.2 has shown that the samples have a high surface roughness the impact of a varied absorption due to thickness variations can be studied analogously to eq. (3.20) which contains the term $\exp(-\alpha d)$. For a symmetric distribution of absorber thickness variations the contributions of locations with different thicknesses cancel out, thus

$$\begin{aligned}\overline{T}(\hbar\omega, d) &= \int_0^\infty (1 - A(\hbar\omega, d))\mathrm{d}P_d \\ &= \int_0^\infty e^{-\alpha d} \exp\left(-\frac{(d - \overline{d})^2}{2\sigma_d^2}\right) \mathrm{d}d \\ &= e^{-\alpha\overline{d}}\left[-\frac{1}{2}e^{\frac{1}{2}\sigma_d^2\alpha^2}\left(\mathrm{erf}\left(\frac{\alpha\sigma_d - D}{\sqrt{2}\sigma_d}\right) - 1\right)\right] \\ &\approx e^{-\alpha\overline{d}} = T(\hbar\omega, \overline{d}).\end{aligned} \tag{3.21}$$

With

$$\mathrm{d}P_d = \frac{1}{\sigma_d\sqrt{2\pi}} \exp\left(-\frac{(d - \overline{d})^2}{2\sigma_d^2}\right) \mathrm{d}d.$$

It has to be noted that only the consequences due to a variation in the absorbance has been studied. If actually measuring the transmission of light through a sample reflection and dispersion have to be taken into account as well.

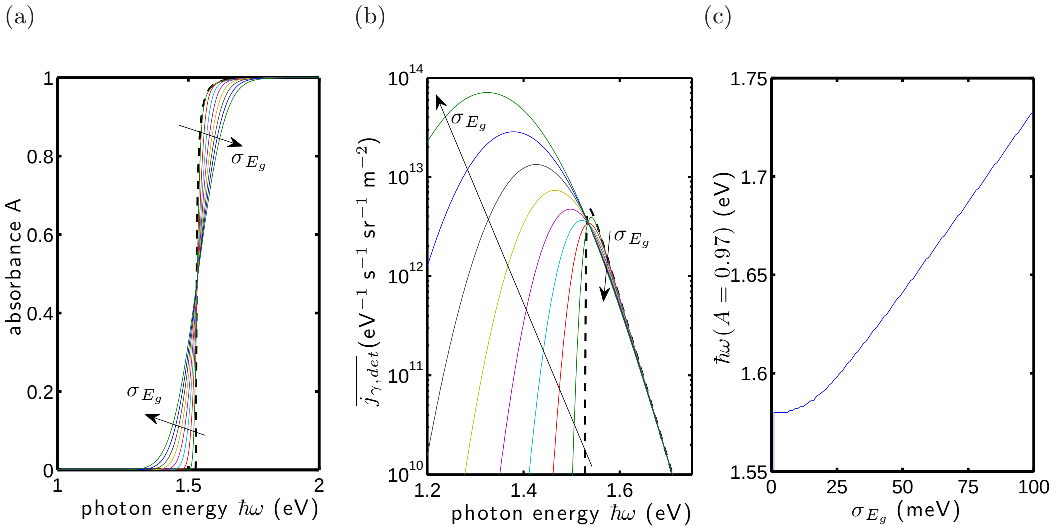

Figure 3.2.: a) superposition of the absorbance through an absorber with laterally varying absorption coefficient $\alpha_{id}(x, y)$ according to eq. 3.20 with $\overline{A} = 1 - \overline{T}$. b) superposition of individual PL centers with constant quasi-Fermi level splitting and varying absorbance $A(x, y, \hbar\omega)$. c) $\hbar\omega(A = 0.97)$ depending on band-gap fluctuations σ_{E_g}.

3.1.2. Band-Gap Grading

Besides the lateral fluctuations of opto-electronic absorber properties the Cu(In,Ga)S_2 samples show a band-gap gradient over the absorber thickness d caused by a depth dependent Ga concentration. Energy dispersive X-ray (EDX) measurements on Cu(In,Ga)S_2 samples have shown a nearly pure $CuGaS_2$ layer at the back and a Cu($In_{1-\xi}Ga_\xi$)S_2 layer with small ξ at the top with a steep transition or say small intermixture of both layers [6]. Although this measurement might not be representative a similar grading will occur in the Cu(In,Ga)S_2 samples analyzed in this work. Figure 3.3 shows a band-gap profile $E_g(z)$ according to eq. (2.2) with an In to Ga ratio extracted from the data in [6]. A realistic band-gap model, which reproduces the actual grading with a transition from a $CuInS_2$ or Cu($In_{1-\xi}Ga_\xi$)S_2 layer with low Ga content to a nearly pure $CuGaS_2$ layer, is a step-like function according to

$$E_g(z) = \frac{E_{g,0} - E_{g,d}}{\exp\left(\frac{z - z_t}{z_w}\right) + 1} + E_{g,d}, \tag{3.22}$$

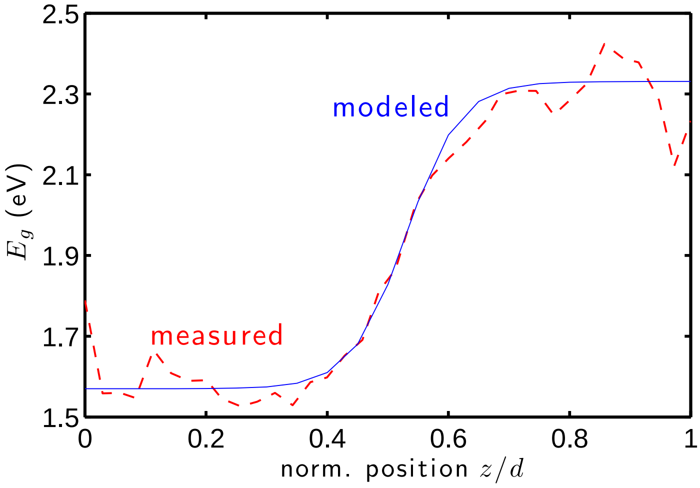

Figure 3.3.: Band-gap profile of Cu(In,Ga)S$_2$ according to eq. (2.2) with the In to Ga ratio from [6] (dashed red line) and modeled band-gap profile (blue) according to eq. (3.22) with $z_t = 0.53d$, $E_{g,0} = 1.57\,\text{eV}$, $E_{g,d} = 2.33\,\text{eV}$ and $z_w = 0.045d$.

with parameters $z_t = 0.53d$ as the transition point from one band-gap $E_{g,0} = 1.57\,\text{eV}$ to another $E_{g,d} = 2.33\,\text{eV}$ and $z_w = 0.045d$ as transition width. The large band-gap regime in figure 3.3 covers nearly half of the absorber. Depending on the preparation process this regime and the intermixture may vary due to inhomogeneities between different sample positions.

As a result of the band-gap grading the absorption coefficient, which depends on the band-gap $E_g(x, y, z)$, varies laterally and over the absorber thickness $\alpha(x, y, z, \hbar\omega)$. According to the Kramers-Kronig relation a variation in α goes along with a variation in the refractive index n_r. But since measurements on Cu(In,Ga)Se$_2$ have shown only a small dependence of n_r on the Ga content [43], which can also be expected for Cu(In,Ga)S$_2$, the depth dependence of the refractive index shall be neglected here.

Because lateral variations in α have been studied in the previous section, this section focusses on the variation of α over the absorber thickness. Thus $\alpha(x, y, z, \hbar\omega) = \alpha(z, \hbar\omega)$ and Lambert-Beers law becomes

$$\frac{\mathrm{d}\Phi}{\mathrm{d}z} = -\alpha(z)\Phi \tag{3.23}$$

for the photon flux Φ. The transmission through a sample is given by solving eq.

(3.23)

$$T = \frac{\Phi(d)}{\Phi_0} = e^{-\int_0^d \alpha(z)\mathrm{d}z}, \tag{3.24}$$

so α has to be integrated over the absorber thickness[5]. Using the absorption coefficient $\alpha_{id}(z, \hbar\omega) = \frac{a}{\hbar\omega}\sqrt{\hbar\omega - E_g(z)}$ of an ideal direct semiconductor, the transmission through a sample with a band-gap grading according to eq. (3.22) can be calculated. Since the analytical solution of the integral $\int \alpha(z)\mathrm{d}z$ is lengthy it can be found in appendix A.

Figure 3.4 shows modeled absorbance spectra $A = 1 - T$ for a variation of one of the parameters z_t, z_w and $E_{g,d}$[6]. A change of the transition point z_t in a two layer system of $\mathrm{CuInS_2}$ with $E_g = 1.53\,\mathrm{eV}$ and $\mathrm{Cu(In,Ga)S_2}$ with $E_g = 2.5\,\mathrm{eV}$ (fig. 3.4a) leads to the absorbances shown in figure 3.4d. For a thinner high band-gap $\mathrm{CuGaS_2}$ layer the absorbance near the $\mathrm{CuInS_2}$ band-edge increases (indicated by arrows). A higher transition width z_w or a smoother transition between $\mathrm{CuInS_2}$ and $\mathrm{CuGaS_2}$ layer (fig. 3.4b) effectively decreases the absorption of photons close to the $\mathrm{CuInS_2}$ band-edge (figure 3.4e). If the second layer provides a lower band-gap than the first (dashed lines in fig. 3.4f) the absorbance in the low energy range increases significantly. A higher band-gap in the second layer on the other hand has only a non-negligible effect if the first layer is comparably thin (figure 3.4d and 3.4f), if not, all photons between $E_{g,0}$ and $E_{g,d}$ are absorbed anyway due to the high absorption coefficient and the steep absorption edge of the ideal direct semiconductor.

Since a depth-dependent absorption coefficient $\alpha(z, \hbar\omega)$ leads to depth-dependent excess carrier densities $\Delta n_{e,h}(z)$ and a depth-dependent quasi-Fermi level splitting $E_{Fnp}(z) = E_{Fn}(z) - E_{Fp}(z)$ Planck's generalized (eq. (3.7)) has to be modified for calculating the photon flux emitted by an absorber with graded band-gap. Instead of eq. (3.6) we get

$$\begin{aligned} dj_{\gamma,em,z}(\hbar\omega) &= C(\hbar\omega)^2 \frac{(1 - R_F)\, e^{-\int_0^d \alpha(z)\mathrm{d}z}}{1 - R_B R_F e^{-2\int_0^d \alpha(z)\mathrm{d}z}} \Omega \mathrm{d}\hbar\omega \\ &\quad \times \int_0^d \alpha(z_i, \hbar\omega) \frac{e^{\int_{z_i}^d \alpha(z)\mathrm{d}z} + R_B e^{-\int_{z_i}^d \alpha(z)\mathrm{d}z}}{\exp\left(\frac{\hbar\omega - E_{Fnp}(z_i)}{kT}\right) - 1} \mathrm{d}z_i \end{aligned} \tag{3.25}$$

---

[5] In this case the reflection of the sample has been neglected for simplicity.

[6] Since $\alpha_{id}(\hbar\omega) \in \mathbb{C}$ and $\Re(\alpha_{id}(\hbar\omega)) = 0$ for $\hbar\omega < E_g$, the real part $\Re(-\int \alpha(z, \hbar\omega)\mathrm{d}z)$ is plotted in each of the figures.

(a) Band-gap profile (b) Band-gap profile (c) Band-gap profile

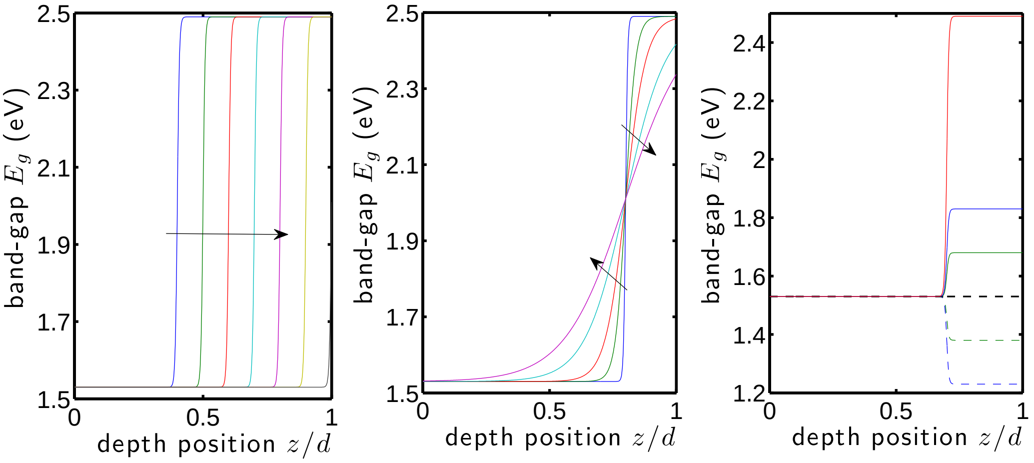

(d) Absorbance for case 3.4a (e) Absorbance for case 3.4b (f) Absorbance for case 3.4c

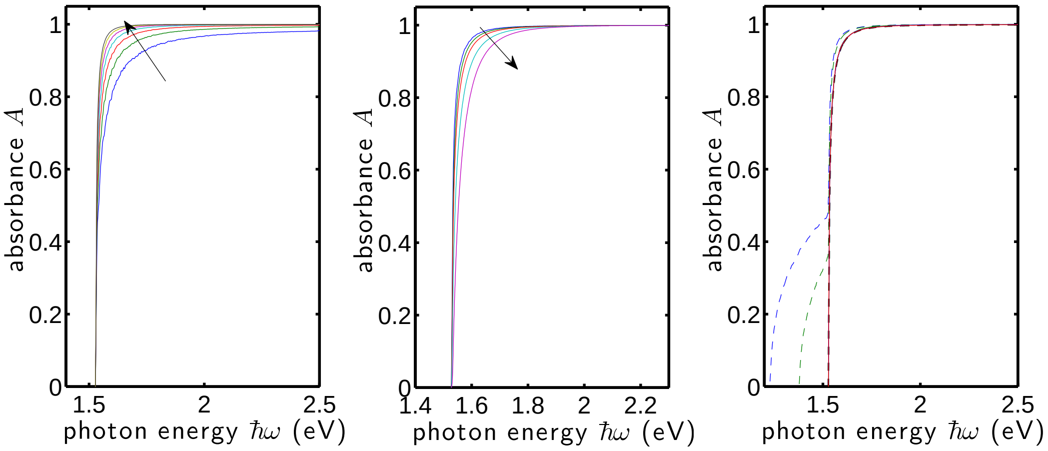

Figure 3.4.: Absorbance of an ideal direct semiconductor with depth-dependent band-gap $E_g(z)$. To describe the band-gap profile a step-like distribution (3.22) is used. The band-gap profiles according to 3.4a, 3.4b and 3.4c lead according to eq. (3.24) with $A = 1 - T$ to the absorbances 3.4d, 3.4e and 3.4e located in the graphs shown below.

where a high thermal conductivity compared to the thickness of the absorber layer has been assumed, thus $T(z) \approx T = const.$. If multiple reflections can be neglected eq. (3.25) becomes

$$dj_{\gamma,em,z}(\hbar\omega) \quad = \quad C(\hbar\omega)^2\,(1-R_F)\,\Omega\mathrm{d}\hbar\omega \int\limits_0^d \frac{\alpha(z_i,\hbar\omega)e^{-\int\limits_{z_i}^{0}\alpha(z)\mathrm{d}z}}{\exp\left(\frac{\hbar\omega-E_{Fnp}(z_i)}{kT}\right)-1}\mathrm{d}z_i. \quad (3.26)$$

This is a non-trivial problem, since the system of semiconductor equations has to be solved in order to calculate $E_{Fn}(z) - E_{Fp}(z)$ [38]. Rather than solving these equations, which is beyond the scope of this work, a rough estimate of $E_{Fn}(z) - E_{Fp}(z)$ shall be made to calculate the emitted PL according to eq. (3.26). According to eq. (3.1) and (3.3) the depth dependent quasi-Fermi level splitting $E_{Fn}(z) - E_{Fp}(z)$ is determined by the local band-gap $E_g(z)$ and the local distribution of electrons $n(z)$ and holes $p(z)$. For illumination with monochromatic light of energy $\hbar\omega > E_{g,0}$ the huge part of photons is absorbed close to the surface and the steady state carrier depth profile $n(z)$, $p(z)$ is determined by the absorption coefficient $\alpha(z)$ and the diffusion length L_D of excited carriers which is in the order of the absorber thickness d. In a rough approximation a blurred form of the band-gap profile $E_g(z)$ according to eq. (3.22) is used to describe the depth dependent quasi-Fermi level

$$E_{Fn}(z) - E_{Fp}(z) = \frac{E_{Fnp}(0) - E_{Fnp}(d)}{\exp\left(\frac{z-z_t}{z_{w,f}}\right)+1} + E_{Fnp}(d)$$

and estimate the effect of a graded band-gap on the emitted PL yield. Figure 3.5b shows the depth profile of $E_{Fn}(z) - E_{Fp}(z)$ for the band-gap grading in figure 3.5a, the transition width of the quasi-Fermi level profile has been varied in the range $z_{w,f} = z_w$ to $z_{w,f} = 10 \times z_w$, with $E_{Fnp}(0) = E_{g,0}/2$ and $E_{Fnp}(d) = E_{g,d}/2$. Figure 3.5c shows the photoluminescence emitted through the front surface ($z = 0$) of the absorber layer according to eq. (3.26). Since $R_F \approx const.$ in this photon energy range it has been neglected for simplicity.

In all cases the PL emitted in the high band-gap region of the absorber layer is — due to reabsorption — several orders of magnitude smaller than the PL emitted from the low band-gap region close to the absorber surface. For an equal transition width in $E_{Fn}(z) - E_{Fp}(z)$ and $E_g(z)$, ($z_{w,f} = z_w$ blue in figs 3.5b and 3.5c) the quasi-Fermi level splitting in the low band-gap region ($z < z_t$) is constant and the high-energy wing of the PL emitted in this region can be described by a linear approximation according to eq. (3.12) with $E_{Fn}(0) - E_{Fp}(0)$. With increasing $z_{w,f}$ the profile $E_{Fn}(z) - E_{Fp}(z)$ for $z < z_t$ becomes more and more inhomogeneous and thus the PL

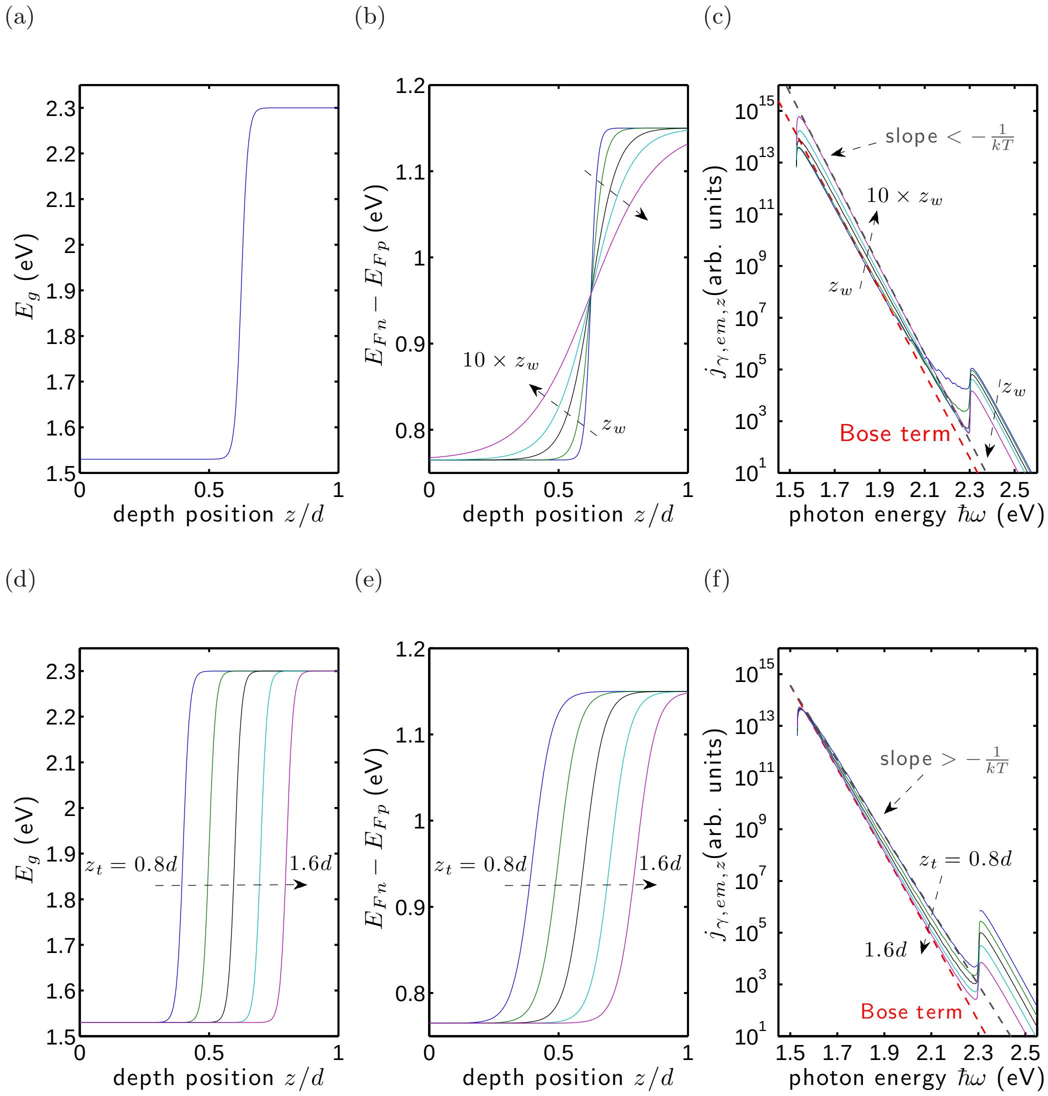

Figure 3.5.: PL of an ideal direct semiconductor with depth-dependent band-gap $E_g(z)$. To describe the band-gap as well as quasi-Fermi level splitting profile a step-like function according to (3.22) is used. The profiles for $E_{Fnp}(z)$ of 3.5b and 3.5e lead according to eq. (3.26) to the PL 3.5c and 3.5f.

emitted from deeper low band-gap regions ($z < z_t$) has a higher local quasi-Fermi level splitting. Since the absorption coefficient α increases with photon energy, the high energetic luminescence from these deeper regions with $z < z_t$ is subjected more to reabsorption (see figure 3.5c). In this case a linear approximation of the high energy wing of the PL ($j_{\gamma,em,z}(\hbar\omega < 2.1\,\mathrm{eV})$ in fig. 3.5c) leads to a slope $< -1/kT$ and an average quasi-Fermi level splitting $\overline{(E_{Fn} - E_{Fp})}_{lowE_g}$ of the low band-gap region higher than $E_{Fn}(0) - E_{Fp}(0)$.

The next three figures (3.5d-3.5f) illustrate a variation in the thickness of high and low band-gap region. For all cases the quasi-Fermi level splitting has been calculated according to eq. (3.27) with $z_{wf} = 3z_w$, $E_{Fnp}(0) = E_{g,0}/2$ and $E_{Fnp}(d) = E_{g,d}/2$, so the regime of high $E_{Fn} - E_{Fp}$ extends into the low band-gap region (see figure 3.5d and 3.5e). For a thin high band-gap region at the rear of the absorber layer (purple in figure 3.5d to 3.5e) nearly all of the PL with $E_{Fnp}(z) > E_{Fnp}(0)$ is reabsorbed and the quasi-Fermi level splitting of the low band-gap region can be described by eq. (3.12) with $E_{Fn}(0) - E_{Fp}(0)$ in good approximation (see dashed line in figure 3.5e). For thinner low E_g regions the PL emitted in the transition region (around z_t) and in the high E_g region ($z \gtrsim z_t - 2z_{wf}$) is subjected to less reabsorption and thus the high energetic PL increases. A linear approximation of $j_{\gamma,em}(\hbar\omega < 2.1\,\mathrm{eV})$ leads to a slope $> -1/kT$ and an average quasi-Fermi level splitting $\overline{(E_{Fn} - E_{Fp})}_{lowEg} < E_{Fn}(0) - E_{Fp}(0)$.

The illustrated examples visualize the possible influence of a band-gap grading on the emitted PL. In all cases with a thin high band-gap region and a quasi-Fermi level splitting following the grading of the band-gap or a very small gradient an extraction of the quasi-Fermi level splitting $E_{Fn}(z < z_t) - E_{Fp}(z < z_t) \approx const.$ can be made by an approximation of the high energy wing (eq. (3.12)) with $E_{Fn}(0) - E_{Fp}(0)$. If the low E_g region close to the surface of the absorber layer is comparably thin or if the grading of $E_{Fnp}(z)$ extends far into the low E_g region, a linear approximation according to eq. (3.12) becomes incorrect. An indicator are slopes $\neq -1/kT$. For the actual profile of $E_{Fnp}(z)$ the local band-gap profile $E_g(x, y, z)$, diffusion length $L_D(x, y, z)$ etc. would have to be known in order to be able to solve the semiconductor equations. The impact of graded band-gaps in Cu(In,Ga)Se$_2$ thin films on the solar cell performance has been studied in various publications and shows an increase in efficiency η for a high band-gap region at the back of the absorber layer [44–46]. The authors attributed this increase to the effect, that the high band-gap region and the resulting high quasi-Fermi level splitting region acts as a diffusion barrier for minority carriers and therefore reduces the recombination at the back contact.

In a last example the photoluminescence emitted through the front and back surface of an absorber layer with graded band-gap will be studied. For identical absorber

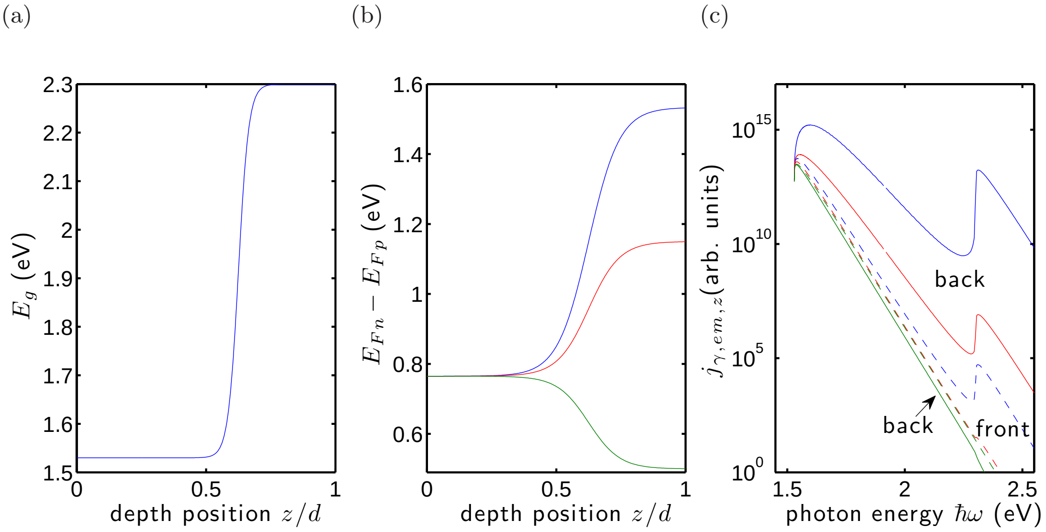

Figure 3.6.: PL emitted through the front ($z = 0$) and back surface ($z = d$) of an ideal direct semiconductor with depth-dependent band-gap $E_g(z)$ according to figure 3.6a. To describe the band-gap, as well as quasi-Fermi level splitting profile analytically representable step functions according to (3.22) are used. The profiles for $E_{Fnp}(z)$ of 3.6b lead according to eq. (3.26) to the PL 3.6c. Solid lines represent the PL emitted through the back and dashed lines emitted through the front surface.

parameters of $E_g(z)$ and $E_{Fnp}(z)$ the PL emitted through front and back surface of the absorber layer differs due to a different reabsorption (figures 3.6). The PL originated in the high E_g region at the back surface of the absorber layer and emitted through the front surface is subjected to high reabsorption, whereas when emitted through the back surface reabsorption is considerable lower (figure 3.6c). The PL originated in the low E_g regime is transmitted nearly without reabsorption through the high E_g region. Nevertheless, due to the higher band-gap at the back of the absorber, a much higher quasi-Fermi level splitting in this region is needed to get detectable PL yields from this regime. If the quasi-Fermi level splitting decreases towards $z = d$ (green in figure 3.6) — e.g. due to a high back surface recombination velocity — the PL originated in the low E_g regime close to the surface is subjected to reabsorption in the transition region ($z \pm 2z_w$) from low to high E_g. Whereas due to smaller $E_{Fnp}(z)$ and higher $E_g(z)$ the PL originated in the region $z > z_t$ is several magnitudes smaller, thus the high energy wing of the resulting PL emitted through the back surface has a slope $< -1/kT$ (green in figure 3.6c).

4. Experimental Setup

4.1. Laterally Resolved Microscopic Measurements

The setup used for measuring laterally and spectrally resolved photoluminescence and white-light transmission consists of a commercial system, a *WiTec* α-SNOM, which has been expanded by a spectrograph and an optical multichannel analyzer (OMA) with a liquid nitrogen cooled 512 pixel InGaAs array. Alternatively the use of a Peltier cooled Silicon OMA (100pixel × 1024 pixel) is available. Since the short wavelength part of the spectrum is better detected by the silicon detector, whereas the InGaAs detector is more suited for longer wavelengths, depending on the purpose of the measurement both spectrally calibrated detectors have been used. A sketch of the setup is shown in figure 4.1. The excitation laser (Nd:YAG) at a wavelength of λ = 532 nm is coupled into the confocal microscope system by a beam splitter and focussed onto the sample by a microscope objective with a numerical aperture of 0.8 and a 60× magnification. Alternatively the excitation laser can be replaced by a halogen lamp.

The luminescence collected from the sample is focussed onto a multi-mode fiber with a nominal diameter of 200 μm that leads to the spectrograph. By the combined use of the OMA and a piezo stage, area scans with a full spectrum for each pixel can be recorded. This setup has a spatial resolution of less than 1 μm [21].

To collect radiation in direction of transmission a second objective beneath the piezo stage can be connected via a fiber to the spectrograph, depending on the substrate thickness an objective with higher working distance and less resolution has to be used. In the same setup atomic force microscopy (AFM) measurements can be carried out by replacing the objective with a cantilever mount and introducing a deflection beam into the beam path.

A similar second setup with a liquid nitrogen cryostat on top of the piezo table offers the possibility to carry out measurements at low temperature ($\geq$ 80 K). The sample is excited with a Helium Neon Laser (λ = 632.8 nm). Due to the cryostat an objective with a larger working distance is necessary, the mirror objective used has a magnification of 36× and an numerical aperture of NA = 0.5.

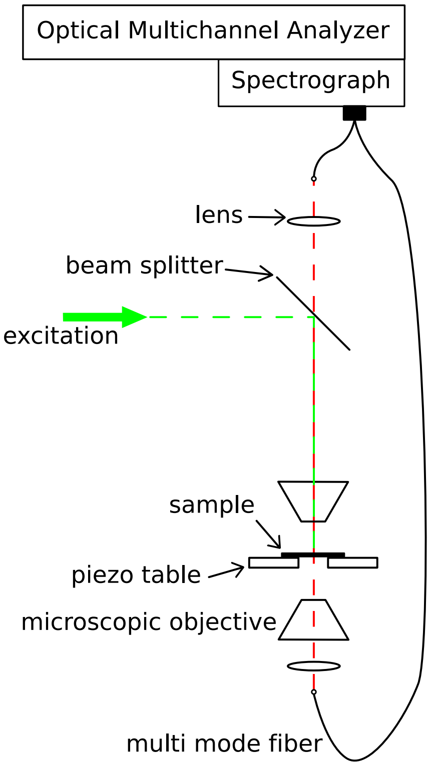

Figure 4.1: Sketch of the experimental setup for measuring laterally and spectrally resolved photoluminescence and white light transmission. The sample is mounted on a piezo table and excited with a 532 nm Nd:YAG laser. The PL can be detected from front (excitation entrance) or from the rear side of the sample by the use of an optical multichannel analyzer (InGaAs or Silicon detector array). Atomic force microscopy measurements can be carried out by mounting a cantilever instead of a microscope objective.

4.2. Macroscopic Calibrated Photoluminescence

A sketch of the setup to record photon fluxes with absolute calibration is outlined in figure 4.2. The sample is excited e.g. by a Nd:YAG laser at 532 nm where a filter wheel is used to adjust laser power. To carry out photoluminescence measurements at low temperature the sample can be mounted in a closed cycle helium cryostat (20 K to 300 K). The generated luminescence is focussed by a lens system through an longpass filter onto the entrance slit of a monochromator. To provide a maximum of sensitivity over a large spectral range three types of detectors are used: a peltier cooled photomultiplier tube (for $\hbar\omega \geq 1.6\,\mathrm{eV}$), a silicon photodiode (1.2 eV to 1.6 eV) and a liquid nitrogen cooled InGaAs detector ($\leq 1.2\,\mathrm{eV}$). By the use of flip mirrors the beam can be guided to the appropriate detector. The photoluminescence signal is recorded with a lock-in amplifier which gets the trigger signal from a chopper in front of the entrance slit of the monochromator.

To calibrate the setup for absolute photon fluxes the spectrum of a tungsten lamp operated at known temperature is recorded. A comparison to a gray body spectrum with the emissivity of tungsten [47] yields the transfer function, a more detailed

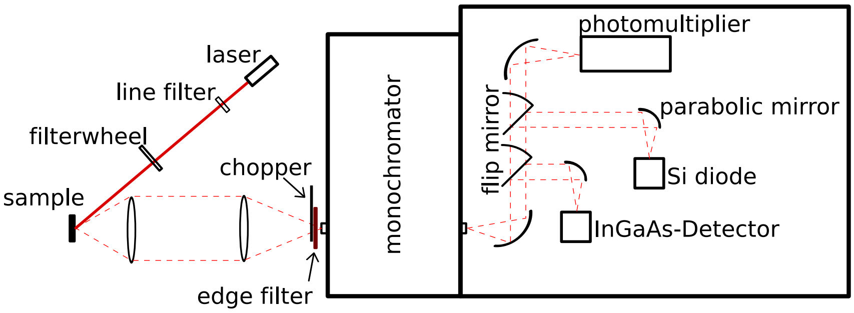

Figure 4.2.: Sketch of the experimental setup for measuring absolute photon fluxes. The photoluminescence of the excited sample is focussed by a lens system onto the entrance slit of a monochromator. Depending on the spectral range one of the three detectors (a peltier cooled photomultiplier tube, a silicon photodiode or a liqiud nitrogen cooled InGaAs detector) can be selected by flip mirrors. An edge filter blocks the laser line from entering the monochromator. The photoluminescence signal is recorded with a lock in amplifier. To minimize noisy photons the detectors are kept in a metal box.

description of the calibration procedure can be found in [17].

4.3. Macroscopic Laterally Resolved Photoluminescence

To carry out laterally resolved photoluminescence measurements a setup according to figure 4.3 with a lateral resolution of approximately 1 mm^2 is used. With this setup areas of several mm^2 can be scanned. Excitation (at e.g. 532 nm) and PL collection is realized by a fiber optic connected to a spectrograph and a liquid nitrogen cooled InGaAs OMA (array with 512 pixel). The sample is placed on a holder with stepper motors in order to to carry out lateral scans. Alternatively the stepper motor can be replaced by a rotation axes to measure the angular dependence of the emitted PL.

Figure 4.3: Sketch of the experimental setup for measuring macroscopic laterally (or angularly) and spectrally resolved photoluminescence. The sample holder is equipped with stepper motors (alternatively the use of a rotation stage is possible). The PL is collected with a collimator and guided to a spectrograph that is connected to an optical multichannel analyzer (InGaAs detector array).

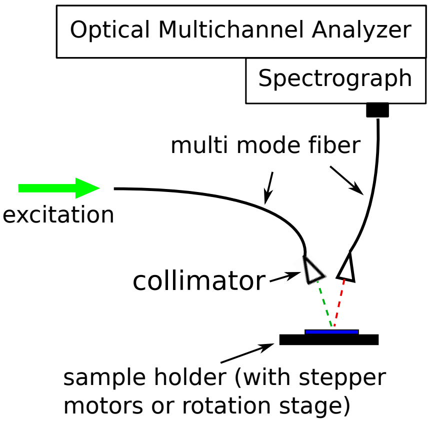

5. Extraction of Opto-Electronic Absorber Properties

In the following chapter the microscopic and laterally resolved as well as macroscopic PL methods for the analyses of polycrystalline chalcopyrite absorbers will be displayed exemplarily on $\mathrm{CuInS_2}$ and $\mathrm{Cu(In,Ga)S_2}$ samples (samples as described in chapter 2).

Since the main topic of the whole chapter is photoluminescence, PL spectra of $\mathrm{CuInS_2}$ and $\mathrm{Cu(In,Ga)S_2}$ provide the best overview and introduction. Figure 5.1a shows spectra of a $\mathrm{CuInS_2}$ (black) and a $\mathrm{Cu(In,Ga)S_2}$ (blue) sample from different positions of a laterally resolved scan in the confocal microscope setup. In order to get detectable PL yields the excitation flux amounts to $\phi = 2.5 \times 10^4$ AM1.5 equivalent photon fluxes ($6.7 \times 10^{21}\,\mathrm{s^{-1}cm^{-2}}$) on $1\,\mathrm{\mu m^2}$. Figure 5.1b shows spectra of the same samples measured in the setup calibrated for absolute photon fluxes with 10 AM1.5 equivalent photon fluxes ($2.7 \times 10^{18}\,\mathrm{s^{-1}cm^{-2}}$) on $1\,\mathrm{mm^2}$. In both cases a 532 nm Nd:YAG laser has been used for excitation.

All spectra show two maxima varying in intensity and energetic position. The peaks can be assigned to "band-to-band" recombination (peak 1) and defect-band (band-defect) recombination (peak 2) [48]. With identical excitation the PL yield of the $\mathrm{Cu(In,Ga)S_2}$ sample is higher, which is also reflected in the high energy wings and thus points towards a higher quasi-Fermi level splitting in $\mathrm{Cu(In,Ga)S_2}$. The substantially varying ratio of peak 1 and peak 2 between microscopic and macroscopic measurements will be adressed in section 5.3. Analyses of both sample types and the transition from microscopic to macroscopic measurements will be discussed below in detail.

5.1. Microscopic Analyses

Figure 5.2a and 5.2c display the integral PL yield $J_\gamma(x,y) = \int j_{\gamma,det}(x,y,\hbar\omega)\mathrm{d}\hbar\omega$ of scans over 60 µm×60 µm ((300×300) spectra) of high quality $\mathrm{CuInS_2}$ and $\mathrm{Cu(In,Ga)S_2}$

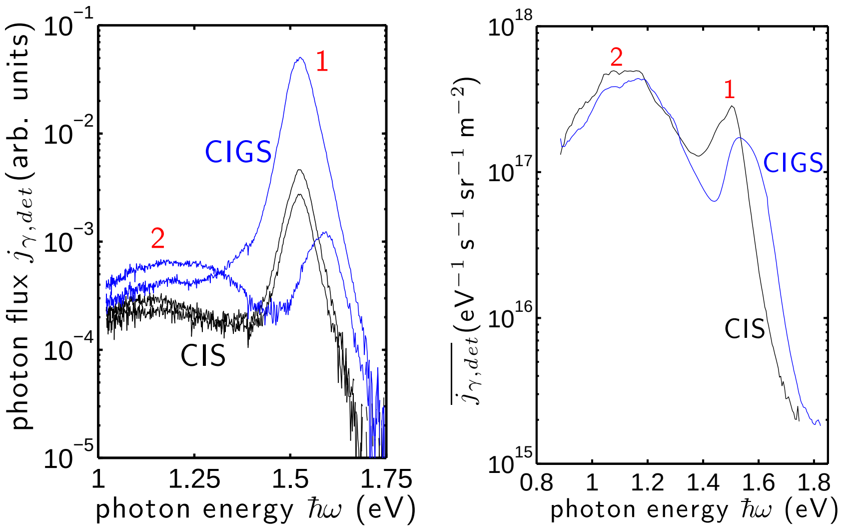
(a) Microscopic (b) Macroscopic

Figure 5.1.: Photoluminescence spectra of $CuInS_2$ and $Cu(In,Ga)S_2$ at different sample positions measured in the confocal microscope setup (5.1a) and in the setup calibrated for absolute photon fluxes (5.1b). Excitation amounts to $\phi = 2.5 \times 10^4$ AM1.5 equivalent photon fluxes ($6.7 \times 10^{21}\,s^{-1}cm^{-2}$) on $1\,\mu m^2$ (confocal setup) and 10 AM1.5 equivalent photon fluxes ($2.7 \times 10^{18}\,s^{-1}cm^{-2}$) on $1\,mm^2$ (setup calibrated for absolute photon fluxes), in both cases with $\lambda_{exc} = 532\,nm$.

samples. In both mappings strong lateral fluctuations on the micron scale can be identified. The histograms of the mappings of the PL-yields show an inhomogeneous distribution with lower intensities occurring more frequently (notice the logarithmic abscissa). With up to a factor of 19 the $Cu(In,Ga)S_2$ sample shows stronger variations. In both cases these fluctuations in the PL yield can be described by a log-normal distribution, in other words the logarithm of the PL yield is normally distributed according to [49]

$$f_{J_\gamma \log}(x) = \frac{a_1}{x} \exp\left(-\frac{(\ln x - M_L)^2}{2\sigma_{M_L}^2}\right), \tag{5.1}$$

with parameters a_1, M_L and σ_L. The log-normal distribution was found to describe distributions resulting from growth processes, e.g. the distribution of grain sizes [35,

(a) J_γ of $CuInS_2$

(b) Histogram of J_γ and Spectra

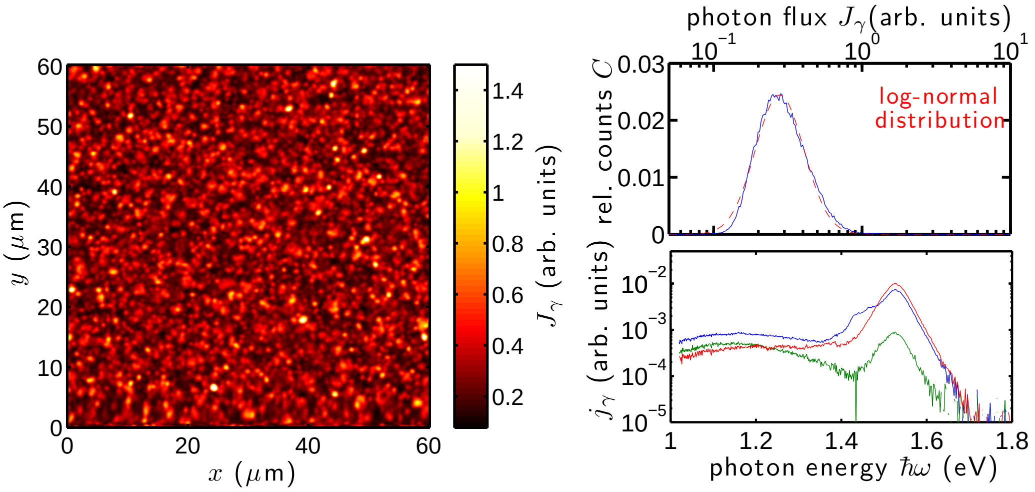

(c) J_γ of Cu(In,Ga)S_2

(d) Histogram of J_γ and Spectra

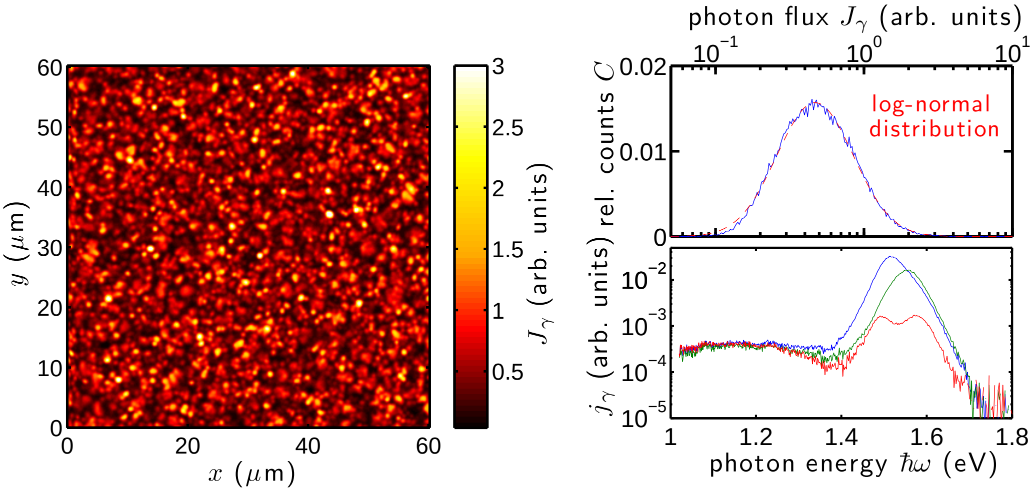

Figure 5.2.: PL yields of a $CuInS_2$ (5.2a) and a Cu(In,Ga)S_2 (5.2c) sample over an area of 60 μm × 60 μm corresponding to (300 × 300) spectra. Excitation with $\lambda = 532\,\mathrm{nm}$ and $\phi = 2.5 \times 10^4$ AM1.5 equivalent photon fluxes ($6.7 \times 10^{21}\,\mathrm{s}^{-1}\mathrm{cm}^{-2}$) at room temperature. Figure 5.2b and 5.2d show exemplary spectra and histograms of the PL yield J_γ. (samples from the same batch as $CuInS_2$ and Cu(In,Ga)S_2 a in table 2.1)

36]. Median $\widetilde{J}_\gamma = \exp M_L$ and standard deviation $\sigma_{J_\gamma} = \sqrt{\left(\mathrm{e}^{\sigma^2_{M_L}} - 1\right)\exp\left(2M_L + \sigma^2_{M_L}\right)}$ of figure 5.2 are $\widetilde{J}_\gamma = 0.32$, $\sigma_{J_\gamma} = 0.14$ for $\mathrm{CuInS_2}$ and $\widetilde{J}_\gamma \approx 0.67$, $\sigma_{J_\gamma} \approx 0.51$ for $\mathrm{Cu(In,Ga)S_2}$ (more details can be found in appendix B). That is a higher PL yield as well as larger variations in $\mathrm{Cu(In,Ga)S_2}$ compared to $\mathrm{CuInS_2}$.

Besides these lateral, strong spectral fluctuations — shown in the exemplary spectra in figure 5.2b and 5.2d — occur. Both peaks vary in intensity and energetic position. These fluctuations question the significance of the integral PL yield J_γ as a means to characterize CIS and CIGS absorber layers even in spatially highly resolved measurements. Instead the splitting of the quasi-Fermi levels reflected by the high energy wing of the PL spectrum are evaluated according to chapter 3.1.

5.1.1. Quasi-Fermi Level Splitting

The basis for a meaningful analysis of the photoluminescence spectrum is Planck's generalized law (eq. (3.7)), which allows the determination of the splitting of quasi-Fermi levels and thus giving an upper limit for the local open circuit voltage V_{oc}. For $\mathrm{CuInS_2}$ samples it is assumed that the quasi-Fermi level splitting $E_{Fnp}(x,y) = E_{Fn}(x,y) - E_{Fp}(x,y)$ varies only laterally and is fairly constant over the absorber thickness, since the analyses are performed under open circuit conditions, which provides for most "flat" carrier depth profiles. By numerical generation of PL signals including photon propagation, reflection at phase borders and interference effects, reabsorption, defect densities as well as depth dependent profiles of the band gap, one is able to study the influence of different profiles on the spectral behavior of the luminescence. This leads to the conclusion — mainly for the high photon energy wing of the PL — that in the vicinity of the heterojunction in the absorber in V_{oc} conditions no substantial departure from a "flat" profile of excess carrier concentration or say "flat" depth profile of the minority carrier quasi-Fermi level for reasonable parameters, e.g. surface recombination velocities $S < 10^4$ cm s^{-1}, may be detected [39, 50].

Since an accurate calibration of the laterally resolved measurements for absolute photon fluxes is not possible due to the high surface roughness and non negligible lateral variations of light coupling in and out, only fluctuations $\triangle_{(x,y)}E_{Fnp} = E_{Fnp}(x,y) - \chi$ are analyzed. Thus $\triangle_{x,y}E_{Fnp}$ and $T(x,y)$ have been fitted to the high energy wing of the PL spectrum according to eq. (3.12). To guarantee that eq. 3.12 can be applied, individual fitting ranges are determined for each spectra with respect to noise level and $A(x,y,\hbar\omega) \approx 1$.

Figure 5.3a shows a mapping of the fluctuation of quasi-Fermi level splitting $\triangle_{x,y}E_{Fnp}$ in $\mathrm{CuInS_2}$, the underlying data set corresponds to that of figure 5.2. Be-

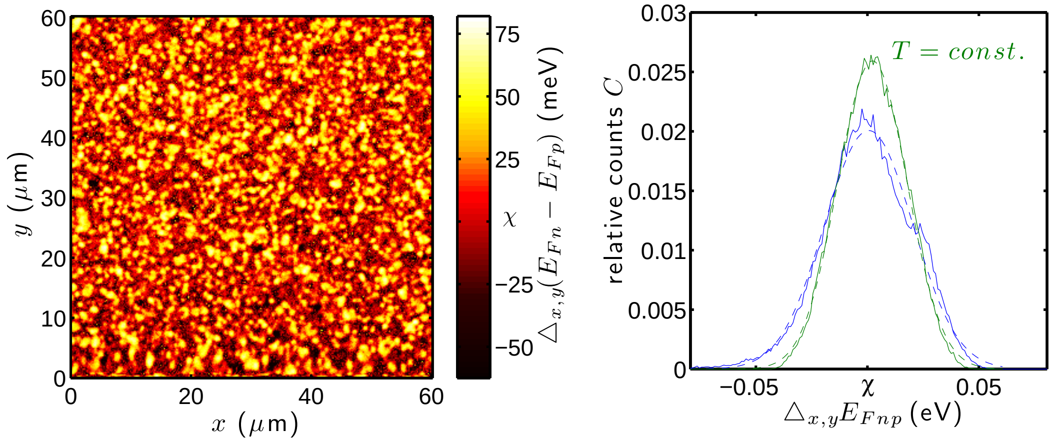

(a) $\triangle_{x,y}E_{Fnp}$ mapping

(b) $\triangle_{x,y}E_{Fnp}$ histogram

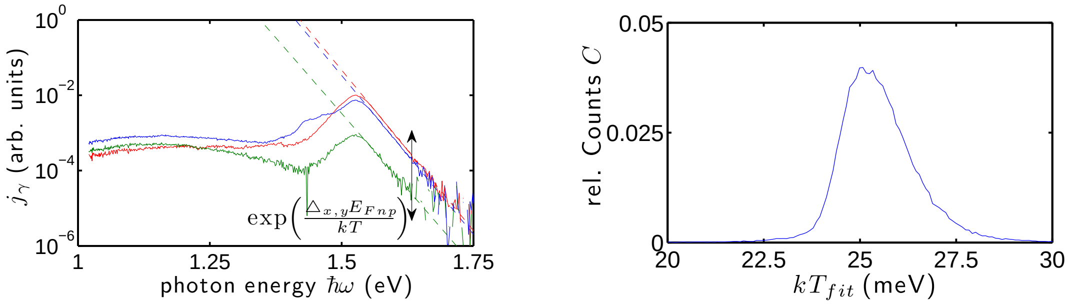

(c) spectra

(d) kT_{fit} histogram

Figure 5.3.: Variation in the quasi-Fermi level splitting of a $CuInS_2$ sample for the data set shown in figure 5.2. Figure 5.3a shows the mapping of $\triangle_{x,y}E_{Fnp}$, 5.3b is the histogram of $\triangle_{x,y}E_{Fnp}$ extracted from the experimental data set (blue). For comparison the histogram of $\triangle_{x,y}E_{Fnp}$ resulting from a fit with $T_{const.}$ = 293 K is also shown (green). 5.3d shows the variation in slope (fit with varying temperature), represented by the inverse slope kT_{fit}. Figure 5.3c displays exemplary and not necessarily representative spectra. The dashed lines represent the Bose term[1].

tween both mappings a correlation coefficient of $r(J_{\gamma,det}, \triangle_{x,y}E_{Fnp}) = 0.259$ with $r \in [-1,1]$ is found, thus the integral PL yield J_γ has only low significance for the opto-electronic absorber properties. Variations up to 100 meV with structure sizes in the micron range are observed. Figure 5.3c shows three exemplary spectra with fitted Bose terms[1]. A higher quasi-Fermi level splitting results in a shift of the Bose term as indicated in the figure, whereas a variation in sample temperature results mainly in a variation of the slope. The histogram of $\triangle_{x,y}E_{Fnp}$ (fig. 5.3b) shows a full width at half maximum of about $FWHM = 48\,\text{meV} \pm 5\,\text{meV}$. Figure 5.3d shows the variation in the inverse slope kT_{fit}, it is centered around $25.2\,\text{meV} \pm 0.3\,\text{meV}$ with $FWHM_{kT_{fit}} = 1.9\,\text{meV} \pm 0.3\,\text{meV}$. Although a small shoulder can be seen towards higher energies, the variations in $\triangle_{x,y}E_{Fnp}$ are well reproduced by a gaussian distribution with standard deviation $\sigma_{E_{Fnp}} = 19.8\,\text{meV}$. For comparison the variations resulting from a fit with $T = 293\,\text{K} = const.$ corresponding to $kT_{fit} = 25.2\,\text{meV}$ are also plotted in the histogram showing a $FWHM_{T_{const}} = 38\,\text{meV} \pm 4\,\text{meV}$. The shoulder seen in the temperature dependent fit disappears and the distribution can be described by a gaussian with $\sigma_{E_{Fnp},T=const.} = 15.6\,\text{meV}$. Both distributions, $\triangle_{x,y}E_{Fnp}$ and $\triangle_{(x,y),T=const.}E_{Fnp}$, are centered around the same average value. One possible reason for the discrepancy between distributions extracted from fits with $kT = const.$ and those with varying slope, is the uncertainty introduced by fitting the lattice temperature of the sample. Although local temperature variations might occur, e.g. due to different local defect densities, the extracted variations of $FWHM_{kT_{fit}} = 1.9\,\text{meV}$ corresponding to about $FWHM_{T_{fit}} = 22\,\text{K}$ are by far to high since it would mean that certain sample locations are beneath ambient temperature during measurement. Consequently variations in the inverse slope kT_{fit} represent the quality of the measurement and in particular the signal to noise ratio. In Cu(In,Ga)Se$_2$ samples smaller variations in $\triangle_{(x,y),T=const.}E_{Fnp}$ in the range of 13 meV to 16 meV for similar excitation fluxes and experimental conditions were reported [20, 21].

To analyze influences of the rough surface on PL yields and quasi-Fermi level splittings, samples have been marked and AFM measurements have been carried out at identical positions (see figs. 5.4).

Although certain features can be identified in all mappings no significant correlation between PL yield $J_{\gamma,det}$ or quasi-Fermi level splitting $\triangle_{x,y}E_{Fnp}$ and AFM surface contour $h(x,y)$ can be found. Correlation coefficients are $r(J_{\gamma,det}, h) = 0.277$ and $r(\triangle_{x,y}E_{Fnp}, h) = 0.243$ with $r \in [-1,1]$ and have been calculated without the

---

[1] For a better comparison all spectra are plotted semi-logarithmically, thus the Bose term shown in the plot equals $\exp(B(\hbar\omega)) \cdot (\hbar\omega)^2$.

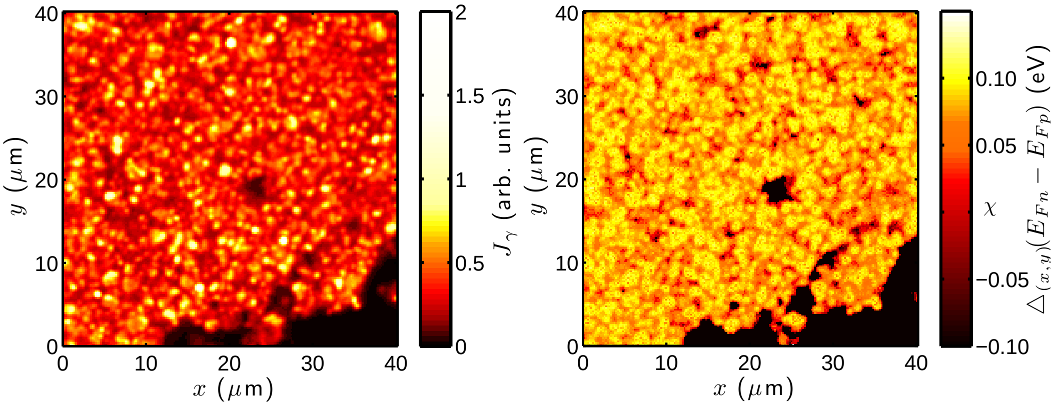
(a) Integral photon flux J_γ

(b) $\triangle_{x,y}E_{Fnp}$

(c) Surface contour

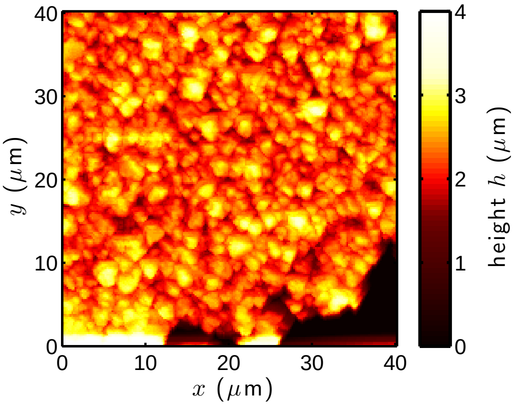

Figure 5.4.: Integral photoluminescence $J_{\gamma,det}$, $\triangle_{x,y}E_{Fnp}$ and surface contour h. The sample has been marked to guarantee identical positions.

marked areas seen in the figures. Accordingly the variation of the absorber thickness has a negligible influence on the detected PL spectra. To verify that light coupling in and out, e.g. higher emission from peaks, has no effect on the PL, correlation to the surface contour $|h|$ are calculated and found to be $r(J_{\gamma,det},|h|) = -0.013$ and $r(J_{\gamma,det},|h|) = 0.003$. In conclusion, variations measured have to be caused by laterally varying opto-electronic sample properties, e.g. defect densities, absorption coefficients, band-gaps, etc. rather than by the surface contour.

When analyzing Cu(In,Ga)S$_2$ absorber layers the graded band-gap described in chapter 2 and 3.1.2 with a higher E_g at the Mo back contact has to be taken into account. It has been shown, that an approximation of the high energy wing of a sample with a thick high band-gap region close to the back contact and a high intermixture of Ga rich and In rich region would lead to a larger slope ($> -1/kT$) of the Bose term (see chapter 3.1.2). This translates into a temperature T_{fit} above the actual sample temperature T and thus the extracted quasi-Fermi level splitting of the regime close to the surface of the semiconductor would be underestimated. On the other hand, a strong gradient $E_{Fnp}(z)$ in the low band-gap region close to the surface could lead to a slope $< -1/kT$ in the extracted Bose term, which translates into a temperature T below the ambient temperature and an overestimation of $\triangle_{x,y} E_{Fnp}$. So the extracted slope contains information about the intermixture of the two (Ga rich and In rich) regimes. For a photoluminescence scan of a sample this would mean, the higher the slope variations, the higher the intermixture between both regimes or the larger the gradient in $E_{Fnp}(z)$ and the larger the error in the extracted quasi-Fermi level splitting. But in reality it's hard to distinguish between slope variations caused by a varying intermixture of the two regions and slope variations that are caused by a variation of opto-electronic properties (e.g. lateral variation of band-gap, absorption coefficient etc.). Since a higher variation in the fitted slope could be caused by a fitting region that is not appropriately chosen, e.g. if the fit is carried out beneath the range where $A \approx 1$.

Under these prerequisites the variation in the quasi-Fermi level splitting $\triangle_{x,y} E_{Fnp}$ is extracted from the photoluminescence of a Cu(In,Ga)S_2 sample. Figure 5.5a shows a mapping of $\triangle_{x,y} E_{Fnp} = \triangle_{x,y}(E_{Fn} - E_{Fp})$ for the data set presented in figure 5.2. Maximum variations of more than 200 meV are observed. Three examples of the fitted spectra can be found in figure 5.5c showing strong spectral fluctuations. The resulting distribution of $\triangle_{x,y} E_{Fnp}$ (figure 5.5b with 5.5d) is much broader than in the case of pure CuInS_2. For temperature dependent fits the full width at half maximum is $\text{FWHM}_{\triangle_{x,y} E_{Fnp}} = 79\,\text{meV} \pm 5\,\text{meV}$ with $\overline{kT_{fit}} = 25.6\,\text{meV}$ and $\text{FWHM}_{kT_{fit}} = 2.8\,\text{meV} \pm 0.3\,\text{meV}$. For $kT = const.$ (green in fig. 5.5b) the distribution is much narrower, $\text{FWHM}_{T=const.} = 53\,\text{meV} \pm 4\,\text{meV}$. Both distributions are well described by a gaussian with $\sigma_{E_{Fnp}} = 33.6\,\text{meV}$ and $\sigma_{E_{Fnp},T=const.} = 22.8\,\text{meV}$, respectively. The large discrepancy between temperature dependent and constant temperature fit is caused by larger spectral variations and by depth dependent band-gaps and quasi-Fermi level splittings in Cu(In,Ga)S_2, that lead to a higher error in the fitted slope. The asymmetry of the extracted slopes as well as the significant occurrence of values < 25 meV (that is beneath ambient temperature) points towards a varying gradient in band-gap and quasi-Fermi level splitting.

The high energy wing of the low band-gap regime can be measured over more than two orders of magnitude, whereas no PL from the high band-gap regime of the

(a) $\triangle_{x,y}E_{Fnp}$ mapping

(b) $\triangle_{x,y}E_{Fnp}$ histogram

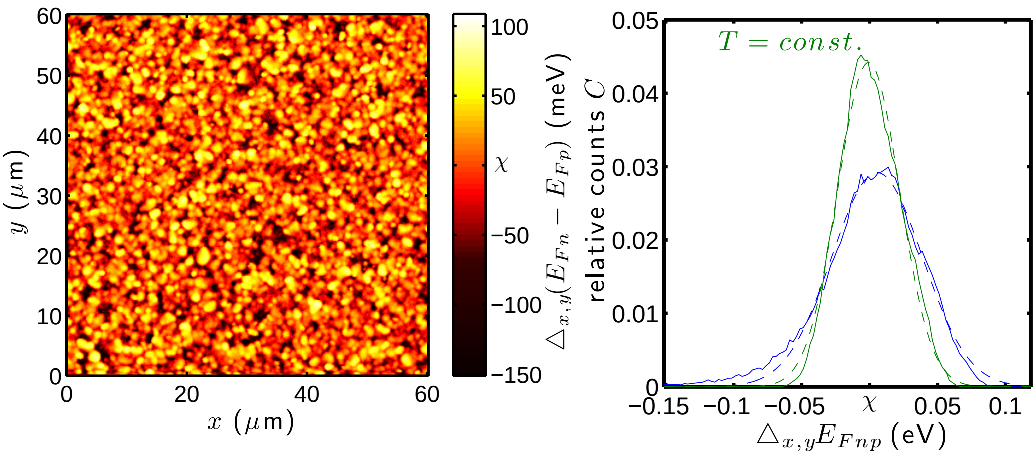

(c) spectra

(d) kT_{fit} histogram

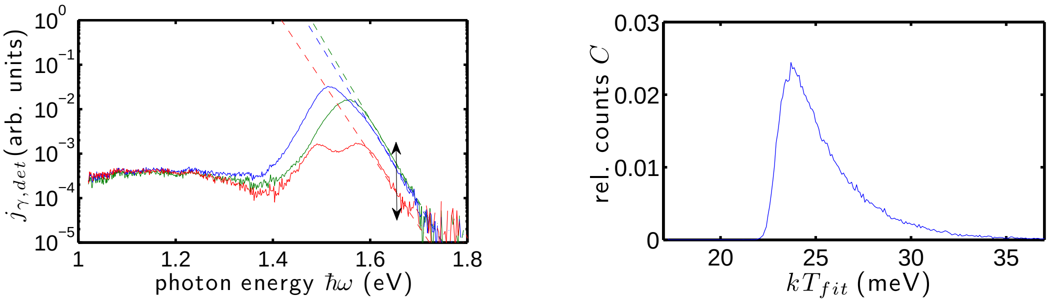

Figure 5.5.: Variation in the quasi-Fermi level splitting of a Cu(In,Ga)S_2 sample for the data set shown in figure 5.2. Figure 5.5a shows the mapping of $\triangle_{x,y}E_{Fnp}$, 5.5b is the histogram of $\triangle_{x,y}E_{Fnp}$ fitted with varying temperature (blue) and constant temperature $T_{const.} = 297\,\mathrm{K}$ (green). Figure 5.5d shows the variation in slope (fit with varying temperature) represented by the inverse slope kT_{fit}. Figure 5.5c displays exemplary and not necessarily representative spectra from the marked positions. The dashed lines represent the Bose term[1].

absorber layer can be detected due to reabsorption. Single spectra with two band-to-band peaks (red spectrum in figure 5.5c) could be caused by two PL centers with different band-gaps lying next to each other or by a large band-gap region close to the absorber surface (analogously to figure 3.4c).

A comparison between the variations $\triangle_{x,y}E_{Fnp}$ of $\mathrm{CuInS_2}$ and $\mathrm{Cu(In,Ga)S_2}$ is displayed in figure 5.6. PL scans have been carried out at different sample positions under equivalent conditions with an excitation of 3×10^4 suns equivalent fluxes. Variations have been extracted with $kT = const.$. Since the offset χ is constant the distributions are directly comparable. Although $\mathrm{Cu(In,Ga)S_2}$ has with $\overline{\mathrm{FWHM}_{CIGS}} = 52\,\mathrm{meV}$ a higher variation than $\mathrm{CuInS_2}$ ($\overline{\mathrm{FWHM}_{CIS}} = 34\,\mathrm{meV}$) the absolute quasi-Fermi level splitting in $\mathrm{Cu(In,Ga)S_2}$ is in average about 70 meV higher. This is also reflected in parameters of cells with nominally identical absorber layers — that is, cells from the same batch — which show an open circuit voltage V_{oc} in average about 115 mV higher (see chapter 2).

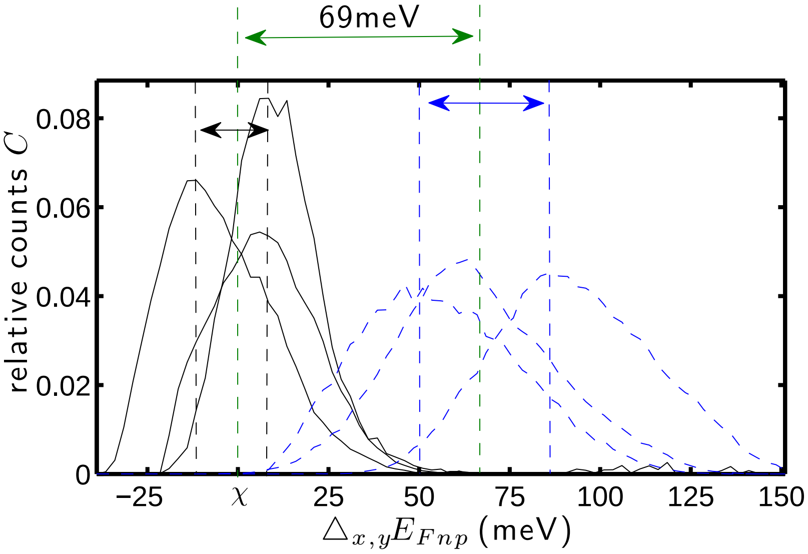

Figure 5.6.: Histograms $\triangle_{x,y}E_{Fnp}$ of $\mathrm{CuInS_2}$ (black) and $\mathrm{Cu(In,Ga)S_2}$ (blue)measured with an excitation of 3×10^4 suns equivalent fluxes at different positions.

5.1.2. Absorbance, Band-Gap and Defects

Besides quasi-Fermi level splitting $\triangle_{x,y}E_{Fnp}$, the absorbance $A(x, y, \hbar\omega)$ of the material can be calculated with the help of Planck's generalized law (eq. (3.13)) and the considerations made in section 3.1.1 and 3.1.2. Furthermore the assumption that initial states in conduction band are unoccupied and final states in valence band and defects (acceptors) are occupied is made. Details on this topic will be discussed in section 5.1.5 and 5.3.2. Figure 5.7 shows three exemplary absorbance spectra for $CuInS_2$ and $Cu(In,Ga)S_2$ in a semi-logarithmic plot. It has to be noted that the absorbances $A(x, y, \hbar\omega)$ shown include multiple reflections as well as thickness variations according to eq. (3.8). The absorbance can be determined over ten orders of magnitude and for all analyzed samples a substantial lateral and spectral variation in the absorption properties is found. For $Cu(In,Ga)S_2$ samples with low and high band-gap regimes, the extracted absorbances are an average across the thickness over the low band-gap regime close to the absorber surface (see sections 3.1.2 and 5.1.1).

To analyze the absorbance in more detail figure 5.8 shows three absorbance spectra calculated from the PL of a $CuInS_2$ sample in a linear and semi-logarithmic plot (data set is the same as of figures 5.2 and 5.3). Although the presented spectra are not

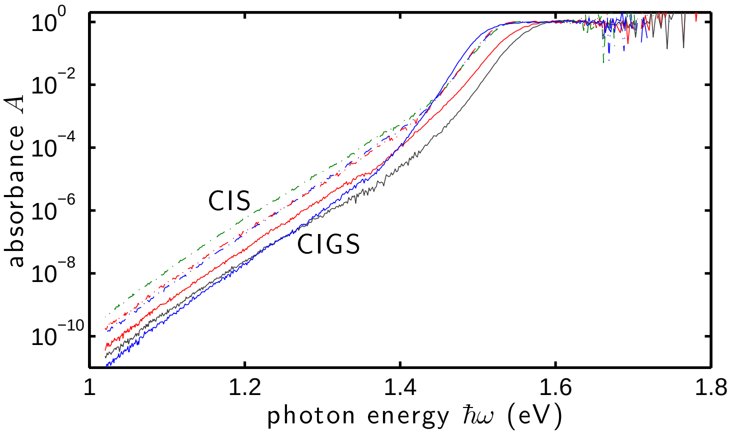

Figure 5.7.: Exemplary absorbance spectra of $CuInS_2$ (dashed) and $Cu(In,Ga)S_2$ (solid) calculated from laterally resolved photoluminescence measurements.

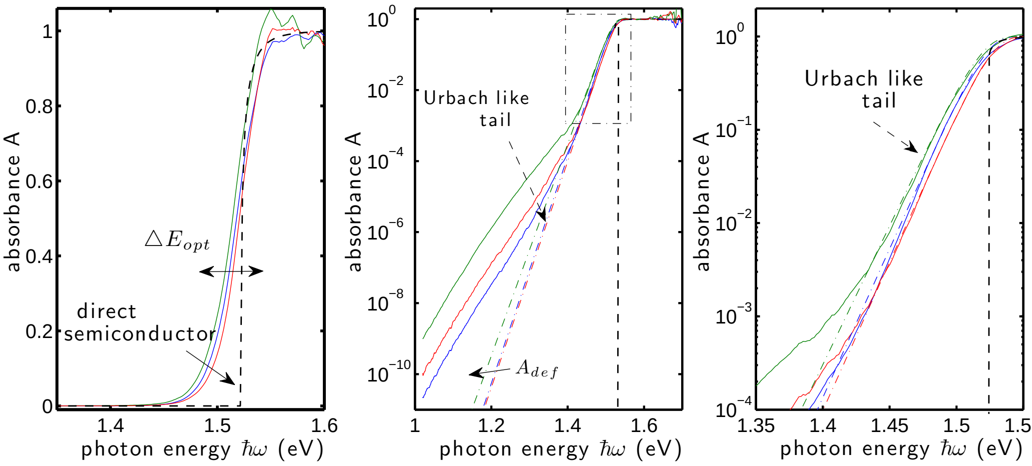
(a) linear plot (b) semi-logarithmic plot (c) detail

Figure 5.8.: Exemplary absorbance spectra of $CuInS_2$, 5.8a shows a linear plot, the dashed line represents the absorbance spectrum of an ideal direct semiconductor. 5.8b, same spectra in a semi-logarithmic plot with fitted Urbach like tail. The sub band-gap absorbance is defined by $A_{def}(x,y) = \int_0^{1.35eV} A(x,y,\hbar\omega)\mathrm{d}(\hbar\omega)$. 5.8c shows a detail of the marked area in 5.8b. The underlying data set corresponds to figures 5.2 and 5.3.

representative, they are consulted to visualize the method. Since $Cu(In_{1-\xi}Ga_{\xi})S_2$ is — as described in chapter 2 — a direct semiconductor, the comparison of the measured spectra to that of an ideal direct semiconductor according to $A_{id} = 1 - e^{-\alpha_{id}\overline{d}}$ with $\alpha_{id} = \frac{a}{\hbar\omega}\sqrt{\hbar\omega - E_g}$ is obvious (dashed line in figs. 5.8). Because no correlation between variations in thickness d and the high energy wing of the PL in terms of the quasi-Fermi level splitting has yet been found, the average thickness of the layer $\overline{d}$ is used. Multiple reflections can be neglected since an ideal direct semiconductor has a steep absorption edge. In contrast to this, no steep absorption edge is observed in the measured spectra, thus the difference is assumed to be caused by tail and defect states deeper in the gap. As a result no fit of A_{id} an no direct extraction of the band-gap $E_g(x,y)$ is possible. Instead, the optical threshold or optical band-gap

$$E_{opt}(x,y) = E_g(x,y) + E'(d(x,y)) + E'', \tag{5.2}$$

defined as the energy, for which the absorbance has dropped by 1/e, is calculated. In doing so, the argumentation of Gütay [21] is met and E'' is assumed to be the constant offset. Since these samples exhibit high thickness variations, $E'(d(x,y))$ takes account for fluctuations due to variations in d. Consequently, if $E'(d(x,y))$ is negligible, lateral variations in E_{opt} correspond to lateral band-gap variations $\triangle_{(x,y)}E_{opt} \approx \triangle_{(x,y)}E_g$.

Figure 5.9a and 5.9b show a mapping of $E_{opt}(x,y)$ for a $CuInS_2$ and a $Cu(In,Ga)S_2$ sample. The variations and the average optical band-gap $\overline{E_{opt}}$ can be extracted from the histograms (figures 5.9c and 5.9d), for $CuInS_2$ it is $\overline{E_{opt}} = 1.51\,eV$ with $FWHM_{E_{opt}} = 7\,meV \pm 2\,meV$ and for $Cu(In,Ga)S_2$ $\overline{E_{opt}} = 1.53\,eV$ with $FWHM_{E_{opt}} = 80\,meV \pm 4\,meV$. Besides the much larger variations in $Cu(In,Ga)S_2$, the distribution of E_{opt} has two maxima. Both peaks can be described by gaussian distributions with optical band-gaps of $\overline{E_{opt,1}} = 1.5\,eV$ and $\overline{E_{opt,2}} = 1.55\,eV$ and standard deviations $\sigma_{E_{opt},1} = 18\,meV$ and $\sigma_{E_{opt},2} = 13\,meV$. These two maxima point towards the existence of two distinct phases, one with an optical threshold of 1.55 eV and presumably higher Ga content and another with an optical threshold of 1.5 eV and low or no Ga content in the region close to the surface. It has to be noted, that not all of the analyzed $Cu(In,Ga)S_2$ samples show two distinct maxima.

Between $E_{opt}(x,y)$ and $\triangle_{x,y}E_{Fnp}$ in $Cu(In,Ga)S_2$ a correlation of $r(E_{opt}, \triangle_{x,y}E_{Fnp}) \approx 0.53$ with $r \in [-1,1]$ is found, so a higher optical band-gap E_{opt} or higher band-gap E_g leads to a higher quasi-Fermi level splitting. A reason why no higher correlation is measured is the influence of the absorber thickness on the optical band-gap or in other words the lateral fluctuation of $E'(d(x,y))$ in eq. (5.2). To estimate the effect of thickness variations on $E_{opt}(x,y)$ the absorption coefficient $\alpha(x,y,\hbar\omega)$ has been extracted for $CuInS_2$ and $Cu(In,Ga)S_2$ with Lambert-Beers law using a constant thickness $\overline{d}$. The absorbance $A(x,y,\hbar\omega)$ has then been recalculated using an alteration in thickness d'. Figure 5.9e shows exemplary $Cu(In,Ga)S_2$ absorbance spectra for $d' = \overline{d} \pm 350\,nm$ (red dashed line) and $d' = \overline{d} \pm 525\,nm$ (black dashed line) — corresponding to the thickness variations in $Cu(In,Ga)S_2$ (see chapter 2.2). A higher thickness d increases the absorbance in the spectral range with low absorption coefficient — that is, the absorption by tail and defect states. In spectral ranges with high α the absorbance is saturated anyway, so no change is observed. Fluctuations with $FWHM_d = 800\,nm$ ($\overline{d} \pm 400\,nm$) in $CuInS_2$ lead to variations in $E'(d(x,y))$ of $\triangle_{x,y}E' \approx 5.9\,meV$ or $\triangle_{x,y}E' \approx 8.6\,meV$, if also thickness fluctuations of the undersurface with $FWHM_d = 345\,nm$ are taken into account (see chapter 2.2). The values for $\triangle_{x,y}E'$ have been averaged over all 90000 spectra of a scan. Thus in the same magnitude as $\triangle_{x,y}E_{opt}$, in conclusion local band-gap variations in $CuInS_2$ are negligibly small or at least not measurable with the current experimental setup. For $Cu(In,Ga)S_2$ with thickness fluctuations of $FWHM_d = 700\,nm$ ($\overline{d} \pm 350\,nm$) the

(a) $CuInS_2$ E_{opt} mapping

(b) $Cu(In,Ga)S_2$ E_{opt} mapping

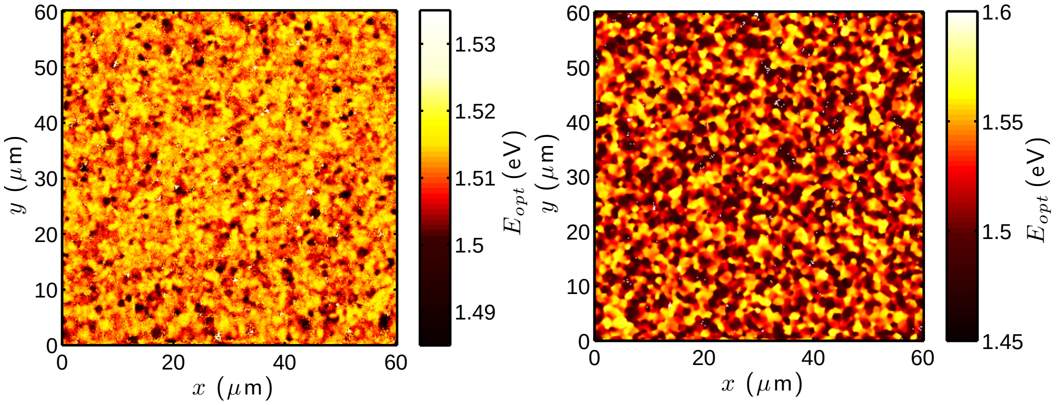

(c) $CuInS_2$ E_{opt} histogram

(d) $Cu(In,Ga)S_2$ E_{opt} histogram

(e) Spectra

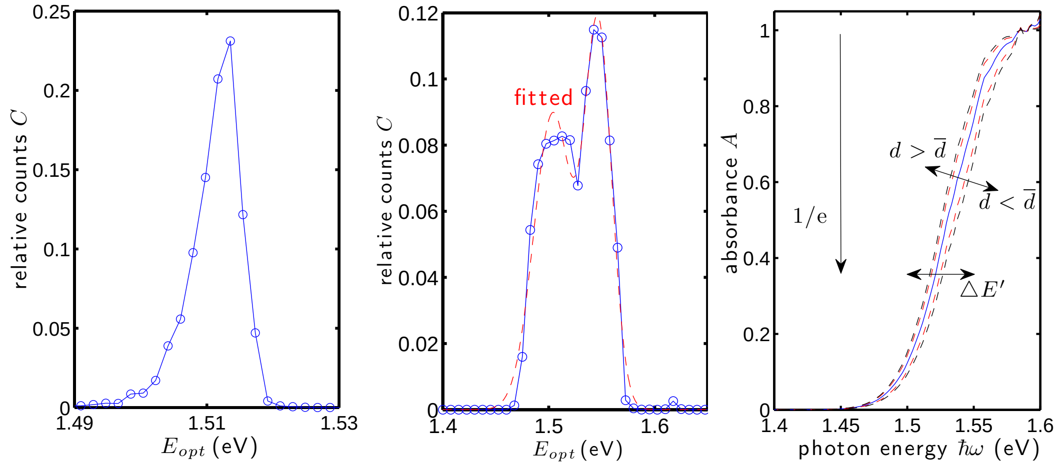

Figure 5.9.: Mapping and histogram of the optical band-gap E_{opt}, which is defined as the point where the absorbance A has dropped to 1/e. Dataset correspond to figures 5.2.

variations of $\triangle_{x,y}E' \approx 7.3\,\text{meV}$ ($\triangle_{x,y}E' \approx 10.7\,\text{meV}$ with $\text{FWHM}_d = 320\,\text{nm}$ of the undersurface) are much smaller than the measured fluctuations in the optical band-gap. Thus the “band-gap” E_g of the analyzed $Cu(In,Ga)S_2$ sample varies with about $\triangle_{x,y}E_g \approx 70\,\text{meV}$ (FWHM, $\sigma_{E_g} \approx 25\,\text{meV}$).

Rau et al. [22] have analyzed the impact of local band-gap fluctuations on the performance of a solar cell and found a decrease in efficiency of about 1.7% for

$\sigma_{E_g} = 50\,\mathrm{meV}$ (3.5% for $\sigma_{E_g} = 75\,\mathrm{meV}$ and 6.1% for $\sigma_{E_g} = 100\,\mathrm{meV}$).

To provide a more detailed description of the absorption edge beneath the optical threshold E_{opt}, the ansatz of an Urbach like tail according to [51]

$$\alpha_{urb} = \alpha_0 \mathrm{e}^{\frac{\hbar\omega - E_0}{E_u}} \tag{5.3}$$

is made, with a decay energy $E_u(x,y)$, which is a function of the structural disorder of the material, and parameters $E_0(x,y)$ and $\alpha_0(x,y)$. The spectra can be fitted by calculating the absorbance $A_{urb} = 1 - e^{-\alpha_{urb}\overline{d}}$. A detail of the fitted spectra is shown in figure 5.8c. Figure 5.10 shows a histogram of the laterally fluctuating magnitude E_u for CuInS$_2$ and Cu(In,Ga)S$_2$. The absorption tails are well reproduced with decay energies $\overline{E_u} = 15.2\,\mathrm{meV} \pm 3.0\,\mathrm{meV}$ (CuInS$_2$) and $\overline{E_u} = 14.3\,\mathrm{meV} \pm 4.2\,\mathrm{meV}$ (Cu(In,Ga)S$_2$). Although the influence of thickness fluctuations on the PL spectrum become larger towards lower photon energies, a procedure similar to figure 5.9d revealed no influences on the decay energy E_u by variations in d. In the literature decay energies of about 25 meV in CuInS$_2$ have been reported [52].

To study laterally varying deep defect states concentrations, the lower energy range of the absorbance spectra (fig. 5.8) has been analyzed. Correctly, the defect absorbance A_{def} has been defined as the difference between measured absorbance A and fitted Urbach A_{urb} absorbance. But since small errors in A_{urb} would lead to

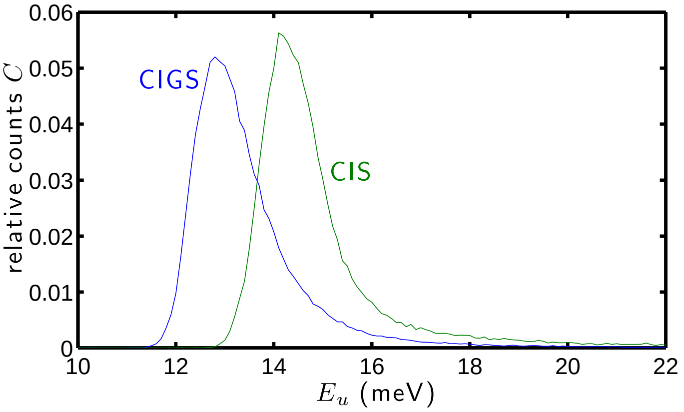

Figure 5.10.: Histogram of the decay energy E_u according to eq. (5.3). Data set correspond to figures 5.2.

large deviations in A_{def} due to the difference in magnitudes, the defect absorbance is calculated by

$$A_{def}(x,y) = \int_{0}^{1.35\,\mathrm{eV}} A(x,y,\hbar\omega)\mathrm{d}\hbar\omega. \tag{5.4}$$

Mapping and histogram of A_{def} are shown in figure 5.11. Structure sizes found in the mapping correspond to structure sizes in the quasi-Fermi level splitting, the distribution of absorbances by defect states (figure 5.11c and 5.11d) is asymmetric with higher A_{def} occurring more seldom. For CuInS$_2$ and Cu(In,Ga)S$_2$ the distributions A_{def} can be described by a log-normal distribution according to eq. (B.1) in the appendix, with $\sigma_{A_{def},CIS} \approx 0.0036$ and $\sigma_{A_{def},CIGS} \approx 0.057$ according to eq. (B.2). Thus

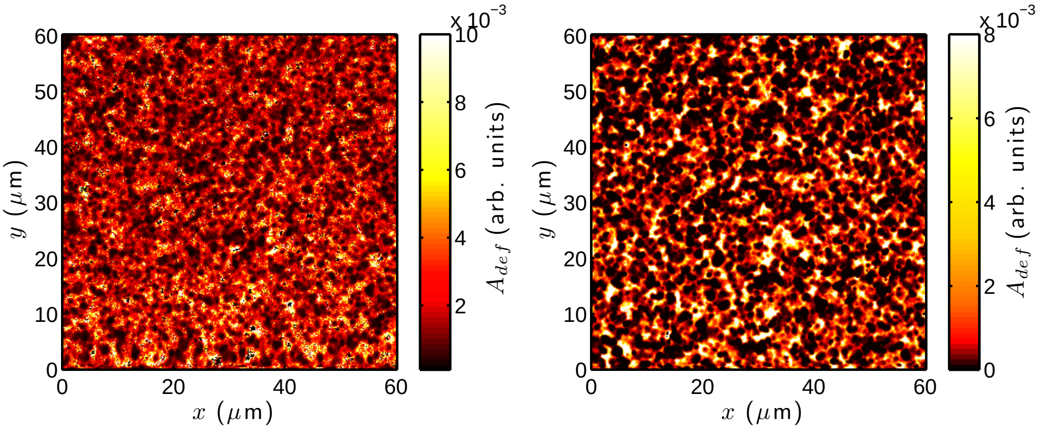
(a) CuInS$_2$ defect absorbance A_{def}

(b) Cu(In,Ga)S$_2$ defect absorbance A_{def}

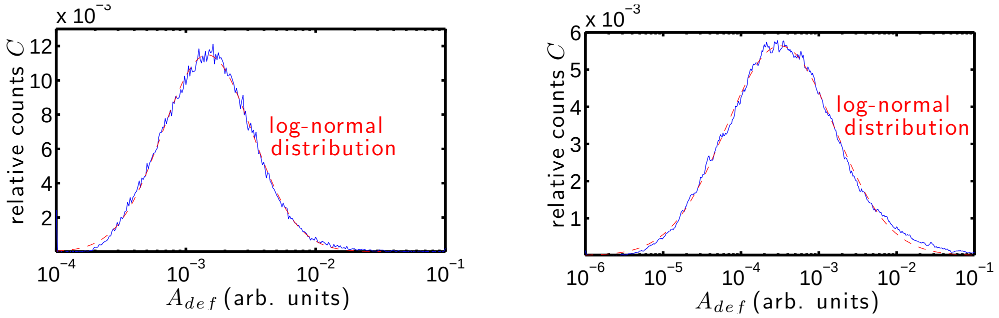
(c) CuInS$_2$ A_{def} histogram

(d) Cu(In,Ga)S$_2$ A_{def} histogram

Figure 5.11.: Mapping (5.11a and 5.11b) and histograms (5.11c and 5.11d) of the absorbance via defect states $A_{def} = \int_0^{1.35\,\mathrm{eV}} A(x,y,\hbar\omega)\mathrm{d}\hbar\omega$.

a higher variation of sub band-gap absorbance in Cu(In,Ga)S$_2$, which is assumed to be proportional to the density of defect states $A_{def} \propto N_D$.

The sub band-gap absorbance shows a clear anti-correlation of $r(A_{def}, \triangle_{x,y}E_{Fnp}) \approx -0.79$ with $r \in [-1, 1]$ to the local quasi-Fermi level splitting $\triangle_{x,y}E_{Fnp}$ in CuInS$_2$ and $r(A_{def}, \triangle_{x,y}E_{Fnp}) \approx -0.69$ in Cu(In,Ga)S$_2$. This indicates a lowering of the local quasi-Fermi level splitting and a decrease in the local minority carrier lifetime $\tau(x, y)$ by increase in local sub band-gap defects, obviously due to a considerable contribution of these defects to recombination. A similar analysis has been performed by Ostapenko et al. [53, 54] in multicrystalline silicon, who found an anti-correlation between the local defect PL and the local minority carrier lifetime. It has to be noted that no direct correlation between the integral values $J_{\gamma,def}(x, y) = \int_0^{1.35\,\mathrm{eV}} j_{\gamma,det}(x, y, \hbar\omega)\mathrm{d}\hbar\omega$ (entire PL yield in the lower energy range) and $\triangle_{x,y}E_{Fnp}$ occurs, since a variation in quasi-Fermi level splitting leads to a variation in the overall PL yield as described in chapter 3.1. In other words, if $A_{def}(x, y)$ was constant an increase in quasi-Fermi level splitting would result in a higher luminescence yield and a higher $J_{\gamma,def}(x, y)$. A separation of these two competing effects, as it is carried out by the calculation of the local absorbance, is therefore necessary.

The measured anti-correlation can be described by a simple model. According to eq. (3.1) electron and hole densities are given by

$$\begin{aligned} n &= \Delta n + n_0 = N_c \exp\left[-\frac{E_c - E_{Fn}}{kT}\right] \\ \text{and} \qquad p &= \Delta p + p_0 = N_v \exp\left[-\frac{E_{Fp} - E_v}{kT}\right]. \end{aligned} \tag{5.5}$$

Where n_0, p_0 are electron (hole) density under thermal equilibrium conditions and Δn, Δp are the excess carrier concentrations. From equations 5.5 the quasi-Fermi level splitting can be deduced as

$$E_{Fn} - E_{Fp} = kT \ln\left(\frac{(\Delta n + n_0)(\Delta p + p_0)}{n_0 p_0}\right). \tag{5.6}$$

In a p-type semiconductor the quasi-Fermi level for holes is almost constant $E_{Fp}(x, y) \approx const.$, consequently lateral variations in the quasi-Fermi level splitting are caused by variations in $E_{Fn}(x, y)$

$$\begin{aligned} \triangle_{(x,y)}\left(E_{Fn} - E_{Fp}\right) \approx \triangle_{(x,y)}E_{Fn} &= kT \ln\left(\frac{\triangle_{x,y}\Delta n + n_0}{n_0}\right) \\ &\approx kT \ln\left(\frac{\triangle_{x,y}\Delta n}{n_0} + 1\right) \end{aligned} \tag{5.7}$$

with $\Delta n \gg n_0$. Under stationary conditions the excess carrier density depends on generation rate G and lifetime $\tau = {}^{C_1}/_{N_D}$, which in turn depends on the defect density N_D, so $\Delta n = \tau G = C_1 G/N_D$ and eq. (5.7) becomes

$$\triangle_{x,y} E_{Fn} \approx -kT \ln\left(\frac{n_0 \triangle_{x,y} N_D}{GC_1}\right) = -kT \ln\left(C_2 \triangle_{x,y} N_D\right), \qquad (5.8)$$

with $C_2 = n_0/(GC_1) \approx const.$. Figure 5.12a and 5.12b show a semi-logarithmic plot of $\triangle_{x,y} E_{Fnp}$ in dependence of the defect absorbance $A_{def}(x,y) \propto N_D(x,y)$, the slopes calculated from a fit according to eq. (5.8) are −22 meV ($CuInS_2$) and −21 meV ($Cu(In,Ga)S_2$). Although a slope of −26 meV would be expected for room temperature (300 K) a good agreement is found considering the errors entering the data analysis and the simplifications made in eq. (5.8).

In the literature different ionization energies of non identified deep defects in $CuInS_2$ and $Cu(In,Ga)S_2$ have been reported [55, 56]. By the use of Brewster-angle spectroscopy (BAS) at room temperature, Lewerenz and co-workers [57] have found two deep defect states in n-type $CuInS_2$ single crystals at $D_1 = 350$ meV and $D_2 = 625$ meV above the valence band. Similar energies of about 370 meV have been found by admittance spectroscopy in p-type Ga doped samples with a preparation process similar to the analyzed $Cu(In,Ga)S_2$ samples [58]. It has to be noted, that these energies have been extracted without sufficient lateral resolution, they are averaged over a large area. In the case of admittance spectroscopy

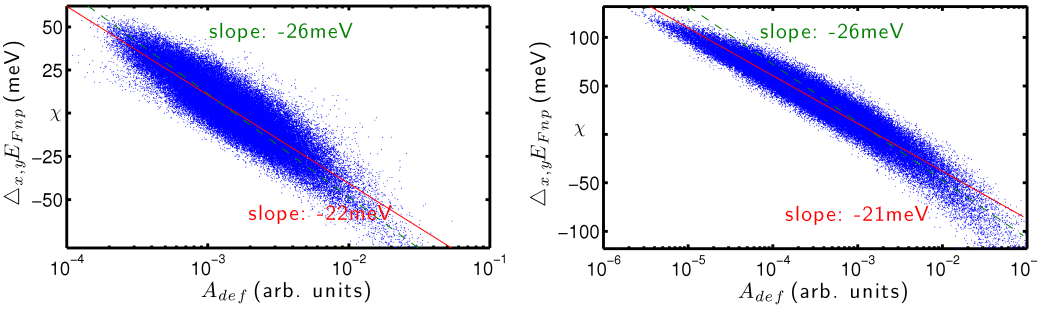
(a) $CuInS_2$

(b) $Cu(In,Ga)S_2$

Figure 5.12.: Fluctuations in quasi-Fermi level splitting $\triangle_{x,y} E_{Fnp}$ depending on the local defect absorbance $A_{def}(x, y, \hbar\omega)$. Slopes have been extracted with natural logarithm according to eq. (5.8).

over the area of a cell ($0.5\,\mathrm{cm}^2$). In order to extract an energy for the broad "defect band" causing the sub band-gap luminescence in the analyzed samples, the energy difference between optical band-gap E_{opt} according to figure 5.9 and energy of the maximum defect luminescence $E_{def,max}$ has been extracted. In $\mathrm{CuInS_2}$ the extracted optical band-gap is 1.511 eV which corresponds to band-gap measurements of $E_g = 1.52\,\mathrm{eV}$ on similar absorber layers [59]. Thus in a good approximation $E'' \approx 0$ and $E_g(x,y) \approx E_{opt}(x,y) - E'(d(x,y))$. For small variations $E'(d(x,y))$ is therefore $E_g(x,y) - E_{def,max}(x,y) \approx E_{opt}(x,y) - E_{def,max}(x,y)$. Figure 5.14a shows the occurrence of $E_{opt} - E_{def,max}$ in a $\mathrm{CuInS_2}$ PL scan. The energy of the maximum defect luminescence $E_{def,max}$ has been determined by fitting a gaussian distribution to the defect luminescence $j_{\gamma,def}(x,y,\hbar\omega)$ for $\hbar\omega \leq 1.35\,\mathrm{eV}$. With high probability a defect energy of 355 meV with FWHM = 45 meV occurs. This corresponds to the energy of defect D_1 above the valence band, whereas defect D_2 is far below the detected PL spectrum. In $\mathrm{Cu(In,Ga)S_2}$ this procedure is aggravated by high band-gap fluctuations which introduce additional errors. The average optical band-gap is $\overline{E_{opt}} \approx 1.53\,\mathrm{eV}$ with two maxima at 1.5 eV and 1.55 eV. Since band-gap measurements of similar $\mathrm{Cu(In,Ga)S_2}$ layers have shown an average band-gap of 1.53 eV the analysis is carried out analogously to $\mathrm{CuInS_2}$, assuming that close to the surface a $\mathrm{Cu(In,Ga)S_2}$ layer with very low Ga content exists. Figure 5.14b shows the energy difference $E_{opt} - E_{def,max}$ for $\mathrm{Cu(In,Ga)S_2}$. The energy of 375 meV occurring with highest probability corresponds to the defect level determined in [58] on similar absorbers[2]. A more profound analysis of shallow defects can be carried out by mea-

---

[2] With FWHM = 90 meV the location of the deep defect in $\mathrm{Cu(In,Ga)S_2}$ shows larger variations which can partly be explained by the fluctuating band-gap E_g.

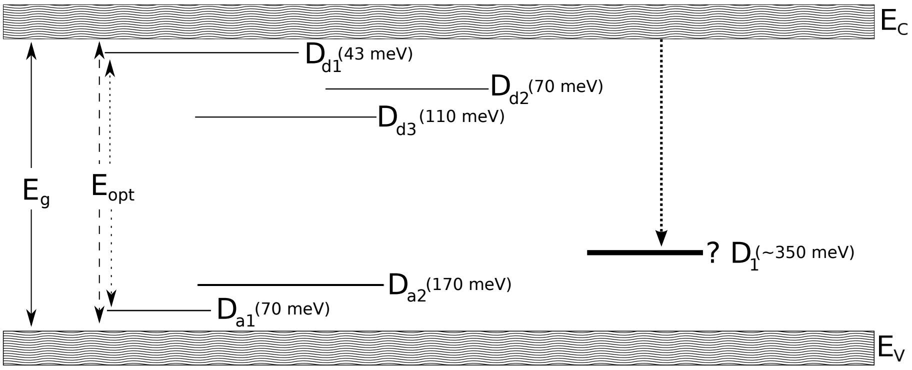

Figure 5.13.: Energy level diagram for $\mathrm{CuInS_2}$ according to [57] and [55].

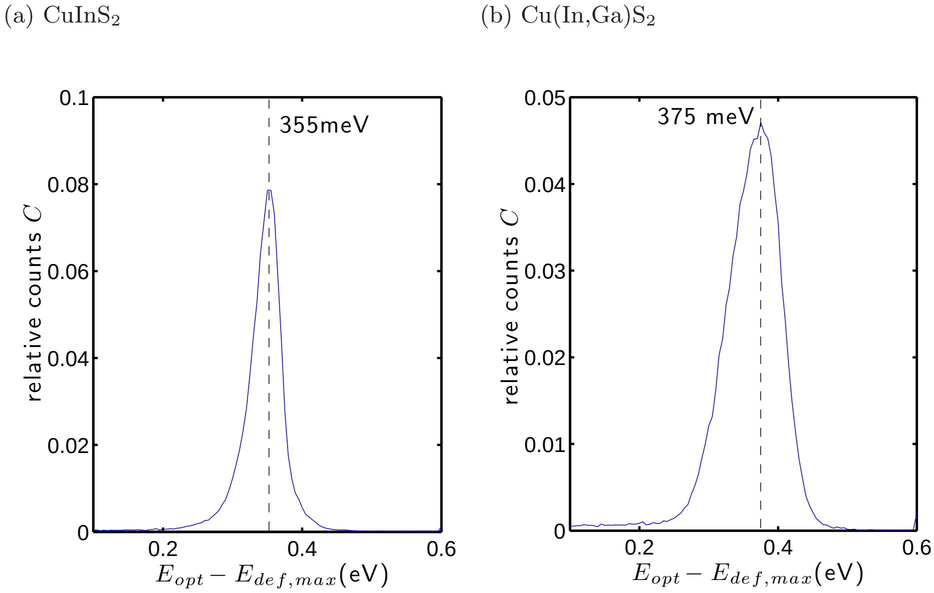

Figure 5.14.: Energy difference between optical band-gap E_{opt} and energy of defect maximum in the photoluminescence $E_{def,max}$. Shown in 5.14a and 5.14b are the occurrences (relative counts C) for CuInS$_2$ and Cu(In,Ga)S$_2$ depending on $E_{opt} - E_{def,max}$.

suring photoluminescence at low temperatures and shall be reported on in the next chapter.

5.1.3. Defect Analysis by Low Temperature Photoluminescence

Photoluminescence and other analyses have shown that CuInS$_2$ tends to form numerous types of intrinsic defects. In most cases three donor and two acceptor levels are mentioned (see sketch of the energy level diagram in figure 5.13). Since an exact classification of these defects (e.g. sulfur vacancy V_S, indium interstitial In_i etc.) is still controversial it will not be given here, for further details see [55,57,60–67].

The laterally resolved photoluminescence at low temperatures $80\,\text{K} \leq T_{cryo} \leq 130\,\text{K}$has been measured in the experimental setup described in chapter 4.1 with a liquid nitrogen cryostat for sample cooling. Due to the cryostat a microscope objective with a larger working distance and a smaller resolution had to be used. The sample was excited with a 20 mW Helium-Neon laser at $\lambda = 632.8\,\text{nm}$, given temperatures T_{cryo} are measured in the cooling finger of the cryostat. Figure 5.15 shows mappings of the integrated PL yield J_γ of a Cu(In,Ga)S_2 absorber at T_{cryo} = 85 K (5.15a), T_{cryo} = 100 K (5.15b) and T_{cryo} = 130 K (5.15c). All scans have been carried out at similar positions, the two bright spots marked with arrows can be identified in all mappings of the PL yield J_γ. At lower temperatures the overall PL yield as well as the size of individual structures increases. Figure 5.16a shows PL spectra from three different positions for T_{cryo} = 85 K. Depending on the lateral position transitions at different photon energies with $P_1 \approx 1.45$ eV, $P_2 \approx 1.511$ eV and $P_3 \approx 1.56$ eV are observed. Töpper et al. [61] measured a PL peak similar to P_1 at 1.44 eV in CuInS_2 and identified it as a donor-acceptor transition (from D_{d1} to D_{a1} in figure

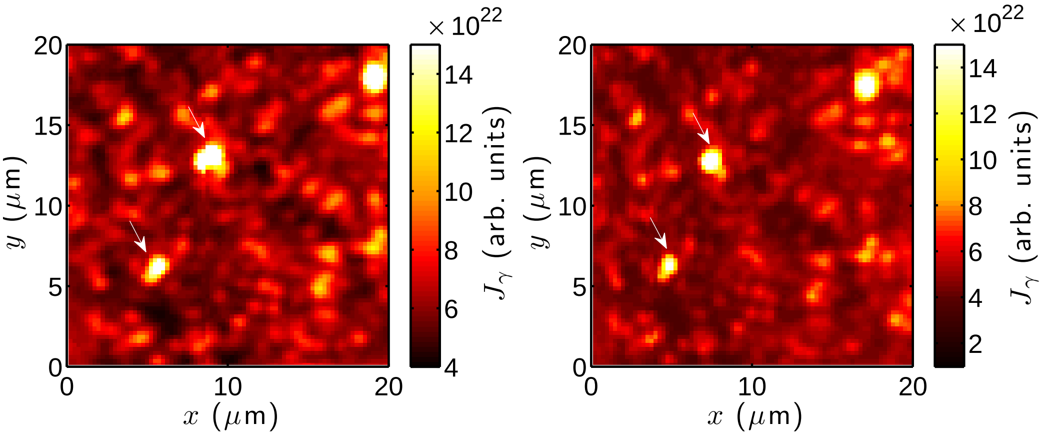
(a) 85 K

(b) 100 K

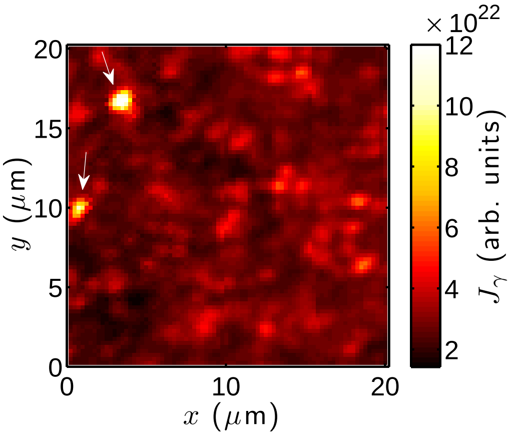
(c) 130 K

Figure 5.15.: Laterally resolved photoluminescence of Cu(In,Ga)S_2 at temperatures of T_{cryo} = 85 K (5.15a), T_{cryo} = 100 K (5.15b) and T_{cryo} = 130 K (5.15c). Details on the experimental setup can be found in chapter 4.1. Luminescence intensities of the scans are comparable.

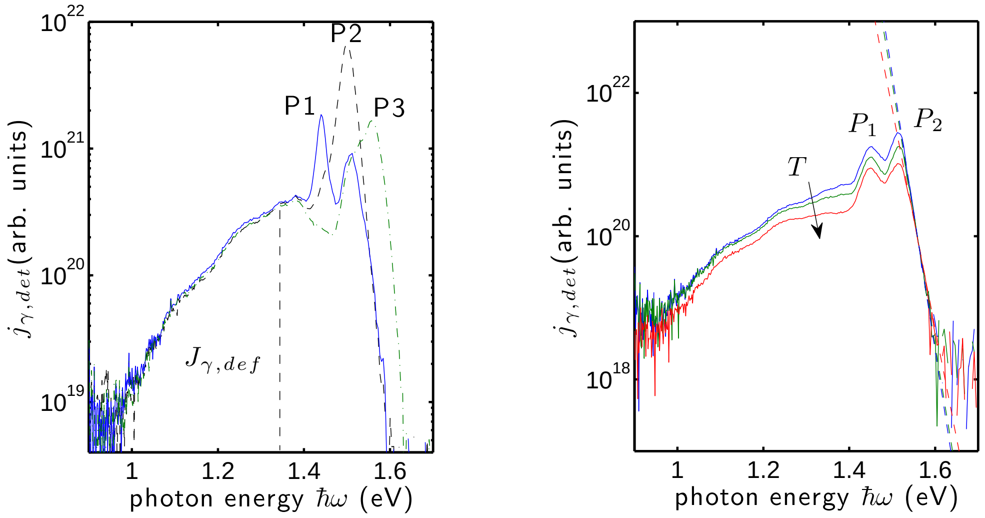

(a) spectra for $T_{cryo} = 85\,\mathrm{K}$

(b) identical positions for increasing T

(c) intensity of P_1

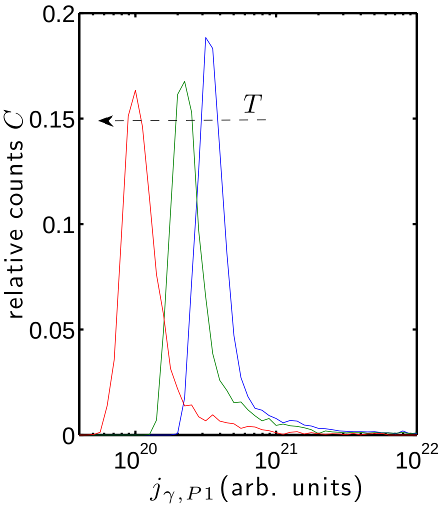

Figure 5.16.: Laterally resolved spectral photoluminescence measured at low temperatures. Figure 5.16a shows exemplary spectra from a scan at $T_{cryo} = 85\,\mathrm{K}$. Three different peaks P_1, P_2 and P_3 occur. 5.16b shows spectra from identical absorber positions for temperatures $T_{cryo} = 85\,\mathrm{K}$, $T_{cryo} = 100\,\mathrm{K}$ and $T_{cryo} = 130\,\mathrm{K}$. 5.16c shows a histogram of the PL yield j_{γ,P_1} of peak P_1 for $T_{cryo} = 85\,\mathrm{K}$, $T_{cryo} = 100\,\mathrm{K}$ and $T_{cryo} = 130\,\mathrm{K}$.

5.13). The energy of a donor-acceptor pair transition is given by [10]

$$\hbar\omega_{DA} = E_g - E_D - E_A + \frac{e^2}{4\pi\epsilon\epsilon_0 r_{DA}} \tag{5.9}$$

where E_D and E_A are donor and acceptor binding energies. The fourth term depends on the distance r_{DA} between donor and acceptor center and represents the Coulomb energy of the ionized centers after recombination. Since phonon interactions can not be observed in polycrystalline Cu(In,Ga)S$_2$ the term $-m\hbar\omega_{LO}$ has been omitted from eq. (5.9). Since the band-gap close to the absorber surface has only a small deviation from that of pure CuInS$_2$ and for 85 K a band-gap shift of about 15 meV to 20 meV can be expected [68, 69], the transition between D_{d1} and D_{a1} is the most likely for P_1 (compare to figure 5.13). The situation is made difficult by the fact, that lateral band-gap fluctuations result in a shift of the donor-acceptor transition, in the present measurements peak P_1 shifts between 1.44 eV and 1.46 eV. For a precise identification of the transition, excitation intensity dependent measurements at identical sample position would have to be carried out. Since the average distance r_{DA} in the Coulomb term in eq. (5.9) decreases for increasing excitation the donor-acceptor transition $\hbar\omega_{DA}$ shifts to higher energies.

The strongest and most often occurring peak is P_2. With an average energy of 1.511 eV it is very close to the average band-gap at room temperature and in average about 61 meV higher than P_1. Furthermore peak P_2 varies between 1.498 eV and 1.525 eV making a clear identification extremely difficult. Most likely is an overlap of so-called free-to-bound and direct "band-to-band" transitions. The energy of free-to-bound transitions involving either donor or acceptor are given by [10]

$$\hbar\omega_{FB} = E_g - E_{D/A} \tag{5.10}$$

so the excitation dependent Coulomb term of eq. (5.9) vanishes since only donors or acceptors are involved. Peak P_3 occurs only in a few local positions and might be due to a "band-to-band" transition in locations with high Ga content.

Figure 5.16b shows an exemplary spectrum for $T_{cryo} = 85\,\mathrm{K}$, $T_{cryo} = 100\,\mathrm{K}$ and $T_{cryo} = 130\,\mathrm{K}$. With increasing temperature T_{cryo} the overall PL yield decreases. Figure 5.16c shows this decrease for the donor-acceptor transition P_1. For a fast relaxation of excited carries (fast compared to recombination) the PL can be described by Planck's generalized law and the high energy wing can be approximates by a Bose term according to eq. (3.12). Since an automated extraction of the variation in quasi-Fermi level splitting proves difficult due to the small and laterally strong fluctuating fitting ranges only a few exemplary spectra will be presented.

The Bose term of figure 5.16b reveals slopes of $kT_{lat} \approx 11\,\mathrm{meV}$ (corresponding to 128 K) for $T_{cryo} = 85\,\mathrm{K}$, $kT_{lat} \approx 12\,\mathrm{meV}$ (corresponding to 143 K) for $T_{cryo} = 100\,\mathrm{K}$ and $kT_{lat} \approx 15\,\mathrm{meV}$ (corresponding to 173 K) for $T_{cryo} = 130\,\mathrm{K}$.

The temperature differences between extracted and cryostat temperature can be due to a band-gap grading with a thick high E_g regime at the back of the absorber or — which is more likely — sample heating which can't be excluded at high excitation and low ambient temperatures. Furthermore extracted slopes $kT_{lat}(x, y)$ vary considerably with the lateral position (not shown here).

The extraction of the local absorbance (not shown here) yields an absorbance $A(\hbar\omega)$ over 20 orders of magnitude, which clearly is beyond the sensitivity of the setup considering a density of states in the range of 10^{20} cm^{-3}. A possible reason for this discrepancy is a strong depopulation of defect levels due to very high quasi-Fermi level splittings (see also section 5.3.2). Thus for a more detailed analysis it has to be known whether the Boltzmann approximation is valid under these conditions.

5.1.4. Structure Analysis

Analogously to chapter 2.2 structure sizes of opto-electronic features can be analyzed by morphological image analyses (see appendix C).

Figures 5.17a and 5.17b show openings of the relative quasi-Fermi level splitting $\triangle_{x,y}E_{Fnp}$ of figures 5.3a and 5.5a. For both absorber layers structure sizes of features in the range of 1 µm–2 µm occur and are smaller than average grain sizes (2 µm–3 µm) found in both sample types. Structure sizes in the optical band-gap of Cu(In,Ga)S$_2$ are found to be between 1 µm and up to 3.5 µm and therefore range from structure size in $\triangle_{x,y}E_{Fnp}$ to grain sizes in surface contour. This seems plausible since the optical threshold E_{opt} is influenced by the absorber thickness in terms of the laterally varying parameter $E'(d(x, y))$. With a diameter of 1 µm the lower boundary of structure sizes in opto-electronic absorber properties is beneath the average grain size and therefore points towards fluctuations within individual grains. With scanning nearfield optical microscopy (SNOM) fluctuating opto-electronic absorber properties within individual grains of Cu(In,Ga)Se$_2$ absorbers have been found [70].

In order to get a minimum scan area needed for a statistically representative PL data set it is proceeded analogously to chapter 2.2. Photoluminescence measurements have been carried out at different positions on an absorber layer and for each position the relative quasi-Fermi level splitting $\triangle_{x,y}E_{Fnp} - \overline{\triangle_{x,y}E_{Fnp}}$ has been calculated. For all $\triangle_{x,y}E_{Fnp} - \overline{\triangle_{x,y}E_{Fnp}}$ data sets openings have been calculated and correlated with each other. To get a correlation coefficient more sensitive to small changes, the

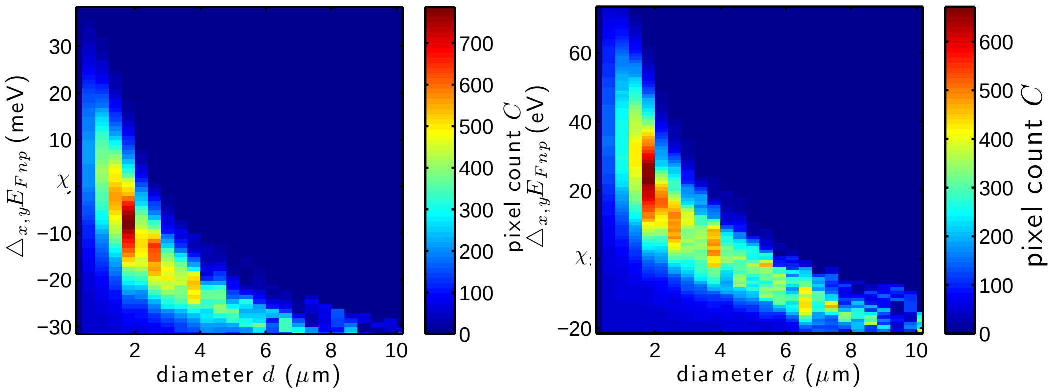

(a) $\triangle_{x,y}E_{Fnp}$ $CuInS_2$ (b) $\triangle_{x,y}E_{Fnp}$ $Cu(In,Ga)S_2$

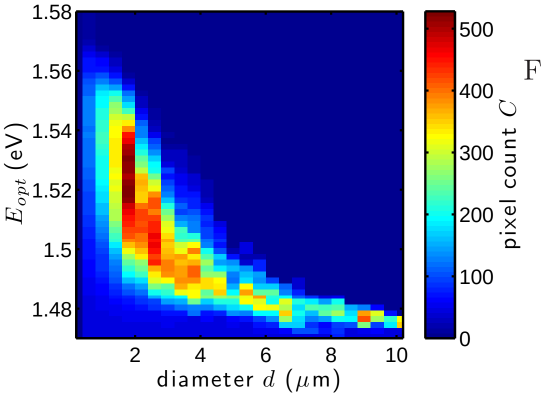

(c) E_{opt} $Cu(In,Ga)S_2$

Figure 5.17.: Opening diagrams of relative quasi-Fermi level splitting $\triangle_{x,y}E_{Fnp}$ of $CuInS_2$ (figure 5.3a) and $Cu(In,Ga)S_2$ (figure 5.5a) and of the optical threshold mapping E_{opt} of $Cu(In,Ga)S_2$ (figure 5.9b).

weighted correlation r_w has been calculated according to eq. (2.3). After artificially reducing scan areas, opening operations have been recalculated and re-correlated. The result is shown in figure 5.18. For large scan areas (above 2000 µm^2) the correlation coefficients saturate against a value of $r_w \approx 0.9$. For smaller scan areas r_w decreases or rather different r_w diverge depending on the underlying data set. Below a threshold of $s_t \approx 841\,\mu m^2 = 29\,\mu m \times 29\,\mu m$ correlation coefficients r_w decrease or diverge considerably, thus the statistical representativity of the underlying dataset is no longer given.

5.1.5. Towards Solar Cell Operating Conditions

Since high excitation fluxes in the range of 10^4 suns equivalent fluxes are needed for detectable photoluminescence yields in laterally resolved measurements with a reso-

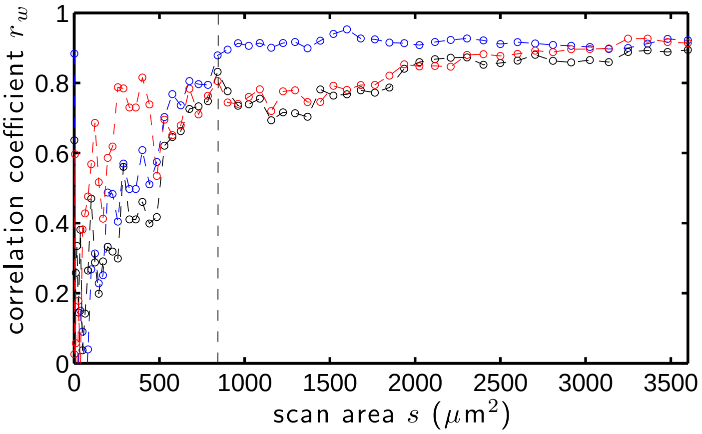

Figure 5.18.: Statistical representativity of extracted $\triangle_{x,y}E_{Fnp}$ data sets. The correlation coefficient r_w of openings calculated from three different $\triangle_{x,y}E_{Fnp}$ mappings with varying scan area s has been calculated according to eq. (2.3).

lution of less than 1 µm, the question arises whether the sample properties extracted above can be applied to solar cell absorber layers operated under AM1.5 equivalent conditions. In order to extrapolate the experimental results towards AM1.5 equivalent conditions, measurements with varying excitation levels have been carried out at room temperature.

To study the behavior of lateral fluctuations, the fluctuations of quasi-Fermi level splitting $\triangle_{x,y}E_{Fnp}$ have been extracted from PL scans over 20 µm × 20 µm ((100 × 100) spectra) with varying excitation ϕ carried out on $CuInS_2$ and $Cu(In,Ga)S_2$ samples. Sample heating by very high excitation fluxes (as seen in fig. 5.21) has been avoided. Figure 5.19a shows the histograms of $\triangle_{x,y}E_{Fnp}$ for $CuInS_2$ measured in a range of ϕ_0 to $10 \cdot \phi_0$ with $\phi_0 = 1.1 \times 10^4$ AM1.5 equivalent flux. Aside from an increase in quasi-Fermi level splitting no changes in the extent of variations can be observed. The fluctuations $\triangle_{x,y}E_{Fnp} - \overline{\triangle_{x,y}E_{Fnp}}$ (figure 5.19b) for all excitations are $\text{FWHM}_{CIS} \approx 42\,\text{meV} \approx$ *const.*. A similar result is found for $Cu(In,Ga)S_2$, which has been measured for excitation fluxes between ϕ_0 and $80 \cdot \phi_0$ with $\phi_0 = 3.8 \times 10^2$ AM1.5 equivalent flux. The variations in $\triangle_{x,y}E_{Fnp}$ have a con-

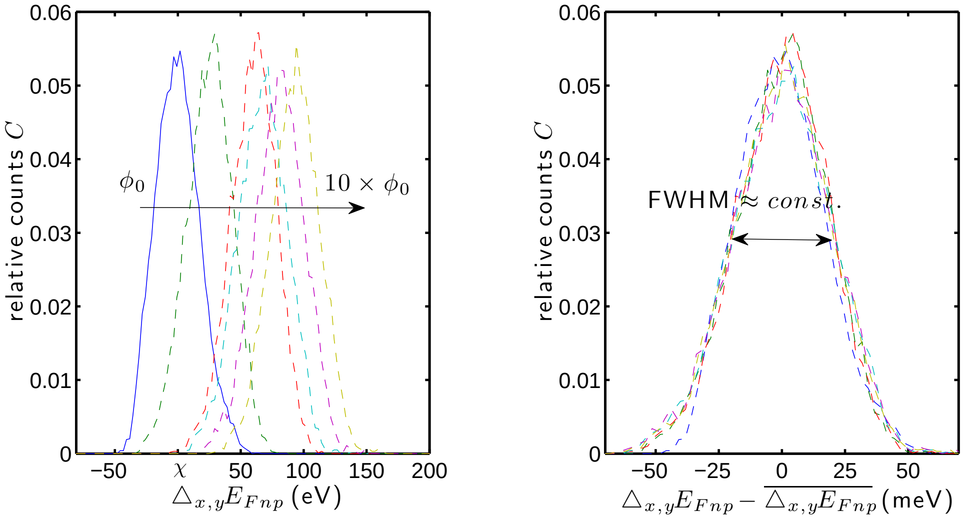
(a) Histogram of $\triangle_{x,y}E_{Fnp}$ of CIS

(b)

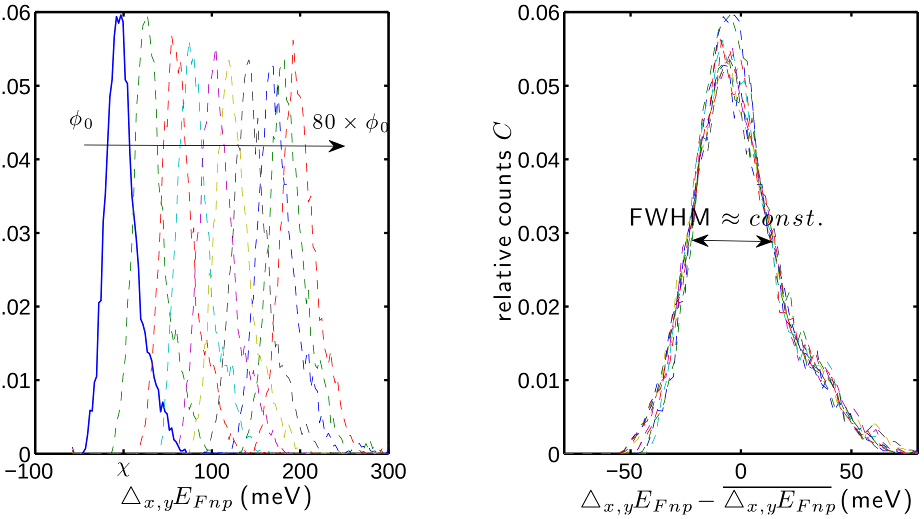
(c) Histogram of $\triangle_{x,y}E_{Fnp}$ of CIGS

(d)

Figure 5.19.: Histograms of quasi-Fermi level splitting of CIS and CIGS for different excitations ϕ in the range of ϕ_0 to $10 \cdot \phi_0$ (with $\phi_0 = 1.1 \times 10^4$ AM1.5 equivalent ($CuInS_2$) and ϕ_0 to $80 \cdot \phi_0$ (with $\phi_0 = 3.8 \times 10^2$ AM1.5 equivalent)($Cu(In,Ga)S_2$). The scan area amounts to $20\,\mu m \times 20\,\mu m$ (1×10^4 spectra).

stant full width at half maximum of $\text{FWHM}_{CIGS} \approx 38\,\text{meV} \approx const.$[3]. This is in contrast to the decrease of variations $\triangle_{x,y}E_{Fnp}$ with increasing excitation found on Cu(In,Ga)Se$_2$ samples [20].

For small excitation fluxes ϕ and a 3-level system of valence band, conduction band and a defect level (e.g. level D_1), the generation G and recombination R of carriers in an absorber layer can be described by the Shockley-Read-Hall (SRH) model [71,72]. In the case of low excitation, the non-radiative recombination dominates and carrier lifetimes are approximately independent of the optical generation leading to a linear dependence between generation G and radiative recombination R_{rad} (see figure 5.20a and 5.20b). For very high generation G the non-radiative recombination saturates $R_{nr} \to const.$, leading again to an almost linear dependence between generation and radiative recombination [4] $G \propto R_{rad}$. In between these two ranges the dependence is non-linear, in a double logarithmic plot this can be seen in a slope departing from unity (figure 5.20). So the photoluminescence dependence of ϕ can be described by [19]

$$j_{\gamma,det} \propto \phi^{\beta}, \tag{5.11}$$

with exponent β.

Figure 5.20c shows the maximum $\overline{j_{det,max}}$ of the PL yield averaged over the area of a laterally resolved scan for different excitation fluxes (data set of figure 5.19a and 5.19c). Since different detectors have been used for CuInS$_2$ (red) and Cu(In,Ga)S$_2$ (blue) photon fluxes are not directly comparable. In both cases a similar exponent $\beta > 1$ is found, $\beta_{CIS} = 1.72 \pm 0.08$ and $\beta_{CIGS} = 1.78 \pm 0.15$. Therefore measurements are carried out at generation rates between the linear regime of small excitation and the linear regime of high excitation and saturated non-radiative recombination. According to Planck's generalized law is $j_{\gamma,det} \propto \exp\left({(E_{Fn} - E_{Fp})}/{kT}\right)$, so

$$E_{Fn} - E_{Fp} \propto kT \ln j_{\gamma,det} \propto kT\beta \ln \phi. \tag{5.12}$$

Figure 5.20d shows the average quasi-Fermi level splitting $\overline{\triangle_{x,y}(E_{Fn} - E_{Fp})}$ of figs. 5.19a and 5.19c. The extracted slopes are 43 meV (CuInS$_2$) and 47 meV (Cu(In,Ga)S$_2$)

---

[3] The discrepancy to the full width at half maximum for Cu(In,Ga)S$_2$ shown in figure 5.5 can be explained by difference in scan area. Due to limitations in scanning time for low excitation fluxes the scan area had to be reduced below the level of statistical representativity. Nevertheless a change in variations of quasi-Fermi level splitting would be seen in the histogram of figure 5.19.

[4] In a doped semiconductor with low excitation the majority carrier concentration is much larger than the excess concentration of the minority carriers, thus $G(\phi) = R_{rad}(\phi) + R_{nr}(\phi)$ with $R_{rad} = j_{\gamma,det} \propto p_0\Delta n$. With increasing excitation $\Delta n \gg p_0$ and $R_{rad} = j_{\gamma,det} \propto \Delta n^2$. Since the non-radiative recombination saturates for very high excitation fluxes, one can write $G(\phi) = R_{rad}(\phi) + R_{nr}$.

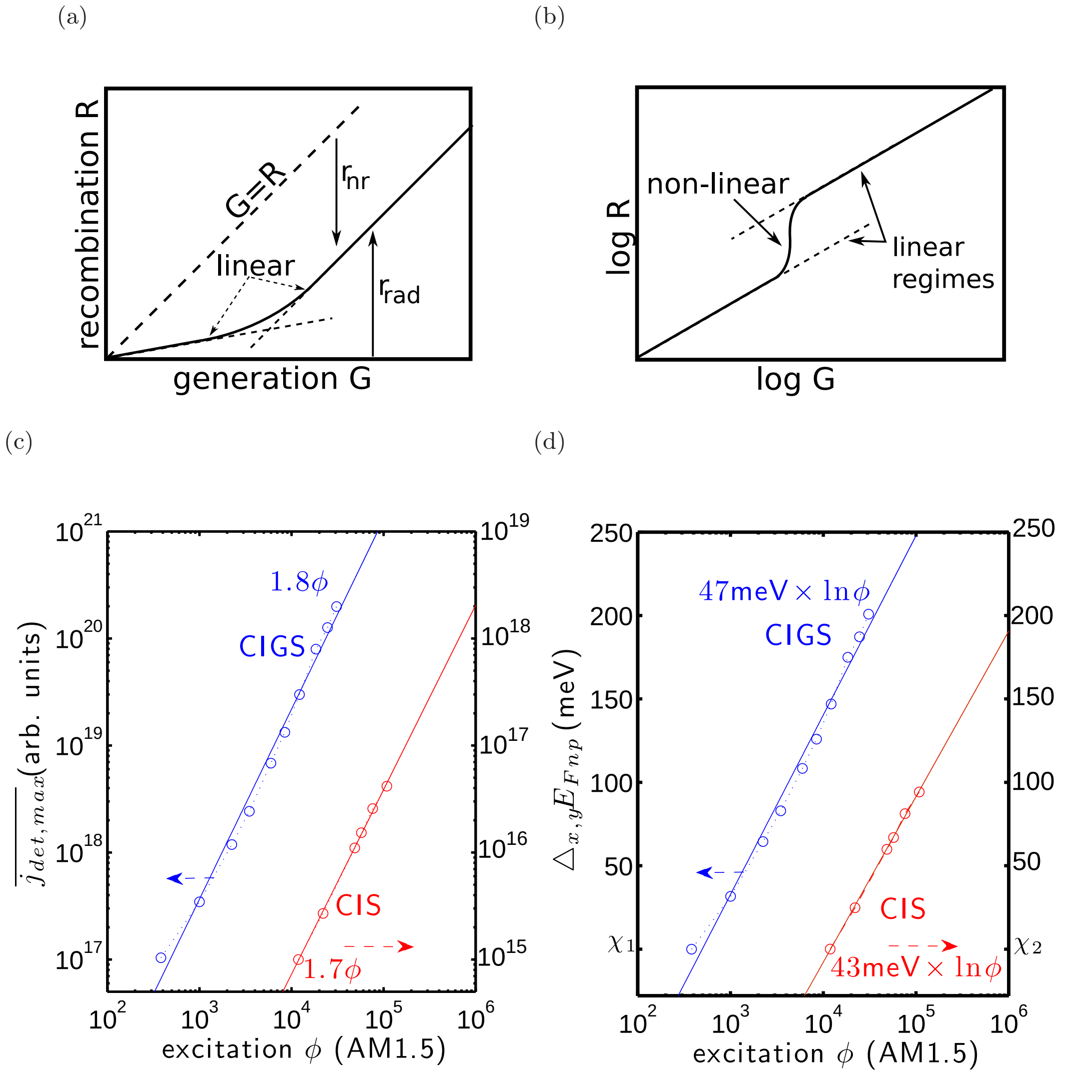

Figure 5.20.: Sketch of the dependence of radiative recombination R on generation G in linear (5.20a) and double logarithmic (5.20b) scale. Figure 5.20c shows the average PL maximum $\overline{j_{\gamma,max}}$ and 5.20d the average quasi-Fermi level splitting $\overline{\triangle_{x,y}E_{Fnp}}$ depending on the excitation flux ϕ in AM1.5 equivalents.

which corresponds to exponents of $\beta_{CIS} \approx 1.66$ and $\beta_{CIGS} \approx 1.81$ for an average temperature of $T \approx 300\,\mathrm{K}$. Thus for laterally resolved PL both determinations of β are equivalent.

Provided the exponent β is in the range $1 - 1.8$ for $\phi < 3.8 \times 10^2$ AM1.5 equivalent a rough extrapolation towards AM1.5 conditions can be made, although the correct β for lower excitation fluxes may actually be smaller (see figure 5.20a). Thus quasi-Fermi level splittings extracted in laterally resolved PL at $3.8{\times}10^2$ AM1.5 are between 155 meV to 280 meV higher than those under AM1.5 conditions.

Figure 5.21a shows the spectrum of a $CuInS_2$ sample measured in the range of 1.6×10^3 AM1.5 equivalent to 2.5×10^6 AM1.5 equivalent (which is well beyond normal excitation conditions even in microscopic measurements) at identical positions. Besides higher PL yield spectral variations are clearly visible. For higher excitation fluxes the ratio between high and low energy peak changes. The approximation by a Bose term shows an increase in E_{Fnp} by about 155 meV and in T_{lat} by about 40 K. In figure 5.21b four absorbance spectra extracted from the PL in figure 5.21a are shown, with increasing excitation ϕ the absorbance in the low energy regime decrease. For a

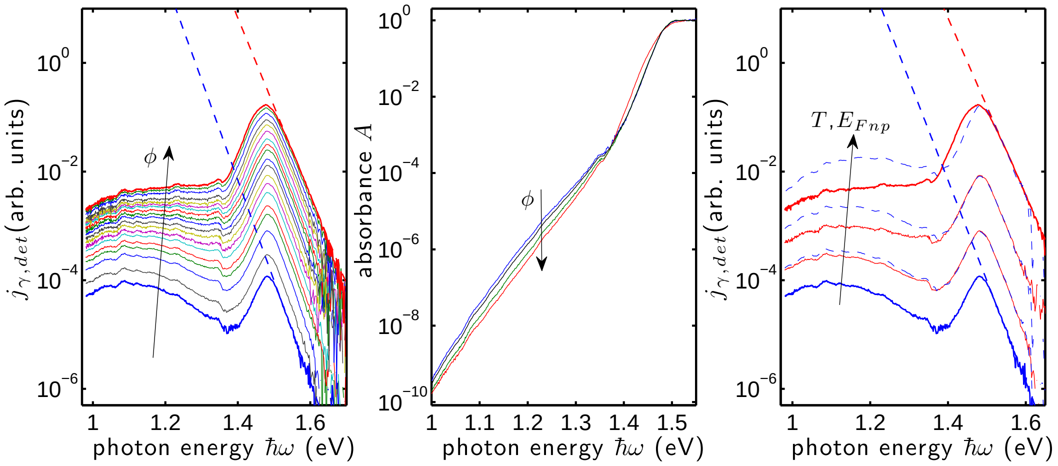
(a) Varying ϕ, measured

(b) Varying ϕ

(c) Varying T and E_{Fnp}, modelled

Figure 5.21.: $CuInS_2$ spectra measured at an identical position for excitations in the range of 1.6×10^3 AM1.5 equivalent to 2.5×10^6 AM1.5 equivalent. Figures 5.21b and 5.21c show extracted absorbance A and reconstructed PL spectra varying temperature T and quasi-Fermi level splitting $E_{Fn} - E_{Fp}$. For details see text.

better visualization the PL spectra measured with high excitation are reconstructed with the absorbance spectrum extracted from the PL with lowest excitation ϕ (blue in figure 5.21c). It is clearly visible that the PL and the absorbance in the low energy range decreases with higher excitation due to a "bleaching" effect. However the absorbance analyses of deep defects in the previous section are not affected by this, since $\phi \approx const.$ throughout a scan the bleaching effect is laterally constant. This is confirmed by the fact that laterally resolved measurements at lower excitation fluxes have shown the same anti-correlation between A_{def} and $\triangle_{x,y}E_{Fnp}$. Furthermore a redefinition of A_{def} by shifting the lower integration boundary (eq. (5.4)) to higher energies, that is the less "bleached" spectral region, has no effect on the measured anti-correlation between A_{def} and $\triangle_{x,y}E_{Fnp}$. The transition towards macroscopic measurements at AM1.5 equivalent conditions is made in section 5.3.

5.2. Cu(In,Ga)S$_2$ without Molybdenum Back Contact

Since absorber layers without Mo back contact — here referred to as "transparent" Cu(In,Ga)S$_2$ — have a different growth behavior they have been analyzed here separately. The first part of this section describes the PL emitted of such samples through front and rear surface. In the second part micro transmission measurements — that is the transmission of "white light" on the microscopic scale — is studied.

5.2.1. Photoluminescence of Front- and Backside

Laterally resolved PL measurements on "transparent" Cu(In,Ga)S$_2$ samples have been carried out in the setup described in section 4.1 and already used in 5.1. Photoluminescence of the rear surface is measured by excitation from the front through the CdS layer and detection of the emitted luminescence through the substrate on the rear side. Due to the substrate, a microscope objective with larger working distance (W.D. = 6.9 mm, numerical aperture NA = 0.5) and in turn smaller resolution (50×) had to be used. In order to get sufficient PL photon fluxes the excitation amounts to 2.5×10^5 AM1.5 equivalent fluxes and thus sample heating can't be avoided. Photoluminescence emitted through the front surface has been measured at identical positions, with the same excitation, but larger resolution (60×) and smaller working distance (W.D. = 0.3 mm, numerical aperture NA = 0.8).

A mapping of both PL yields (front and rear) of a Cu(In,Ga)S$_2$ absorber without Mo back contact is shown in figures 5.22a and 5.22b. The scale of PL intensity is not directly comparable due to different optical paths and microscope objectives. In both

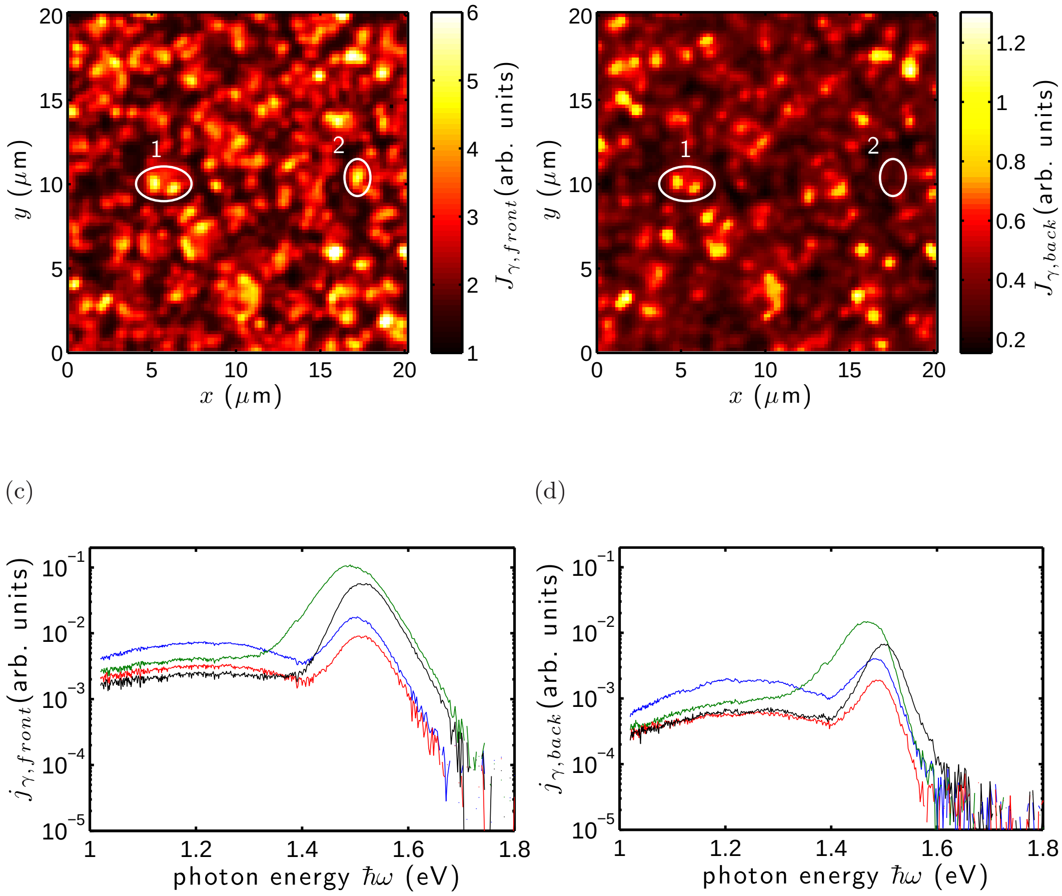
(a) $J_{\gamma,front}$ mapping

(b) $J_{\gamma,back}$ mapping

(c)

(d)

Figure 5.22.: Photoluminescence of a transparent Cu(In,Ga)S_2 sample, excitation from the frontside, PL measurement from the front and from the backside.

mappings similar structures occur. Individual structures can be identified in both, on front and back mapping (e.g. point 1 in 5.22a and 5.22b). With a correlation coefficient of $r_{f,b} \approx 0.68$ with $r \in [-1;1]$, it can be assumed that most grains extend throughout the absorber material while having a higher Ga content a the back. On the other hand some structures appearing on the front are not visible on the PL mapping of the rear side (e.g. point 2 in 5.22a and 5.22b), such grains might not extend over the full absorber layer thickness.

Figure 5.22c and 5.22d show exemplary spectra for identical positions. In all spectra no luminescence from the high band-gap regime at the rear side of the absorber is visible. The spectral shape between both varies significantly especially in the slope of the high energy wing. In the PL spectra detected from the rear side the slope of the high energy wing is much steeper. The steeper slope points towards a smaller quasi-Fermi level splitting in the high band-gap regime close to the glass substrate (compare to figure 3.6c). A constant E_{Fnp} throughout the absorber or a higher E_{Fnp} in the high band-gap regimes would not lead to a slope $< -1/kT$ (compare to figure 3.6). Such a gradient in $E_{Fnp}(z)$ could be caused by the different growth process of absorber layers without Mo back contact, e.g. a high defect density or a high surface recombination velocity close to the substrate.

5.2.2. Micro Transmission

Laterally and spectrally resolved transmission measurements on the microscopic scale have been carried out at identical positions with PL and AFM measurements. For transmission of “white light” a halogen lamp has been coupled into the setup described in section 4.1 in addition to the excitation laser. The given transmission spectra are measured with respect to transmission through the sample substrate $T = T_{sample}/T_{substrate}$. Due to technical reasons the transmission measurements have a lower optical resolution with a spot size of 8 µm ± 1 µm in diameter.

Figure 5.23a and 5.23c show surface contour h and transmission $T_{ges}(x,y) = \int T(x,y,\hbar\omega)\mathrm{d}\hbar\omega$ of a Cu(In,Ga)S_2 sample grown without Mo back contact, to guarantee identical sample positions the sample has been marked in the upper left corner. Since resolution in AFM measurements is much higher the surface contour h has been convolved with a two dimensional gaussian ($\sigma = 3\,\mu\mathrm{m}$) in order to compare T_{ges} and h, the result h' is shown in figure 5.23b. Between h' and T_{ges} a slight anti-correlation of $r(T_{ges}, h') \approx -0.41$ is found[5]. At some positions this anti-correlation is more pronounced, while others seem to have a direct correlation or no correlation at all, e.g. structures 1 and 2 in mappings 5.23b and 5.23c are anti-correlated (high thickness, low transmission) whereas at position 3 a low thickness as well as a low transmission is found. This could be an indication for a laterally varying reflection or dispersion, since T_{ges} is mainly governed by the transmission in the low energy range where the absorbance $A < 10^{-4}$ is too small to be measureable with direct transmission measurements.

---

[5] Only the non-marked area has been used for calculation of the correlation coefficient, the correlation between T_{ges} and h (original surface contour data set) is $r(T_{ges}, h) \approx -0.23$.

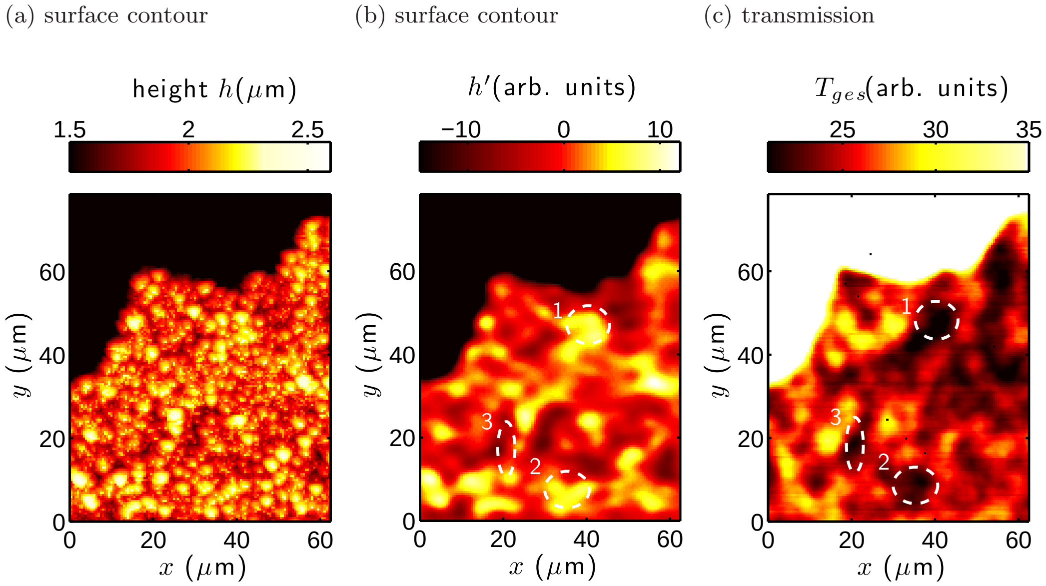

Figure 5.23.: Surface contour h (5.23a) and transmission T (5.23b) of a Cu(In,Ga)S_2 sample grown without Mo back contact. The absorber has been marked in the upper left corner to guarantee identical sample positions.

In the following photoluminescence and transmission at identical absorber positions will be analyzed (figure 5.24a and 5.24b)[6]. As in figure 5.23c the mapping of T_{ges} shows larger structures than the corresponding PL mapping J_γ, which is due to the difference in optical resolution. T_{ges} shows fluctuations up to a factor of 2. Figure 5.24c displays exemplary transmission spectra $T(\hbar\omega)$ for the positions marked in 5.24a and 5.24b. In contrast to macroscopic transmission measurements (figure 2.7) an in average smaller T in the low photon energy (large wavelength) regime is measured. On the basis of macroscopic measurements have been carried out with an integrating sphere the difference might be explained by dispersion on the microscopic scale (spot size is larger than average grain size) which also corresponds to figure 5.23. To analyze a possible influence of laterally varying opto-electronic absorber properties, the variation in quasi-Fermi level splitting as well as the local absorbance (figure 5.24e) have been calculated. However neither a correlation be-

---

[6] Marking the sample is not necessary, since PL and transmission have identical optical excitation paths and the experimental setup does not have to be altered.

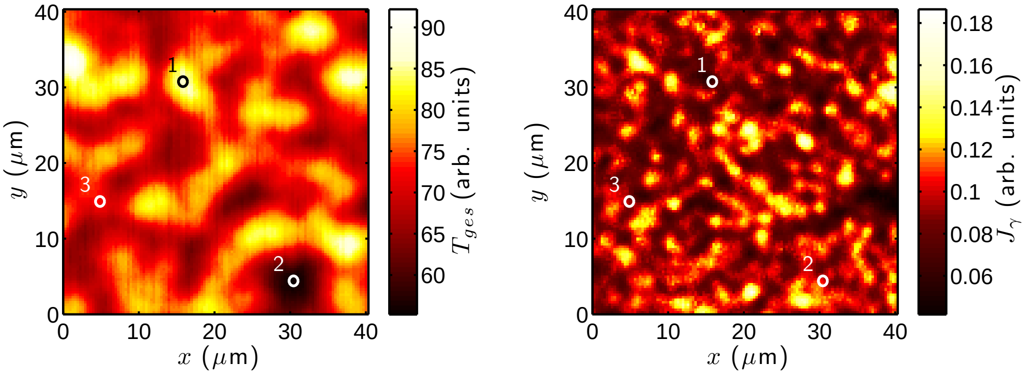
(a) transmission T_{ges}

(b) J_γ mapping

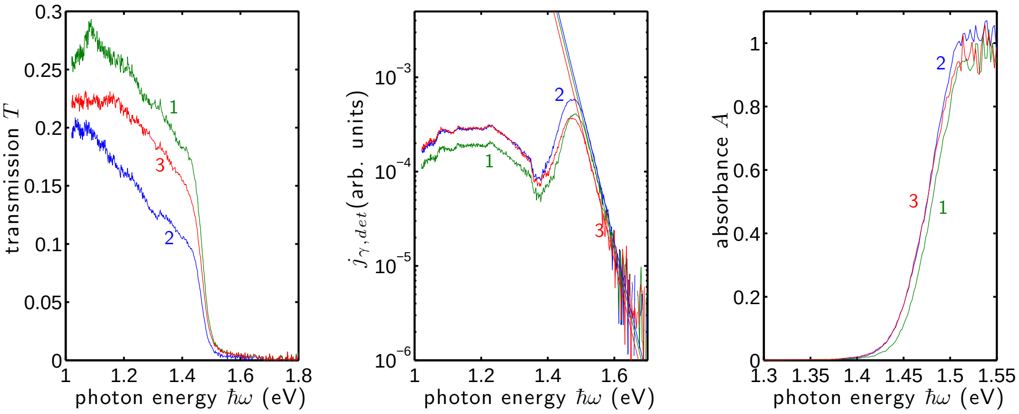
(c) transmission spectra

(d) PL spectra

(e) absorbance spectra

Figure 5.24.: Transmission and laterally resolved PL on a Cu(In,Ga)S_2 sample withou Mo back contact, 5.24a shows a mapping of the transmission $T_{ges}(x,y) = \int T(x,y,\hbar\omega)\mathrm{d}\hbar\omega$ and 5.24b a mapping of the PL yield J_γ. In figure 5.24c, 5.24d and 5.24e exemplary transmission, PL and absorbance spectra are shown. Numbers correspond to the positions marked in 5.24a and 5.24b.

tween local quasi-Fermi level splitting (not shown here) and local transmission nor a relation between optical band-gap and transmission or the onset of optical transmission $T_{opt} := \hbar\omega(T = 0.05)$ is found. Thus small scale transmission is mainly governed by varying reflection and/or dispersion in the low photon energy regime. Eventually an increase in optical resolution for “white light” transmission could improve this analysis.

5.3. Transition to Macroscopic Calibrated Analyses

For the transition/alignment to macroscopic measurements spectral variations due to nonlinear superposition of individual PL centers as described in chapter 3.1.1 have to be taken into account. The variations in quasi-Fermi level splitting $\triangle_{x,y}E_{Fnp}$ on the microscopic scale lead to an overestimation of the quasi-Fermi level splitting $E_{Fnp,macro}$ extracted from a macroscopic PL measurement.

If lateral diffusion of charge carriers in measurements with macroscopic scale illumination can be neglected or has the same extend as in laterally resolved measurements on the microscopic scale, the overestimation for gaussian shaped variations is $\sigma^2_{E_{Fnp}}/(2kT)$ with standard deviation $\sigma_{E_{Fnp}}$ extracted in laterally resolved microscopic PL scans. A homogeneous illumination as it is used on the macroscopic scale could lead to a different lateral diffusion and thus to an alteration in σ_μ which in turn leads to a change in the overestimation. In addition fluctuations below the optical resolution of the experimental setup to measure PL with sub micron resolution would lead to a further overestimation. Since all these unknown parameters can’t be taken into account, corrections to macroscopic extracted quasi-Fermi level splittings $E_{Fnp,macro}$ are made according to $\sigma_{E_{Fnp}}/(2kT)$ (eq. (3.17)). Furthermore microscopic band-gap fluctuations lead to a softening of the macroscopic absorption edge, consequently the point where $A(\hbar\omega) \approx 1$ shifts to higher energies which is important for quasi-Fermi level splitting extraction. The spectra shown at the beginning of the chapter point out another discrepancy, the ratio between high energy and low energy peak changes considerably. The same effect was addressed in the last section for measurements with varying excitation ϕ.

The excitation flux needed to get detectable photoluminescence yields differs between measurements on microscopic and macroscopic scale by a factor of about 10^3 to 10^4. Very high excitation fluxes on the other hand, could lead to a high quasi-Fermi level splitting and a depopulation of defect states which would lead to a decrease in the absorption coefficient in this energy range (see section 5.3.2). Also a lateral variation of the defect level D_1 on the microscopic scale (see section 5.1.2) can lead to an increase in defect luminescence $J_{\gamma,def}$ and to a shift in the maximum of defect luminescence in macroscopic PL measurements. But since microscopic fluctuations in the in the defect level D_1 are comparably small this effect can be neglected (for a detailed description see appendix D).

5.3.1. Quasi-Fermi Level Splitting

Figure 5.25 shows the absolute photon flux emitted by a $CuInS_2$ absorber layer (same sample as in section 5.1.1) for excitation fluxes of ϕ = 1 AM1.5, 10 AM1.5 and 25 AM1.5 equivalents. All spectra have been measured with the setup described in chapter 4.2 with an optical resolution of approximately 1 mm^2. Depending on the wavelength region InGaAs-detector, silicon photodiode or photomultiplier have been used. To minimize heating, the sample has been mounted on a copper block. The low energy wing of the spectrum at AM1.5 is below the detection threshold of the InGaAs detector. Due to negligible band-gap fluctuations $\triangle_{x,y}E_g$ (see figure 5.9) a sharp maximum of the "band-to-band" peak can be measured (see chapter 3.1.1). The quasi-Fermi level splitting $E_{Fnp,macro}$ extracted from the high energy

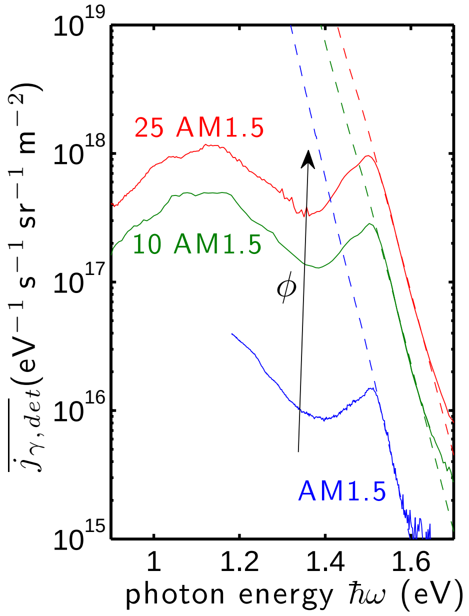

Figure 5.25: Calibrated Photoluminescence of $CuInS_2$ for excitation ϕ of 1, 10 and 25 sun equivalent fluxes at λ = 532 nm. The detection area is 1 mm^2. (sample from the same batch as $CuInS_2$ in table 2.1)

wing according to eq. (3.11) with $A = (1 - R_F)$ yields[7]

$$\begin{aligned}(E_{Fn} - E_{Fp})_{macro,\mathrm{AM1.5}} &= 825\,\mathrm{meV} \pm 79\,\mathrm{meV}\\ \text{with } T_{lat,\mathrm{AM1.5}} &= 328\,\mathrm{K} \pm 11\,\mathrm{K}\\ (E_{Fn} - E_{Fp})_{macro,\mathrm{10AM1.5}} &= 829\,\mathrm{meV} \pm 52\,\mathrm{meV}\\ \text{with } T_{lat,\mathrm{10AM1.5}} &= 369.7\,\mathrm{K} \pm 8.0\,\mathrm{K}\\ (E_{Fn} - E_{Fp})_{macro,\mathrm{25AM1.5}} &= 848\,\mathrm{meV} \pm 43\,\mathrm{meV}\\ \text{with } T_{lat,\mathrm{25AM1.5}} &= 380.8\,\mathrm{K} \pm 6.8\,\mathrm{K}.\end{aligned}$$

Thus already at an illumination of one sun equivalent fluxes, sample heating for “large” area excitation (e.g. mm^2) can’t be avoided. The large error in $E_{Fnp,macro}^{\mathrm{AM1.5}}$ is due to the relatively small fitting range and the resulting slope variations. At higher excitation the error decreases slightly at the expense of more sample heating. The reflection R_F has only a small influence on the extracted $E_{Fnp,macro}$, neglecting R_F leads to a decreased $E_{Fnp,macro}$ by about 5 meV. With fluctuations on the microscopic scale of $FWHM = 48\,\mathrm{meV} \pm 5\,\mathrm{meV}$ or $\sigma_{E_{Fnp}} \approx 19.8\,\mathrm{meV}$, respectively, the overestimation due to non-linear averaging amounts to

$$\begin{aligned}\frac{1}{T_{lat,\mathrm{AM1.5}}}\frac{\sigma^2_{E_{Fnp}}}{2k} &= 6.9\,\mathrm{meV} \pm 0.4\,\mathrm{meV}\\ \frac{1}{T_{lat,\mathrm{10AM1.5}}}\frac{\sigma^2_{E_{Fnp}}}{2k} &= 6.2\,\mathrm{meV} \pm 0.2\,\mathrm{meV}\\ \frac{1}{T_{lat,\mathrm{25AM1.5}}}\frac{\sigma^2_{E_{Fnp}}}{2k} &= 6.0\,\mathrm{meV} \pm 0.2\,\mathrm{meV} \qquad (5.13)\end{aligned}$$

and is much smaller than the error resulting from the fit. Nevertheless, the correction $E_{Fnp} = E_{Fnp,macro} - \sigma^2_{E_{Fnp}}/2kT$ leads to $E_{Fnp,AM1.5} = 818\,\mathrm{meV} \pm 95\,\mathrm{meV}$, $E_{Fnp,10AM1.5} = 823\,\mathrm{meV} \pm 25\,\mathrm{meV}$ and $E_{Fnp,25AM1.5} = 842\,\mathrm{meV} \pm 25\,\mathrm{meV}$.

For the Cu(In,Ga)S$_2$ sample a higher fluctuation in opto-electronic absorber properties on the microscopic scale, as well as the band-gap grading in comparison with CuInS$_2$ have to be taken into account. According to section 3.1.1 and figure D.2 the fluctuations $\triangle_{x,y}E_g$ lead to a smearing out of the absorbance edge, resulting in a shift and a broadening of the high energy peak. This corresponds to the PL spectra shown in figure 5.26a with $\triangle_{x,y}E_g \approx 70\,\mathrm{meV}$ (from section 5.1.1) the point where

---

[7] For R_F the reflection measurement of figure 2.7 is used, since $R = R_F$ for sufficient high energies above the band-gap.

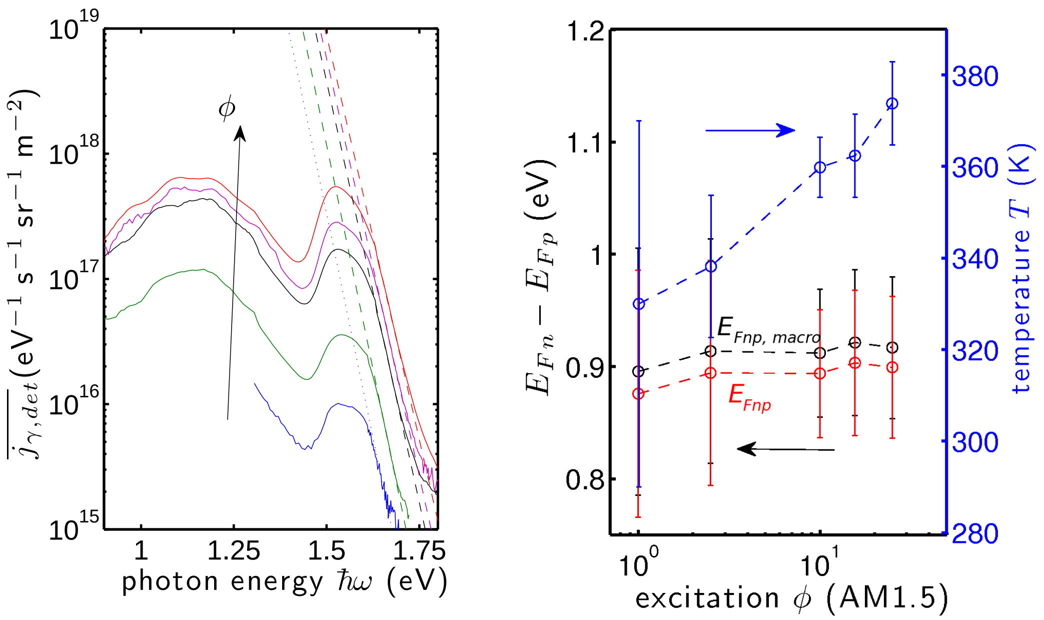

(a) Cu(In,Ga)S_2

(b)

Figure 5.26.: Calibrated photoluminescence of a Cu(In,Ga)S_2 absorber layer, 5.26a shows spectra measured at the same sample position with an excitation of $\phi = (1; 2.5; 10; 15.6$ and $25)$ AM1.5. 5.26b shows quasi-Fermi level splitting $E_{Fnp,macro}$ and temperature T_{lat}, which have been extracted according to eq. (3.11) with $A = (1 - R_F)$. (sample from the same batch as Cu(In,Ga)S_2 b in table 2.1)

$A > 0.97$ shifts by about[8] 20 meV. The detected PL is emitted from the low band-gap regime close to the surface of the absorber layer, the PL of the high band-gap region is — due to reabsorption — below the detection threshold. To extract the absolute quasi-Fermi level splitting $E_{Fnp,macro}$, it is proceeded analogously to the CuInS_2 sample and the factor $(1 - R_F)$ is taken into account. Figure 5.26b shows extracted $E_{Fnp,macro}$ and T_{lat}. Due to the large fluctuations in E_g the fitting range compared to CuInS_2 decreases, causing a further increase in errors. For one sun equivalent a

---

[8] This is a rough estimate since the fluctuations $\triangle_{x,y}E_g$ are not very well described by a gaussian distribution with $\sigma_{E_g} \approx 30$ meV and the actual absorption coefficient differs from that of an ideal direct semiconductor.

quasi-Fermi level splitting of $E_{Fnp,macro} = 895\,\text{meV} \pm 110\,\text{meV}$ is found. For increased excitation only a slightly higher $E_{Fnp,macro}$ is measured due to the increase in sample temperature. With fluctuations in the microscopic scale quasi-Fermi level splitting $\triangle_{x,y}E_{Fnp}$ of $\text{FWHM}_{\triangle_{x,y}E_{Fnp}} = 79\,\text{meV} \pm 5\,\text{meV}$ or $\sigma_{E_{Fnp}} = 33.6\,\text{meV}$, the overestimation by incorrect averaging ranges between 19.9 meV and 17.5 meV depending on the actual sample temperature. Corrected $E_{Fnp,macro}$ are shown in figure 5.26b.

Since cell areas of finally processed solar cells with similar absorber layers amount to $0.5\,\text{cm}^2$, the measured area of $1\,\text{mm}^2$ is not representative due to variations on the macroscopic scale. To quantify variations on the scale of the cell area spectrally resolved PL mappings of the absorber layer have been measured with a resolution of $1\,\text{mm}^2$ (figure 5.27a) in the experimental setup described in section 4.3. The dashed lines indicate the sample dimensions. Spectra for the marked positions are shown in figure 5.27c and reveal strong spectral fluctuations on the macroscopic scale, especially of the high energy wing. For an average slope 28.4 meV (corresponding to a temperature of $T = 330\,\text{K}$ extracted from the PL spectra) the variation in quasi-Fermi level splitting $\triangle_{x,y}E_{Fnp,macro}$ has been extracted. The result with positions marking the spectra of figure 5.27c, is shown in figure 5.27b. Fluctuations of up to 100 meV are observed[9]. Mappings 5.27a and 5.27b demonstrate nicely that a higher PL yield is not necessarily an indicator for a high quasi-Fermi level splitting. The histogram of the $\triangle_{x,y}E_{Fnp,macro}$ mapping shows fluctuations with $\text{FWHM} = 65\,\text{meV} \pm 15\,\text{meV}$ which is in the same range as small scale fluctuations with 79 meV. The calibrated PL shown in figure 5.26 has been measured in the upper right corner of the PL scan of figure 5.27a and 5.27b (near position 3)[10]. Solar cells with nominal identical absorber layers (from the same batch) have an open circuit voltage $V_{oc} \approx 794\,\text{mV}$ and an efficiency $\eta \approx 11\,\%$ and are thus within the range of error and lateral variations on the macroscopic scale of the extracted quasi-Fermi level splitting $\overline{(E_{Fn} - E_{Fp})}_{AM1.5} = 875\,\text{meV} \pm 110\,\text{meV}$.

With the analyses of the same absorber layer in calibrated PL at low excitation and PL with sub-micron resolution under high excitation the rough extrapolation made in section 5.1.5 can be connected to the absolute E_{Fnp} extracted above. Figure 5.28 shows the maximum of the macroscopic PL yield $\overline{j_{\gamma,max}}$ ("band-to-band" luminescence) of figure 5.26 together with the data from microscopic laterally resolved

---

[9] The black spots correspond to positions where no extraction of $\triangle_{x,y}E_{Fnp,macro}$ was possible due to low PL yields.

[10] The exact location is not known since the sample had to be mounted in different experimental setups and marking the sample goes along with destroying a part of the film.

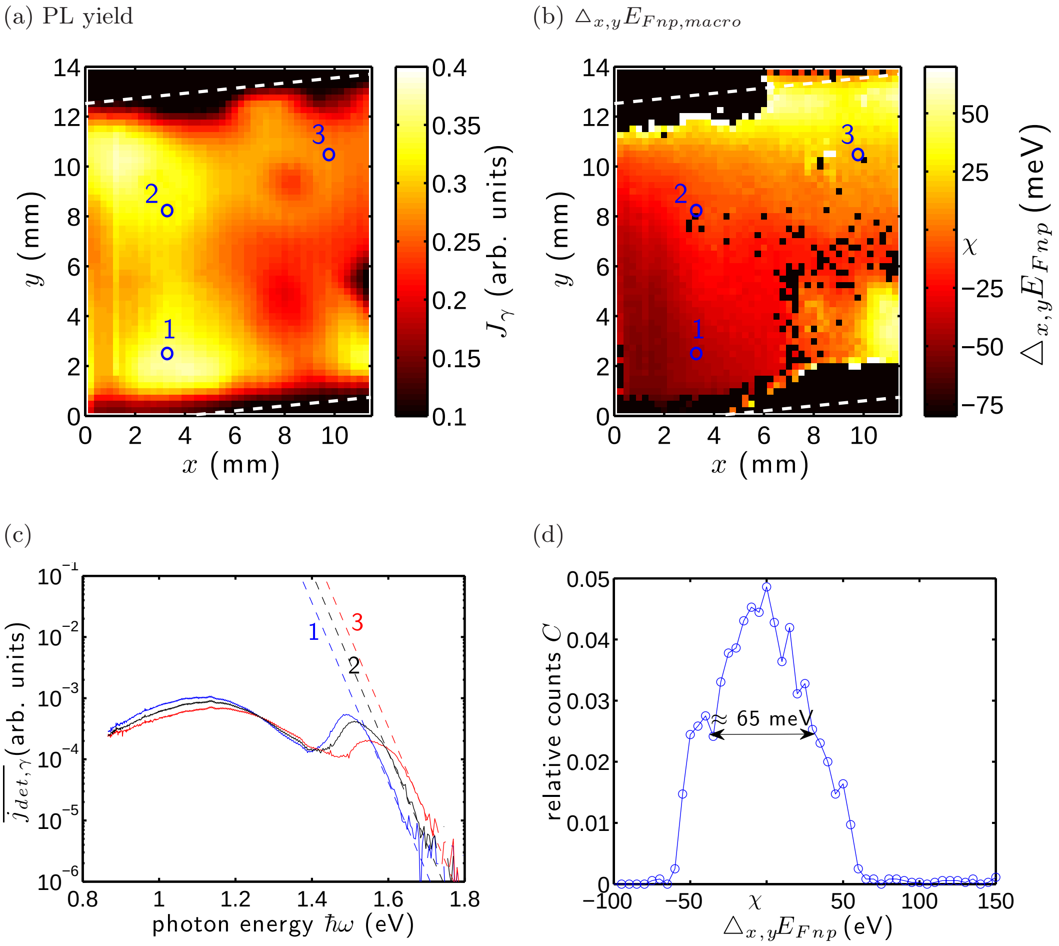

(a) PL yield

(b) $\triangle_{x,y}E_{Fnp,macro}$

(c)

(d)

Figure 5.27.: Laterally resolved macroscopic PL. The measurements have been carried out in the setup described in section 4.3. The lateral resolution is approximately 1 mm^2 and the excitation flux amounts to 115 mW with λ = 532 nm. 5.27a shows the PL yield of a Cu(In,Ga)S$_2$absorber layer (same sample analysed in section 5.1.1), the dashed lines mark the sample dimensions. 5.27b shows the extracted relative quasi-Fermi level splitting $\triangle_{x,y}E_{Fnp,macro}$. To extract $\triangle_{x,y}E_{Fnp,macro}$ the temperature T has been assumed constant at T = 330 K extracted from the averaged spectrum. In 5.27c the spectra for the marked positions and in 5.27d the histogram of $\triangle_{x,y}E_{Fnp,macro}$ are shown.

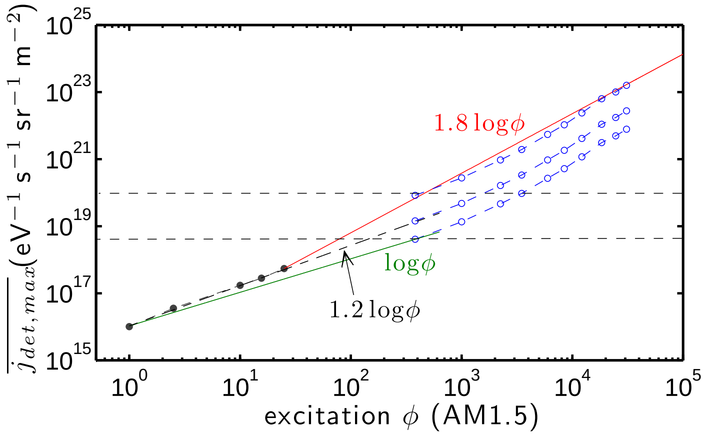

Figure 5.28.: Maximum $\overline{j_{\gamma,max}}$ of the PL yield for varying excitation ϕ. With the absolute photon fluxes extracted in calibrated PL measurements (black) an extrapolation towards the microscopic PL (blue) can be made. With $\beta_{micro} \approx 1.8$ (red), $\beta_{macro} \approx 1.2$ (black) and $\beta_{min} = 1$ (green).

measurements (figure 5.20) depending on the excitation flux ϕ. Since effects of superposition of laterally varying PL yields are comparably small, they have been neglected here. For macroscopic measurements the extracted exponent β_{macro} is 1.21 ± 0.09. It has to be taken into account, that sample heating for excitation on the macroscopic scale could not be avoided. This introduces another uncertainty and the exponent β_{macro} extracted according to $\overline{j_{\gamma,max}} \propto \phi^{\beta_{macro}}$ could actually be larger if sample heating could be avoided. Since the sample position in microscopic and macroscopic measurements is not exactly the same (also a different scan area), the assumption has to be made, that different positions have a similar exponent β. This assumption seems to be fulfilled, because even $CuInS_2$ and $Cu(In,Ga)S_2$ in micro PL have shown a similar β. The extrapolation reveals that the photon fluxes measured in laterally resolved measurements on the microscopic scale is in the range of $5 \times 10^{21}\,\mathrm{eV}^{-1}\mathrm{s}^{-1}\mathrm{sr}^{-1}\mathrm{m}^{-2}$ to $1 \times 10^{23}\,\mathrm{eV}^{-1}\mathrm{s}^{-1}\mathrm{sr}^{-1}\mathrm{m}^{-2}$ for 2.5×10^{4} AM1.5 equivalent fluxes. This corresponds to a quasi-Fermi level splitting close to/or in the range of the sub band-gap absorbance A_{def}.

In the next section the absorbance of macroscopic and microscopic PL measurements and a possible influence of the high excitation and respective high quasi-Fermi level splittings on the absorbance in microscopic PL measurements will be studied.

5.3.2. Absorbance

At first the macroscopic absorbance and particularly the lateral variation in sub band-gap absorbance A_{def}^{macro} (figure 5.29a) and in optical band-gap E_{opt}^{macro} (figure 5.29b) on the macroscopic scale are studied. The average optical band-gap is $\overline{E_{opt}^{macro}} \approx 1.57\,\mathrm{eV}$, it shows lateral fluctuations with a standard deviation of $\sigma_{E_{opt}}^{macro} \approx$

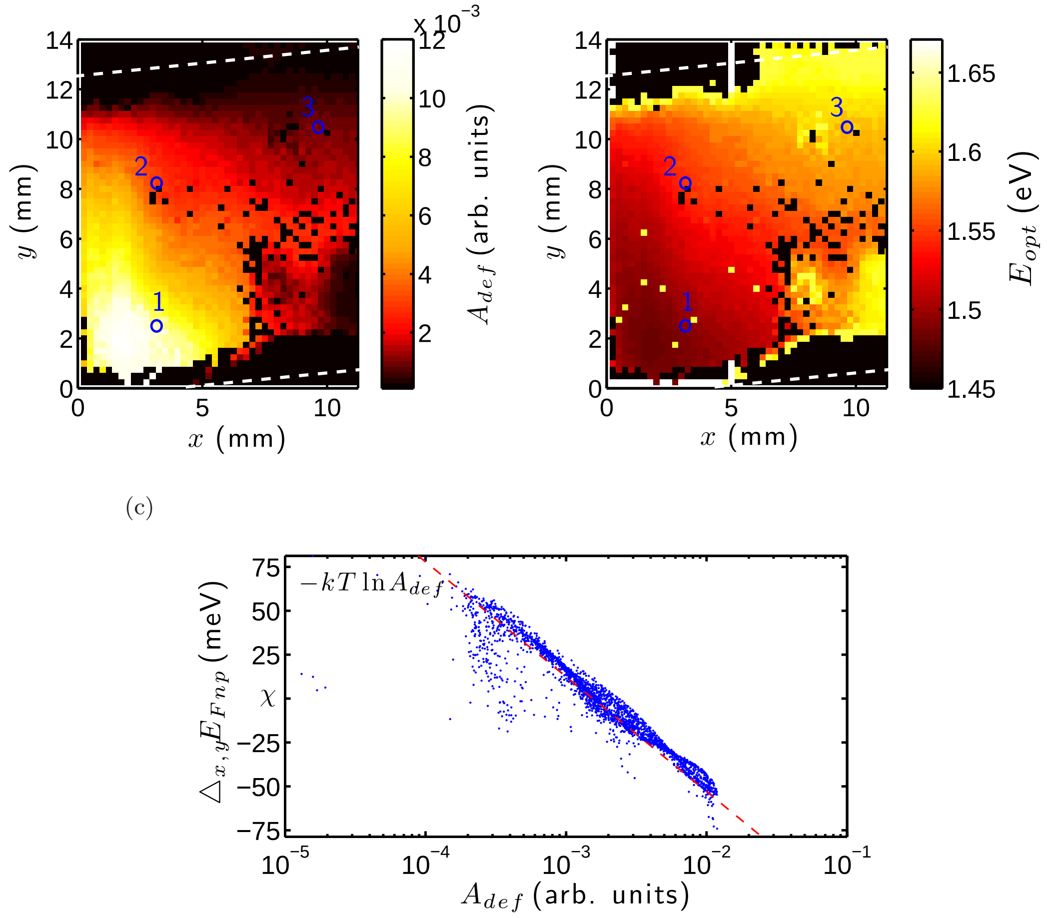
(a) Sub band-gap absorbance

(b) Optical band-gap

Figure 5.29.: a) Defect absorbance A_{def} extracted from the PL in figure 5.27a and b) quasi-Fermi level splitting $\triangle_{x,y}E_{Fnp}$ depending on local defect absorbance $A_{def}(x,y) \propto N_D(x,y)$, the dashed line corresponds to $-kT\ln(A_{def})$ with $T = 330\,\mathrm{K}$.

43 meV, thus even higher fluctuations than on the microscopic scale. A possible reason for these high variations could be due to large scale fluctuations during film growth and as a result a lateral variation of intermixture between Ga rich and In rich layer. Furthermore a — compared to microscopic measurements — higher correlation of $r(E_{opt}^{macro}, \triangle_{x,y} E_{Fnp}^{macro}) \approx 0.88$ to the local quasi-Fermi level splitting is found.

As in microscopic PL measurements a strong anti-correlation of $r = -0.82$ between $\triangle_{x,y} E_{Fnp}^{macro}$ and A_{def} exists and the model of eq. (5.8) ($\triangle_{x,y} E_{Fn} \approx -kT \ln(A_{def})$) is confirmed as well. In Figure 5.29c the local quasi-Fermi level splitting is plotted against A_{def}, the dashed line corresponds to $-kT \ln(A_{def})$ with $T \approx 330\,\mathrm{K}$ extracted from the PL spectra.

The main difference between micro- and macroscopic measured absorbance spectra is the difference in sub band-gap absorbance by up to about two orders of magnitude which leads to a decreased sub band-gap luminescence in microscopic PL. Figure 5.30a shows the absorbance A_{macro} of $\mathrm{CuInS_2}$ extracted from a macroscopic PL measurement at 10 AM1.5 equivalent fluxes. The dashed lines represent absorbance spectra extracted from a laterally resolved PL scan at approximately 2.5×10^4 AM1.5 equivalent fluxes. Although spectral variations on the microscopic scale are strong, a clear difference to macroscopic measurements at lower excitation is seen. Figure 5.30b shows absorbance spectra of $\mathrm{Cu(In,Ga)S_2}$ extracted from macroscopic (A_{macro}) and microscopic (A) PL measurements. The absorbance A has been averaged over a scan area of $60\,\mu\mathrm{m} \times 60\,\mu\mathrm{m}$ for different excitation fluxes ϕ. Increased excitation leads to a decrease in the absorbance below the optical band-gap.

In general the Fermi-Dirac occupation probability of electrons n and holes p involving degenerate levels of a defect site is given by [73]

$$\begin{aligned} f_n &= \left[g_n + \exp\left(\frac{E - E_{Fn}}{kT}\right)\right]^{-1} \\ f_p &= \left[g_p + \exp\left(\frac{E_{Fp} - E}{kT}\right)\right]^{-1}, \end{aligned} \tag{5.14}$$

where $g_n = g_p = 1$ if individual states are independent or say wave functions of the state are not well localized (especially in defects). This is the case for a broad defect band with a continuum of energy levels — as assumed to be present in the analyzed samples. For a higher excitation ϕ the splitting of quasi-Fermi levels $E_{Fn} - E_{Fp}$ increases, leading to a shift of the Fermi distributions as shown in figure 5.31. If the defect band D_1 is attached to the valence band, a higher E_{Fnp} leads to a depopulation of defect states D_1 by electrons or a population by holes. The absorption coefficient

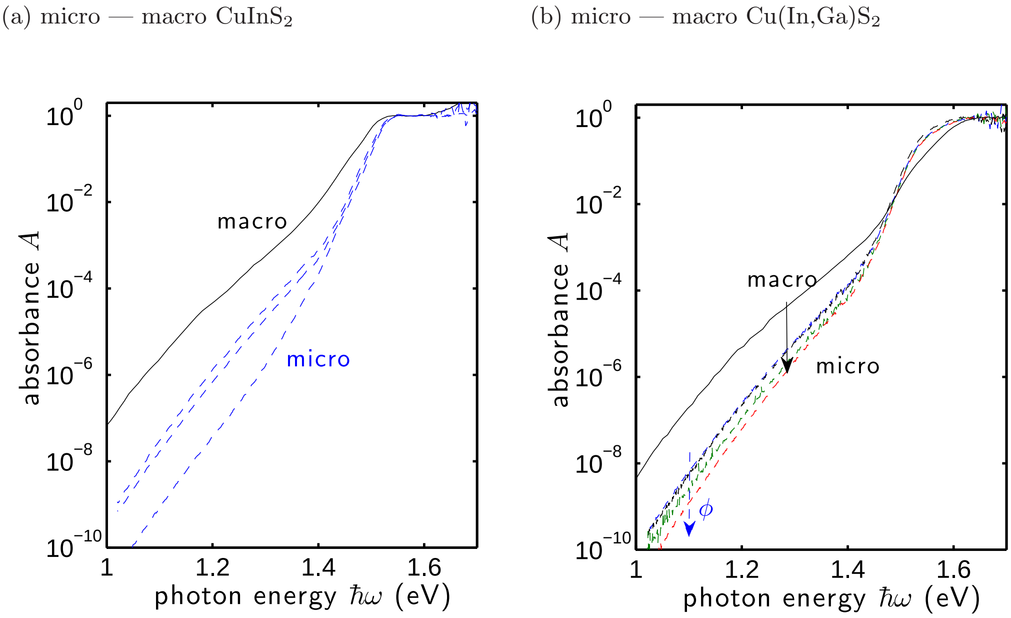
(a) micro — macro $CuInS_2$

(b) micro — macro $Cu(In,Ga)S_2$

Figure 5.30.: Absorbance spectra extracted from macroscopic calibrated Photoluminescence at 10 AM1.5 equivalents. Figure 5.30a shows $CuInS_2$ absorbance spectra extracted from microscopic laterally resolved PL at different sample positions (blue dashed) and macroscopic calibrated PL measurements (black) (figure 5.25). 5.30b shows $Cu(In,Ga)S_2$ absorbance spectra extracted from microscopic laterally resolved and average over a scan area of 60 µm × 60 µm for varying excitation flux ϕ in the range of $(1.2 \times 10^4$ to $3.7 \times 10^4)$ AM1.5 equivalents (dashed line) together with the macroscopic $Cu(In,Ga)S_2$ absorbance spectra of 5.26.

$\alpha(\hbar\omega)$ is determined by the transition between initial states D_i in valance band D_v and defects D_1 and final states D_f in the conduction band [13, 74]

$$\alpha(\hbar\omega) = \frac{n_r}{c} \int_0^\infty M(E, \hbar\omega) D_i(E) D_f(E + \hbar\omega) \left[f(E) - f(E + \hbar\omega) \right] \mathrm{d}E, \qquad (5.15)$$

with M containing the matrix elements which may depend on energies E and $\hbar\omega$. Thus a depopulation of D_1 by electrons (or population by holes) decreases the probability of transitions from valence band to D_1 and minimizes $\alpha(\hbar\omega)$ in the corresponding energy range. A similar situation would occur if D_1 was attached to the

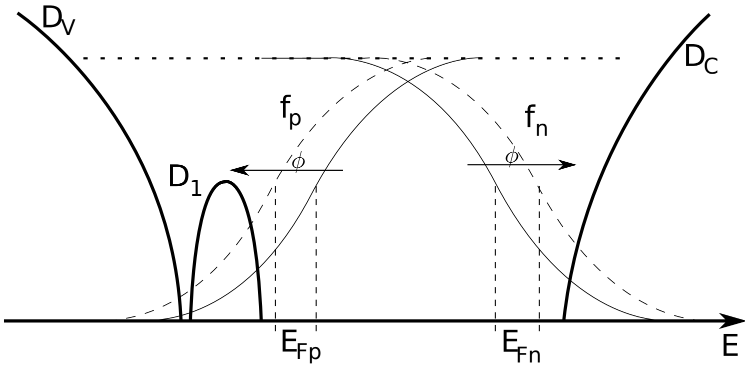

Figure 5.31.: Fermi-Dirac distribution of an illuminated semiconductor with defect band D_1 for varying energies E_{Fn} and E_{Fp}.

conduction band, furthermore transitions between two defect “bands” D_1' and D_1'' are also possible.

As seen in the previous section by a rough extrapolation, the average quasi-Fermi level splitting increases for excitation fluxes in the range of 2.5×10^4 AM1.5 equivalent fluxes to values close to/or in the vicinity of the sub band-gap absorbance. Since the Boltzmann approximation of Planck's generalized law is only valid for $\hbar\omega - E_{Fnp} \gg kT$, the absorbance A (eq. (3.13)) at photon energies in the vicinity or below the quasi-Fermi level splitting E_{Fnp} can not be extracted. On the other hand, the fact that experimental results of macroscopic laterally resolved measurements correspond to those extracted in microscopic measurements with high excitation (compare e.g. figure 5.12 and 5.29) points towards a lower quasi-Fermi level splitting and the applicability of the Boltzmann approximation.

6. Summary and Outlook

Photoluminescence analyses on the basis of Planck's generalized radiation law has proven as a comprehensive method to characterize opto-electronic absorber properties of polycrystalline $Cu(In_{1-\xi}Ga_{\xi})S_2$ thin films. However the transition from microscopic towards macroscopic photoluminescence measurements and the extraction of absolute quasi-Fermi level splittings proves difficult. The main reasons are the low luminescence yield of $Cu(In_{1-\xi}Ga_{\xi})S_2$ under AM1.5 equivalent conditions caused by the wide band-gap with a comparably small E_{Fnp} and strong lateral fluctuations of opto-electronic absorber parameters on microscopic as well as macroscopic scale.

The analyzed samples revealed a — compared to the thickness of the film — very high surface roughness ($\mathrm{FWHM}_h \approx 800\,\mathrm{nm}$ for $CuInS_2$ and $\mathrm{FWHM}_h \approx 700\,\mathrm{nm}$ for $Cu(In,Ga)S_2$), nevertheless no influence on the PL spectrum in terms of local quasi-Fermi level splitting could be found. Structure sizes in AFM surface contour and opto-electronic absorber properties have been studied by the use of Minkowski opening operations, which revealed grain sizes from 2 µm to 3 µm whereas structures in $\triangle_{x,y}E_{Fnp}$ ranges from 1 µm to 2 µm and in the optical band-gap E_{opt} from 1 µm to 3.5 µm. By the successive application of Minkowski opening operations on data sets of varying scan sizes a lower boundary for the statistical representativity of the underlying data set could be given. For the surface contour a minimum scan area of about $900\,\mu\mathrm{m}^2$ ($30\,\mu\mathrm{m}\times 30\,\mu\mathrm{m}$) was found. A similar area of $841\,\mu\mathrm{m}^2$ ($29\,\mu\mathrm{m}\times 29\,\mu\mathrm{m}$) was extracted for the variation in quasi-Fermi level splitting $\triangle_{x,y}E_{Fnp}$.

On the microscopic scale variations in the quasi-Fermi level splitting of about 38 meV in $CuInS_2$ and 53 meV in $Cu(In,Ga)S_2$ have been found, which is much larger than fluctuations measured under equivalent conditions in selenized absorber layers. In contrast to $Cu(In,Ga)Se_2$ no dependency of the extend in lateral variation of$\triangle_{x,y}E_{Fnp}$ on the excitation flux ϕ could be found. In the case of Ga doped samples a varying Ga to In ratio over the film thickness leads to a band-gap gradient with a high E_g regime at the back and a low E_g regime close to the surface of the absorber layer. This causes gradients in e.g. E_{Fnp}, absorption coefficient etc. An estimation showed, that in the case of a relatively thin high band-gap region (compared to the thickness of the absorber layer) parameters extracted from PL correspond in good approximation to those of the In rich layer close to the front surface. On the other hand, if the In rich layer gets thinner a linear regression of the high energy wing of the PL does not necessarily yield the correct slope of the Bose term ($-1/kT$) and thus errors of extracted parameters increase.

On the macroscopic scale (mm-regime), the extraction of quasi-Fermi level splittings from PL spectra calibrated for absolute photon fluxes proves difficult. Due to larger detection/excitation areas sample heating can not be avoided and low PL yields (as well as large band-gap fluctuations in Cu(In,Ga)S$_2$) lead to high errors in the extracted E_{Fnp}. The non-linear superposition of laterally varying E_{Fnp} beneath the optical resolution in large scale detection leads to an overestimation of extracted quasi-Fermi level splittings $E_{Fnp,macro}$. A study for gaussian shaped variations $\triangle_{x,y}E_{Fnp}$ with standard deviation $\sigma_{E_{Fnp}}$ revealed an overestimation by the factor $\sigma^2_{E_{Fnp}}/(2kT)$, which in the case of Cu(In$_{1-\xi}$Ga$_\xi$)S$_2$ absorber layers is small compared to the error caused by a linear approximation of the Bose term.

The local absorbances of thin films have been extracted by the help of Planck's generalized law. It has been found, that Cu(In,Ga)S$_2$ layers show strong fluctuations in the optical band-gap of about FWHM$_{E_{opt}} \approx 80\,\text{meV}$ ($\triangle_{x,y}E_g \approx 70\,\text{meV}$) on the microscopic scale, whereas fluctuations E_{opt} in CuInS$_2$ are negligible compared to fluctuations in E_{opt} caused by thickness variations. Thus band-gap fluctuations seem to be caused by a varying Ga content or varying intermixture of Ga rich regime at the back and In rich regime at the front of the absorber. For regions with higher E_{opt} and with it a potential higher Ga content, a higher quasi-Fermi level splitting was found.

As a major limiting factor for the local quasi-Fermi level splitting E_{Fnp} the local density of deep defects could be identified. Between defect absorbance A_{def} and the lateral variation $\triangle_{x,y}E_{Fnp}$ an anti-correlation was found that can described by $\triangle_{x,y}E_{Fn} \approx -kT\ln(N_{def}) \propto -kT\ln(A_{def})$ on microscopic as well as macroscopic scale. The energetic position of the maximum of these deep defects at room temperature PL corresponds to published values of an — until now — unidentified defect "band".

A characterization of shallow defects has been carried out by laterally resolved micro PL at low temperatures ($T_{cryo} = 85\,\text{K}$, $100\,\text{K}$ and $130\,\text{K}$). Different radiative transitions with laterally varying photon energy are visible. Clearly identifiable is a transition at $1.45\,\text{meV} \pm 0.01\,\text{meV}$, which — with high probability — is caused by a donor-acceptor recombination. For an exact classification however, additional excitation dependent measurements are necessary. Since the Coulomb term in the transition energy of eq. (5.9) increases with increasing excitation, the peak visible in the PL spectrum would shift to higher energies.

For all scans with small detection areas high excitation fluxes (in the range of 10^4 AM1.5 equivalents) are necessary to get detectable PL yields. Such high excitation fluxes go along with a high quasi-Fermi level splitting. An estimation of the extend of E_{Fnp} in these microscopic PL measurements yields values for E_{Fnp} in the vicinity of the defect luminescence. Due to large uncertainties no exact value for E_{Fnp} could be given, thus a clear answer to the problem up to which photon energies the Boltzmann approximation and with it the extraction of the local absorbances A is mathematically correct could not be given. However laterally and spectrally resolved PL with high (microscopic) and low (macroscopic) excitation fluxes yield similar results. The major difference measured between microscopic and macroscopic scale is the decrease of sub band-gap absorption with increasing quasi-Fermi level splitting or increasing excitation. A possible explanation is given in figure 5.31, the increased quasi-Fermi level splitting leads to a depopulation of defect states, which decreases the sub band-gap absorbance that depends on the quantity of possible transitions (see eq. (5.15)).

Absorber layers without Mo back contact offer a wider range of characterization possibilities (e.g. detection of PL emitted through front and back surface and micro transmission), however since growths conditions of samples grown directly on the substrate differ considerably from absorber layers grown on Mo coated substrates, results are not directly transferable to other samples. Mappings of photoluminescence yields emitted through front and back surface show similar structures, thus most grains can be assumed to extend throughout the absorber layer. Optical micro transmission on these samples proves difficult, since the transmission in the low photon energy regime seems to be mainly influenced by the surface topology of the absorber layer and due to the high surface roughness no interference patterns can be detected.

Problems which have not been addressed or that came up during this work are e.g. a more detailed analysis of potential temperature fluctuations during PL scans with sub-micron resolution, which could be caused by laterally varying defect concentrations and an increased non-radiative recombination. For measurements at room temperature fluctuations in the slope of the Bose term $-1/kT$ could not be identified as variations in temperature but are mainly due to uncertainties of the fit. A more detailed analysis of laterally resolved PL at low temperatures could be promising.

Conclusions about the excess carrier and quasi-Fermi level splitting profile could possibly be drawn from measuring PL emitted through front and back surface of an absorber layer. Even though this would only be possible by a parameter optimization and go along with high computing time. Moreover the solution might not be unique without further knowledge about the absorber layers. Nevertheless the solution of the semiconductor equations for absorber layers with graded properties could give detailed knowledge on the emitted PL yield.

Finally, an additional starting point for an extensive analysis of defects could be laterally and spectrally resolved PL at low temperatures or the study of excitation dependent absorption e.g. by photothermal deflection spectroscopy (PDS).

Bibliography

[1] I. Repins, M. Contreras, B. Egaas, C. DeHart, J. Scharf, C. Perkins, B. To, and R. Noufi, “19.9% efficient ZnO/CdS/CuInGaSe$_2$ solar cell with 81.2% fill factor,” *Progress in Photovoltaics: Research and Applications*, vol. 16, no. 3, pp. 235–239, 2008.

[2] M. A. Green, K. Emery, Y. Hishikawa, and W. Warta, “Solar cell efficiency tables,” *Progress in Photovoltaics: Research and Applications*, vol. 18, pp. 346–352, 2010.

[3] R. Klenk, J. Klaer, R. Scheer, M.-C. Lux-Steiner, I. Luck, N. Meyer, and U. Rühle, “Solar cells based on CuInS$_2$ - an overview,” *Thin Solid Films*, vol. 480, pp. 509–514, 2005.

[4] J. Klaer, R. Klenk, and H. W. Schock, “Progress in the development of CuInS$_2$ based mini-modules,” *Thin Solid Films*, vol. 515, no. 15, pp. 5929–5933, 2007.

[5] R. Kaigawa, A. Neisser, R. Klenk, and M.-C. Lux-Steiner, “Improved performance of thin film solar cells based on Cu(In,Ga)S$_2$,” *Thin Solid Films*, vol. 415, pp. 266–271, 2002.

[6] R. Mainz, F. Streicher, D. Abou-Ras, S. Sadewasser, R. Klenk, and M.-C. Lux-Steiner, “Combined analysis of spatially resolved electronic structure and composition on a cross-section of a thin film Cu(In$_{1-x}$Ga$_x$)S$_2$ solar cell,” *Phys. Status Solidi A*, vol. 206, no. 5, pp. 1017–1020, 2009.

[7] K. Taretto and U. Rau, “Numerical simulation of carrier collection and recombination at grain boundaries in Cu(In,Ga)Se$_2$ solar cells,” *Journal of Applied Physics*, vol. 103, no. 094523, 2008.

[8] K. Bothe, G. H. Bauer, and T. Unold, “Spatially resolved photoluminescence measurements on Cu(In,Ga)Se$_2$ thin films,” *Thin Solid Films*, vol. 403-404, pp. 453–456, 2002.

[9] P. Basu, *Theory of optical Processes in Semiconductors.* Oxford University Press, Oxford, 1997.

[10] C. Klingshirn, *Semiconductor Optics.* Springer, Berlin, second ed., 2005.

[11] D. R. Vij, ed., *Handbook of Applied Solid State Spectroscopy.* Springer, Berlin, 2006.

[12] J. Singh, *Optical Properties of Condensed Matter.* John Wiley & Sons Ltd, Chichester, 2006.

[13] P. Würfel, "The chemical potential of radiation," *J. Phys. C: Solid State Phys.*, vol. 15, pp. 3967–3985, 1982.

[14] K. Schick, E. Daub, S. Finkbeiner, and P. Würfel, "Verification of a generalized planck law for luminescence radiation from silicon solar cells," *Appl. Phys. A*, vol. 54, no. 109, 1992.

[15] P. Würfel, S. Finkbeiner, and E. Daub, "Generalized Plancks radiation law for luminescence via indirect transitions," *Applied Physics A*, vol. 60, no. 1, pp. 67–70, 1995.

[16] T. Trupke, E. Daub, and P. Würfel, "Absorptivity of silicon solar cells obtained from luminescence," *Solar Energy Materials and Solar Cells*, vol. 53, no. 1-2, pp. 103–104, 1998.

[17] S. Tardon, *Quantitative Photoluminescence Studies in a-Si:H/c-Si Solar Cells.* PhD thesis, Carl von Ossietzky Universität Oldenburg, 2005.

[18] P. Würfel, T. Trupke, T. Puzzer, E. Schäfer, W. Warta, and S. Glunz, "Diffusion length of silicon solar cells from luminescence images," *Journal of Applied Physics*, vol. 101, no. 123110, 2007.

[19] S. Siebentritt and U. Rau, eds., *Wide-Gap Chalcopyrites.* Springer, 1 ed., 2006.

[20] L. Gütay and G. H. Bauer, "Local fluctuations of absorber properties of Cu(In,Ga)Se_2 by sub-micron resolved PL towards "real life" conditions," *Thin Solid Films*, vol. 517, pp. 2222–2225, 2009.

[21] L. Gütay, *Konfokale Photolumineszenz von Cu(In, Ga)Se_2.* PhD thesis, Carl von Ossietzky Universität Oldenburg, 2008.

[22] U. Rau and J. H. Werner, "Radiative efficiency limits of solar cells with lateral band-gap fluctuations," *Applied Physics Letters*, vol. 84, no. 19, 2004.

[23] J. Klaer, R. Klenk, D. Abou-Ras, R. Scheer, and H. W. Schock, "Progress in mini-modules from a $CuInS_2$ baseline process," *21st European Photovoltaic Solar Energy Conference*, 2006.

[24] K. Siemer, J. Klaer, I. Luck, J. Bruns, R. Klenk, and D. Bräunig, "Efficient $CuInS_2$ solar cells from rapid thermal process (RTP)," *Solar Energy Materials and Solar Cells*, vol. 67, pp. 159–166, 2001.

[25] S. Merdes, B. Johnson, J. Klaer, R. Klenk, I. Lauermann, R. Mainz, and A. Meeder, "Current transport in $Cu(In,Ga)S_2$ based solar cells with high open circuit voltage - bulk vs. interface," *Mater. Res. Soc. Symp. Proc.*, vol. 1165, pp. 1165–M05–15, 2009.

[26] R. Mainz, *In-situ Analyse und Wachstum photovoltaischer Absorber mit Bandlückengradienten.* PhD thesis, Freie Universität Berlin, 2008.

[27] A. Neisser, *Gallium as an Isovalent Substitution in $CuInS_2$ Absorber Layers for Photovoltaic Applications.* PhD thesis, Freie Universität Berlin, 2001.

[28] J. L. Shay, B. Tell, H. M. Kasper, and L. M. Schiavone, "p-d hybridization of the valence bands of $I\text{-}III\text{-}VI_2$ compounds," *Physical Review B*, vol. 5, no. 12, 1972.

[29] H. Neumann, W. Hörig, V. Savlev, J. Lagzdonis, B. Schumann, and G. Kühn, "The optical properties of $CuInS_2$ thin films," *Thin Solid Films*, vol. 79, pp. 167–171, 1981.

[30] H. Miyakea, M. Hataa, Y. Hamamurah, and K. Sugiyama, "Growth of $CuGaS_2$ single crystals by the traveling heater method using Cul solvent," *Journal of Crystal Growth*, vol. 144, pp. 236–242, 1994.

[31] H. Fan, W. Spitzer, and R. Collins, "Infrared absorption in n-type Germanium," *Physical Review*, vol. 101, no. 2, 1956.

[32] D. Thomas, "Infrared absorption in Zinc oxide crystals," *J. Phys. Chem. Solids.*, vol. 10, pp. 47–51, 1959.

[33] W. Baer, "Free-carrier absorption in reduced $SrTiO_3$," *Physical Review*, vol. 144, no. 2, 1966.

[34] P. Emelie, J. Phillips, B. Buller, and U. Venkateswaran, “Free carrier absorption and lattice vibrational modes in bulk ZnO,” *Journal of Electronic Materials*, vol. 35, no. 4, 2006.

[35] C. Thompson, “Grain growth in thin films,” *Annual Review of Materials Science*, vol. 20, pp. 245–268, 1990.

[36] T. Schlenker, M. Valero, H. Schock, and J. Werner, “Grain growth studies of thin Cu(In,Ga)Se_2 films,” *Journal of Crystal Growth*, vol. 264, pp. 178–183, 2004.

[37] O. Stenzel, *Das Dünnschichtspektrum.* Akademie Verlag, Berlin, 1996.

[38] P. Würfel, *Physics of Solar Cells.* Wiley-VCH, Berlin, 1 ed., 2004.

[39] S. Knabe, L. Gütay, and G. H. Bauer, “Interpretation of quasi-fermi level splitting in Cu(Ga,In)Se_2-absorbers by confocally recorded spectral luminescence and numerical modeling,” *Thin Solid Films*, vol. 517, pp. 2344–2348, 2009.

[40] G. H. Bauer, R. Brüggemann, S. Tardon, S. Vignoli, and R. Kniese, “Quasi-fermi level splitting and identification of recombination losses from room temperature luminescence in $Cu(In_{1-x}Ga_x)Se_2$ thin films versus optical band gap,” *Thin Solid Films*, vol. 480, no. 410-414, 2005.

[41] L. Gütay and G. H. Bauer, “Analysis of band gap fluctuations in Cu(In,Ga)Se_2 by confocal optical transmission and photoluminescence,” *Mater. Res. Soc. Symp. Proc. Materials Research Society*, vol. 1012, no. Y08-03, 2007.

[42] E. Daub and P. Würfel, “Ultralow values of the absorption coefficient of Si obtained from luminescence,” *Physical Review Letters*, vol. 74, no. 6, 1995.

[43] M. I. Alonso, M. Garriga, C. A. Durante-Rincon, E. Hernandez, and M. Leon, “Optical functions of chalcopyrite $CuGa_xIn_{(1-x)}Se_2$ alloys,” *Appl. Phys. A*, vol. 74, pp. 659–664, 2002.

[44] T. Dullweber, G. Hanna, W. Shams-Kolahi, A. Schwartzlander, M. Contreras, R. Noufi, and H.-W. Schock, “Study of the effect of gallium grading in Cu(In,Ga)Se_2,” *Thin Solid Films*, vol. 361-362, pp. 478–481, 2000.

[45] M. Topič, F. Smole, and J. Furlan, “Band-gap engineering in CdS/Cu(In,Ga)Se2 solar cells,” *Journal of Applied Physics*, vol. 79, no. 11, 1996.

[46] J. Song, S. S. Li, C. H. Huang, O. D. Crisalle, and T. J. Anderson, "Device modeling and simulation of the performance of Cu(In$_{1-x}$,Ga$_x$)Se$_2$ solar cells," *Solid-State Electronics*, vol. 48, pp. 73–79, 2004.

[47] D. R. Lide, *CRC Handbook of Chemistry and Physics*, vol. 75. CRC Press, Boca Raton, Florida, 1994.

[48] T. Unold, I. Sieber, and K. Ellmer, "Efficient CuInS$_2$ solar cells by reactive magnetron sputtering," *Applied Physics Letters*, vol. 88, no. 213502, 2006.

[49] I. N. Bronstein, K. A. Semendjajew, G. Musiol, and H. Mühlig, *Taschenbuch der Mathematik.* Verlag Harri Deutsch, Frankfurt am Main, 2001.

[50] S. Knabe, M. Langemeyer, F. Heidemann, R. Brüggemann, and G. H. Bauer, "Study of the effect of excess carrier lifetime depth profiles and depth dependent absorption coefficients on the emitted photoluminescence spectrum of chalcopyrite thin films," *Progress in Photovoltaics: Research and Applications*, 2011.

[51] A. Davydov, "Theory of Urbach's rule," *phys. stat. sol.*, vol. 27, no. 51, 1968.

[52] A. F. Halverson, P. T. Erslev, J. Lee, J. D. Cohen, and W. N. Shafarman, "Characterization of the electronic properties of wide bandgap CuIn(Se,S)$_2$ alloys," *Mater. Res. Soc. Symp. Proc.*, vol. 865, no. F16.3, 2005.

[53] S. Ostapenko, I. Tarasov, J. Kalejs, C. Haessler, and E. Reisner, "Defect monitoring using scanning photoluminescence spectroscopy in multicrystalline silicon wafers," *Semicond. Sci. Technol.*, vol. 15, pp. 840–848, 2000.

[54] S. Ostapenko, I. Tarasov, and J. Kalejs, "Defect characterization in multicrytsalline silicon using scanning techniques," *Solid State Phenomena*, vol. 78-79, pp. 259–266, 2001.

[55] J. Eberhardt, *Photolumineszenz epitaktischer und polykristalliner CuInS$_2$-Schichten für Dünnschichtsolarzellen.* PhD thesis, Friedrich-Schiller-Universität Jena, 2007.

[56] J. Eberhardt, K. Schulz, H. Metzner, J. Cieslak, T. Hahn, U. Reisloehner, M. Gossla, F. Hudert, R. Goldhahn, and W. Witthuhn, "Epitaxial and polycrystalline CuInS$_2$ thin films: A comparison of opto-electronic properties," *Thin Solid Films*, vol. 515, no. 15, pp. 6147–6150, 2007.

[57] H. Lewerenz and N. Dietz, “Defect identification in semiconductors by brewster angle spectroscopy,” *Journal of Applied Physics*, vol. 73, no. 10, 1993.

[58] I. Riedel, J. Riediger, J. Ohland, J. Keller, M. Knipper, J. Parisi, R. Mainz, and S. Merdes, “Photoelectric characterization of Cu(In,Ga)S_2 solar cells obtained from rapid thermal processing at different temperatures,” *Solar Energy Materials and Solar Cells*, 2010.

[59] R. Scheer, R. Klenk, J. Klaer, and I. Luck, “$CuInS_2$ based thin film photovoltaics,” *Solar Energy*, vol. 77, pp. 777–784, 2004.

[60] H. J. Hsu, M. H. Yang, R. S. Tang, T. M. Hsu, and H. L. Hwang, “A novel method to grow larger $CuInS_2$ single crystals,” *Journal of Crystal Growth*, vol. 70, pp. 427–432, 1984.

[61] K. Töpper, J. Bruns, R. Scheer, M. Weber, A. Weidinger, and D. Bräunig, “Photoluminescence of $CuInS_2$ thin films and solar cells modified by postdeposition treatments,” *Appl. Phys. Lett.*, vol. 71, no. 4, 1997.

[62] J. Binsma, L. Giling, and J. Bloem, “Luminescence of $CuInS_2$,” *Journal of Luminescence*, vol. 27, pp. 35–53, 1982.

[63] H. Ueng and H. Hwang, “The defect structure of $CuInS_2$. Part I: Intrinsic defects,” *J. Phys. Chem. Solids.*, vol. 50, no. 12, pp. 1297–1305, 1989.

[64] H. Ueng and H. Hwang, “The defect structure of $CuInS_2$. Part II: Thermal annealing defects,” *J. Phys. Chem. Solids.*, vol. 51, no. 1, pp. 1–10, 1990.

[65] B. Tell, J. L. Shay, and H. M. Kasper, “Electrical properties, optical properties and band structure of $CuGaS_2$ and $CuInS_2$,” *Physical Review B*, vol. 4, no. 8, 1971.

[66] N. Lahlou and G. Massé, “Donor-acceptor pair transitions in $CuInS_2$,” *Journal of Applied Physics*, vol. 52, no. 2, 1981.

[67] A. W. Verheijen, L. J. Gilling, and J. Bloem, “The region of existence of $CuInS_2$,” *Mater. Res. Bull.*, vol. 14, p. 237, 1979.

[68] T. M. Hsu and J. H. Lin, “Anomalous temperature-dependent band-gaps in $CuInS_2$ studied by surface-barrier electroreflectance,” *Physical Review B*, vol. 37, no. 8, pp. 4106–4110, 1988.

[69] T. M. Hsu, "The electron-phonon contribution to the energy gap in $CuInS_2$," *Physics Letters A*, vol. 133, no. 1,2, pp. 79–81, 1988.

[70] L. Gütay, C. Lienau, and G. H. Bauer, "Subgrain size inhomogeneities in the luminescence spectra of thin film chalcopyrites," *Applied Physics Letters*, vol. 97, no. 052110, 2010.

[71] R. N. Hall, "Electron-hole recombination in germanium," *Physical Review*, vol. 87, p. 387, 1952.

[72] W. Shockley and W. T. Read, "Statistics of the recombinations of holes and electrons," *Physical Review*, vol. 87, no. 5, 1952.

[73] G. Lasher and F. Stern, "Spontaneous and stimulated recombination radiation in semiconductors," *Physical Review*, vol. 133, no. 2A, pp. A553–A563, 1964.

[74] F. Stern, "Elementary theory of the optical properties of solids," *Solid State Physics*, vol. 15, pp. 299–408, 1963.

[75] C. R. Giardina and E. R. Dougherty, *Morphological methods in image and signal processing.* Prentice Hall, New Jersey, 1988.

[76] P. Soille, *Morphologische Bildverarbeitung.* Springer, Berlin, 1998.

[77] R. Fuhrmann, "Ensemble analysis of spatially resolved sub-micrometer structures," Studienarbeit, Carl von Ossietzky Universität Oldenburg, 2005.

[78] G. H. Bauer, L. Gütay, and R. Fuhrmann, "Extraction of features from 2-D laterally sub-micron resolved photoluminescence in $Cu(In,Ga)Se_2$ absorbers by Fourier transforms and Minkowski-operations," *Thin Solid Films*, vol. 511, p. 309, 2006.

Appendices

A. Graded Band-Gap

The analytical solution of the integral over a depth dependent absorption coefficient α (see also section 3.1.2)

$$\alpha(z, \hbar\omega) = \frac{a}{\hbar\omega}\sqrt{\hbar\omega - E_g(z)} \tag{A.1}$$

with graded band-gap $E_g(z)$ according to

$$E_g(z) = \frac{E_{g,0} - E_{g,d}}{\exp\left(\frac{z-z_t}{z_w}\right) + 1} + E_{g,d} \tag{A.2}$$

has been calculated using a computer algebra system. The solution of the integral is given by

$$\begin{aligned}\int \alpha(z, \hbar\omega)\mathrm{d}\hbar\omega \quad = \quad & \frac{a z_w}{\hbar\omega\sqrt{\hbar\omega - E_{g,d}}}\left[\hbar\omega \ln\left\{\frac{\beta + 2\zeta\sqrt{\hbar\omega - E_{g,d}}}{2\sqrt{\hbar\omega - E_{g,d}}}\right\} - \right. \\ & E_{g,d}\ln\left\{\frac{\beta + 2\zeta\sqrt{\hbar\omega - E_{g,d}}}{2\sqrt{\hbar\omega - E_{g,d}}}\right\} - \sqrt{\hbar\omega - E_{g,0}}\sqrt{\hbar\omega - E_{g,d}} \times \\ & \left.\ln\left\{\frac{\beta - E_{g,0} - E_{g,0}\mathrm{e}^{\left(\frac{z-z_t}{z_w}\right)} + 2\zeta\sqrt{\hbar\omega - E_{g,0}}}{\mathrm{e}^{\left(\frac{z-z_t}{z_w}\right)}}\right\}\right]\end{aligned} \tag{A.3}$$

with abbreviations β and ζ

$$\begin{aligned}\zeta &= \sqrt{\left(\hbar\omega - E_{g,d}\right)\left(\mathrm{e}^{\left(\frac{z-z_t}{z_w}\right)}\right)^2 + \left(2\hbar\omega - E_{g,0} - E_{g,d}\right)\mathrm{e}^{\left(\frac{z-z_t}{z_w}\right)} + \hbar\omega - E_{g,0}} \\ \beta &= 2\hbar\omega - E_{g,0} - E_{g,d} + 2\left(\hbar\omega - E_{g,d}\right)\mathrm{e}^{\left(\frac{z-z_t}{z_w}\right)}.\end{aligned} \tag{A.4}$$

B. Log-Normal Distribution

When the logarithm of a magnitude X is normally distributed a log-normal distribution exists, which is defined by [49]

$$f_{X,\log}(x) = \frac{a_1}{x}\exp\left(-\frac{(\ln x - M_L)^2}{2\sigma_{M_L}^2}\right), \tag{B.1}$$

with parameters a_1, M_L and σ_{M_L}. Mean $\overline{X}$, median $\widetilde{X}$ and standard deviation σ_X of the magnitude X are related to M_L and σ_{M_L} by

$$\begin{aligned} \overline{X} &= \exp\left(M_L + \frac{\sigma_{M_L}^2}{2}\right) \\ \widetilde{X} &= \exp M_L \\ \sigma_X &= \sqrt{\left(\mathrm{e}^{\sigma_{M_L}^2} - 1\right)\exp\left(2M_L + \sigma_{M_L}^2\right)}. \end{aligned} \tag{B.2}$$

The median $\widetilde{X}$ identifies the border between upper and lower half of a distribution (for a gaussian $\overline{X} = \widetilde{X}$), it has the advantage of being more robust towards outliers. The log-normal distribution is often used to describe distributions resulting from a growth processes, e.g. in semiconductor physics the distribution of grain sizes [35]. Figure B.1 shows the distribution of grain sizes as extracted by the Minkowski opening procedure (summation over all heights h in figure 2.4) fitted by a log-normal distribution according to eq. (B.1) with $\widetilde{d} \approx 2.9\,\mu\mathrm{m}$ ($M_L = 1.1 \pm 0.1$) and $\sigma_d \approx 3.8\,\mu\mathrm{m}$ ($\sigma_{M_L} = 0.8 \pm 0.04$) for $\mathrm{CuInS_2}$ and $\widetilde{d} \approx 2.6\,\mu\mathrm{m}$ ($M_L = 0.96 \pm 0.05$) and $\sigma_d \approx 3.1\,\mu\mathrm{m}$ ($\sigma_{M_L} = 0.77 \pm 0.04$) for Cu(In,Ga)$\mathrm{S_2}$ according to eq. (B.2). Log-normal distributed grain sizes have been measured before on Cu(In,Ga)$\mathrm{Se_2}$ thin films [36].

The photoluminescence yield and the opto-electronic properties extracted from PL spectra show a similar distribution that can be described by eq. (B.1) (see also section 5.1). Figure B.2a and B.2b show a double logarithmic plot with histograms of the lateral fluctuation in PL yield J_γ and sub band-gap absorbance A_{def} of a CIGS sample fitted by a log-normal distribution with $\widetilde{J_\gamma} \approx 0.67$ ($M_L = -0.41 \pm 0.01$), $\sigma_{J_\gamma} \approx 0.51$ ($\sigma_{M_L} = 0.59 \pm 0.01$) and $\widetilde{A}_{def} \approx 0.0043$ ($M_L = -5.4 \pm 0.3$), $\sigma_{A_{def}} \approx 0.057$ ($\sigma_{M_L} = 1.6 \pm 0.4$). For comparison a normal distribution is also plotted. For comparably

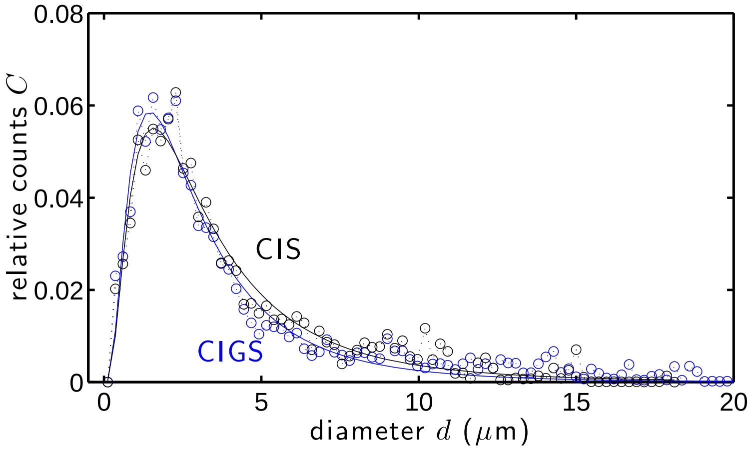

Figure B.1.: Distribution of grain sizes in the analyzed $Cu(In_{1-\xi}Ga_{\xi})S_2$ absorber layers.

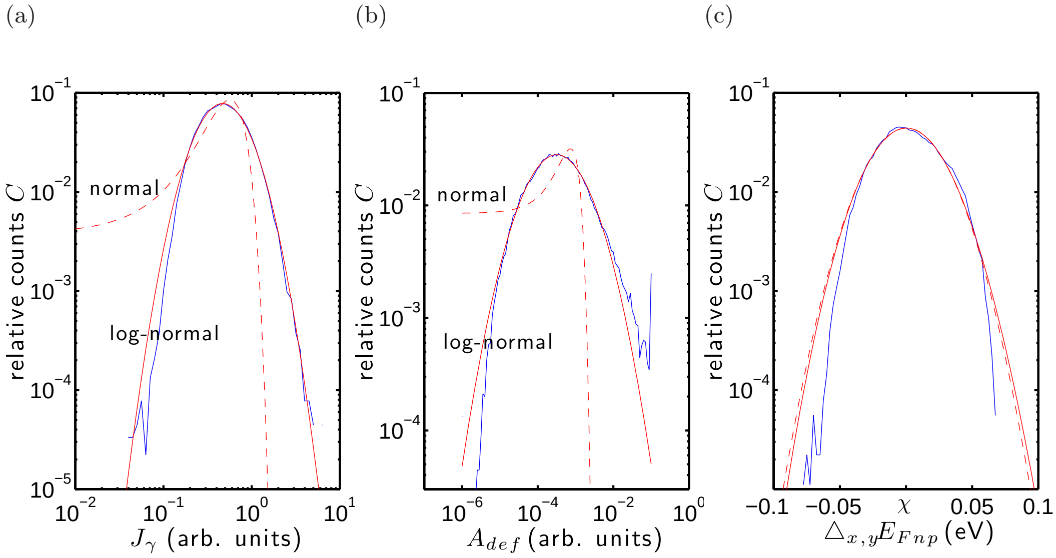

Figure B.2.: Log-normal distributions fitted to the histogram of lateral fluctuations in PL yield J_γ (B.2a), sub band-gap absorbance A_{def} (B.2b) and quasi-Fermi level splitting $\triangle_{x,y}E_{Fnp}$ (B.2c) of CIGS. Data set from figures 5.2, 5.11 and 5.5. For comparison the dashed lines lines represent a normal distribution.

small fluctuations as in $\triangle_{x,y}E_{Fnp}$ (figure B.2c), gaussian and log-normal distribution become similar.

C. Morphological Image Analysis

In this section an overview on morphological or Minkowski image analysis will be given starting with the introduction of the fundamental morphological operations necessary to apply the analysis. For more detailed information on this topic the reader is referred to the appropriate literature [75, 76].

In the Minkowski algebra an image A is a subset of the Euclidean plane $\mathbb{R}^2$, a translation of A by the vector $x \in \mathbb{R}^2$ is given by

$$A + x = \{a + x | a \in A\}. \tag{C.1}$$

With eq. (C.1) the Minkowski operations are defined

$$\begin{aligned} \text{Minkowski addition:} \quad A \oplus B &= \bigcup_{b \in B} A + b \\ \text{Minkowski substraction:} \quad A \ominus B &= \bigcap_{b \in B} A + b. \end{aligned} \tag{C.2}$$

That is the translation of A by each element of B and then taking the union (addition) or the intersection (subtraction). The Minkowski addition by a structuring element B is also called a dilatation $\mathcal{D}(A, B) = A \oplus B$, it has the effect of "expanding" an image (see figure C.1a). The corresponding operation to "shrink" an image is the erosion, it is defined by subtracting a structuring element $-B$ (see figure C.1b)

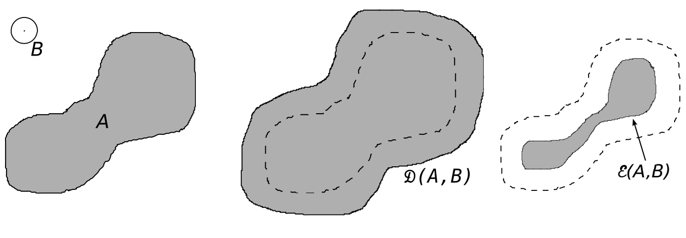
(a) dilatation

(b) erosion

Figure C.1.: dilatation, erosion and opening

$$\mathcal{E}(A, B) = A \ominus (-B) = \{x | B + x \subset A\}. \tag{C.3}$$

With these operations the opening of an image can be defined as the successive application of erosion and dilatation

$$\mathcal{O}(A,B) = [A \ominus (-B)] \oplus B = \mathcal{D}[\mathcal{E}(A,B),B]. \tag{C.4}$$

The opened set $\mathcal{O}(A,B)$ can also be expressed as the union of all structuring elements B that fit into the original set A

$$\mathcal{O}(A,B) = \bigcup\{B|B \subseteq A\}. \tag{C.5}$$

When applying the opening procedure on images with varying magnitude (e.g. a grayscale image in contrast to a black and white image) a parameterized opening has to be carried out. All values of the image below a certain threshold h are assigned to one magnitude (e.g. white) and all values above that threshold to another magnitude (e.g. black) resulting in a data set A_h on which the opening can be applied. By successively varying the threshold limit h the image with varying magnitude is analyzed. Besides such a parameterization in magnitudes, a variation in the structuring set B — e.g. a filled circle with varying diameter C_d — can be applied. By subtracting two openings with circles C of varying diameter $d_1 < d_2$ as structuring elements

$$\triangle\,\mathcal{A}(h,d) = \mathcal{O}(A_h, C_{d_2}) - \mathcal{O}(A_h, C_{d_1}), \tag{C.6}$$

a measure of the area where the circle C_{d_1} but not the circle C_{d_2} “fitted in” is created. By successively varying threshold h of data set A_h and circle diameter d a comprehensive analysis of structure sizes is possible.

The digital implementation of this procedure was carried out by Fuhrmann [77] and has been applied to experimental data [78]. To illustrate the mathematical description figure C.2 shows the application of the opening procedure on an exemplary surface contour (figure C.2a) consisting of circular structures of different diameter and height. Figure C.2b shows the surface profile along the dotted line. When constructing the subset A_h of A a cut at a certain height h is made, which is successively scanned with circles C_d of growing diameter d. The remaining area $\mathcal{A}(h,d)$ is plotted versus diameter d and height h in figure C.2c. All structure sizes and heights are clearly identified. The light blue areas are due to aliasing effects, where surface topology and structuring set C_d didn’t match well.

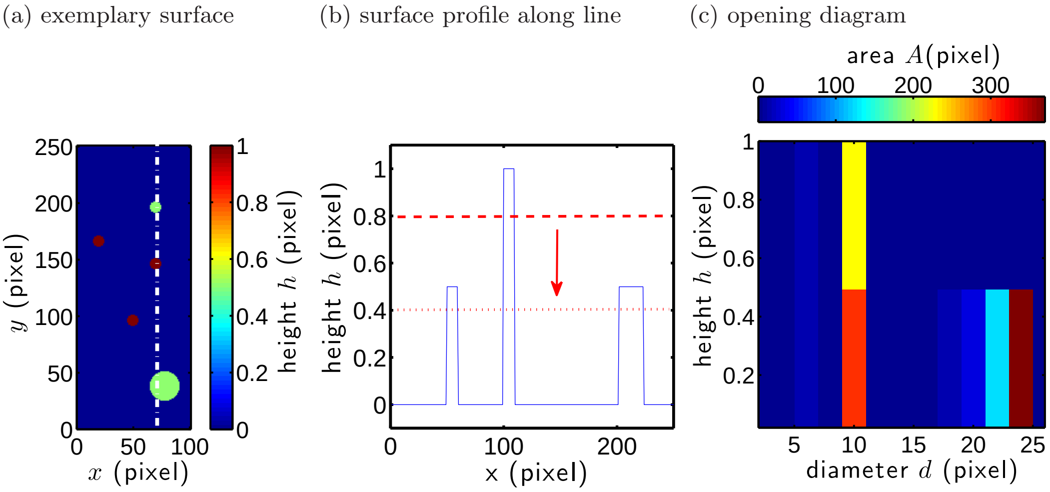
(a) exemplary surface
(b) surface profile along line
(c) opening diagram

Figure C.2.: Minkowski opening operation

D. Superposition of Photoluminescence Centers

To study the superposition of a laterally varying defect absorbance α_{def} the microscopic measured absorbance has been modeled with the sum of the absorption coefficients α_{id} for an ideal direct semiconductor, α_{urb} for an Urbach like tail and α_{def} for a gaussian shaped defect absorption according to $A(\hbar\omega) = 1 - exp[-(\alpha_{id} + \alpha_{urb} + \alpha_{def})d]$. The defect absorbance is defined by a gaussian defect "band"

$$\alpha_{def} = \alpha_{d0} \mathrm{e}^{-\left(\frac{\hbar\omega - \alpha_{dc}}{\sigma_d}\right)^2} \tag{D.1}$$

with α_{dc} as the center position, σ_d its width or standard deviation and α_{d0} its magnitude. Figure D.1 shows modeled (red) and measured (black) absorbance. Different cases of the superposition for a laterally varying absorbance have been studied. Case *a* corresponds to band-gap fluctuations (analogously to section 3.1.1) and is realized by a shift of the absorbance spectrum to higher or lower energies. Extend and occurrence of a certain shift are determined by a gaussian distribution function analogously to eq. (3.22). The macroscopic absorbance spectrum results from the

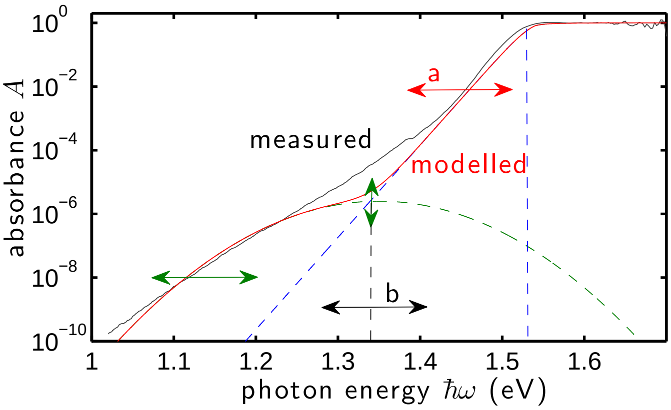

Figure D.1.: Modeled and measured absorbance A.

superposition of all microscopic absorbance spectra. To simulate different band-gap fluctuations $\triangle E_g$, different standard deviations σ_{E_g} for the distribution function have been used (see figure D.2a). A higher variation leads to an increase in tail and defect absorbance. The resulting PL spectra have — depending on the band-gap variations, represented by σ_{E_g} — an increased PL yield as shown in figure D.2b. Besides the band-to-band transitions analyzed before, the broad peak of defect absorbance increases and shifts together with the band-to-band peak to lower energies. The extend of this peak shift can not be determined exactly since it depends in particular on the underlying microscopic absorbance spectra.

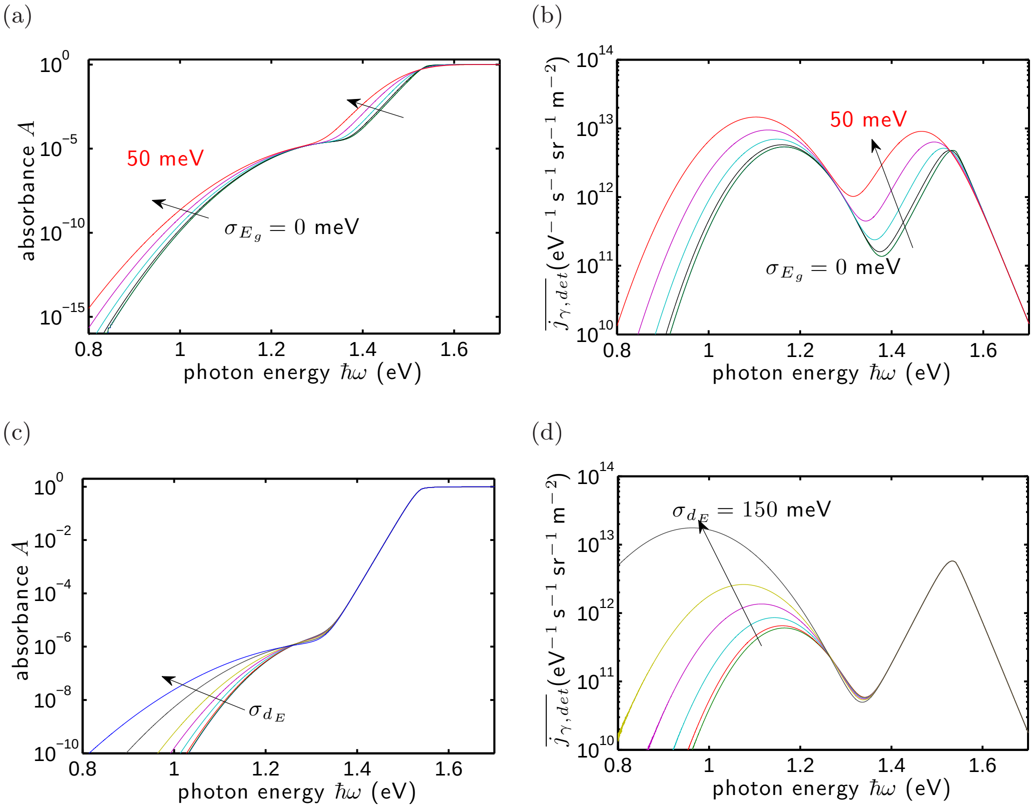

Figure D.2.: Superposition of a laterally varying defect absorbance.

In a second approach the center position α_{dc} of the defect absorption (eq. (D.1)) which corresponds to the energy of the deep defect states is varied analogously. Figure D.2c shows the resulting absorbance $\overline{A}$, with increasing variation $\sigma_{\alpha_{dc}}$ the absorbance in the lower energy range increases. Only for a substantial variation of

α_{dc} — which is beyond the fluctuations in the analyzed samples — a significant increase of luminescence $\overline{j_{\gamma,det}}$ in the lower energy range is found. This increase in $\overline{j_{\gamma,det}}$ goes along with a shift of the maximum in defect luminescence.

E. Angular Dependence of Macroscopic Photoluminescence

To verify that the angular dependence of macroscopic PL is not influenced by the surface roughness, the emitted PL has been measured for varying detection angles in the setup described in section 4.3. Sample excitation has been carried out perpendicular to the absorber surface. Figure E.1a shows the measured PL spectra for varying angles between excitation and detection. Due to low excitation fluxes

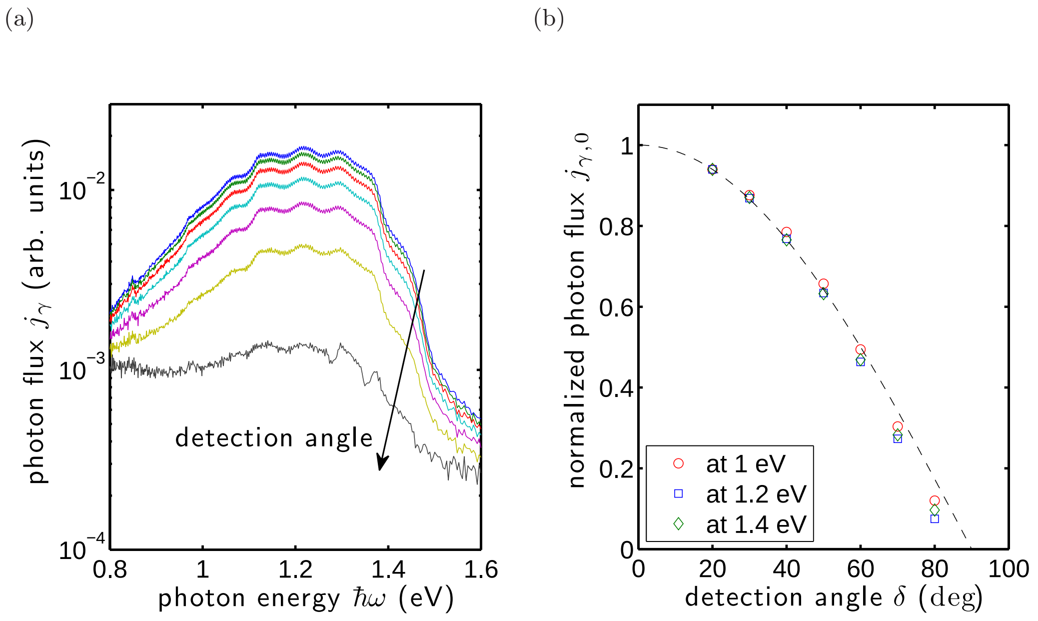

Figure E.1.: Angular dependence of the emitted photoluminescence , E.1a shows PL spectra for varying angles between excitation (perpendicular to the surface) and detection. E.1b shows the normalized PL yield of $\overline{j_{\gamma,0}}(1\,\mathrm{eV})$ (○), $\overline{j_{\gamma,0}}(1.2\,\mathrm{eV})$ (□) and $\overline{j_{\gamma,0}}(1.4\,\mathrm{eV})$ (◇).

and lower spectral sensitivity of the InGaAs detector towards higher photon energies only the defect related luminescence can be measured. The angular dependence of the spectral luminescence decreases according to Lambert's cosine law (dashed line in figure E.1b corresponds to $\cos\delta$). The labels in figure E.1b correspond to the normalized photon flux at 1 eV ($\bigcirc$), 1.2 eV ($\square$) and 1.4 eV ($\diamond$).

Erklärung

Hiermit versichere ich, dass ich diese Arbeit selbständig verfasst und keine anderen als die angegebenen Hilfsmittel benutzt habe.

Oldenburg, 29. September 2011

....
Florian Heidemann

Danksagung/Acknowledgements

An dieser Stelle möchte ich mich bei denen Bedanken, die mir diese Arbeit ermöglicht und mich dabei unterstützt haben. Dies gilt vor allem für meinen Betreuer und Doktorvater Gottfried H. Bauer, der immer ein offenes Ohr und Zeit für Diskussionen fand und mir wertvolle Anregungen für meine Arbeit geben konnte. Susanne Siebentritt möchte ich dafür danken, dass sie die Rolle der Zweitgutachterin übernommen und mich in der Endphase meiner Arbeit durch hilfreiche Gespräche und wertvollen Anregungen unterstützt hat. Unter den Mitgliedern der AG Greco möchte ich besonders Rudi Brüggemann für gute Tipps sowie den Blick aufs Detail und Peter Pargmann für seine schnelle Hilfe bei allen möglichen und unmöglichen Problemen sowie seine lockere Art bedanken. Was wäre eine Doktorarbeit wohl ohne die Unterstützung und den regen Austausch mit anderen Mitstreitern, deshalb auch ein besonderer Dank an meine Bürokollegen Levent Gütay und Sven Burdorf, den Mitdoktoranden Sebastian Knabe und Max Meessen sowie und alle anderen Mitglieder der Arbeitsgruppe Greco.

Für die Herstellung der Proben möchte ich ganz besonders Saoussen Merdes und Jo Klaer vom Helmholtz-Zentrum-Berlin danken, die auch versucht haben ausgefallenen Wünsche gerecht zu werden. Des weiteren Danke ich allen Partnern im Projekt KD-CIS sowie der finanziellen Unterstüzung durch das BMU (Projektnummer 0327589 C).

Neben diesen Menschen haben mich natürlich vor allem meine Freundin Gesche Fuhrmann — besonders in der Endphase der Arbeit — und meine Familie bei meinem Vorhaben unterstützt. Zu guter letzt Danke ich meinen Freunden und allen die hier zu kurz gekommen sind...

Lebenslauf

Florian Heidemann

geb. am 25. September 1979 in Dinklage, Deutschland
Staatsangehörigkeit: deutsch

Schulbildung & Zivildienst

28.06.1999	Abitur an der Helene Lange Gesamtschule, Oldenburg
10.1999 – 09.2000	Kindertagesstätte Philosophenweg, Oldenburg

Studium

01.10.2000	Begin mit dem Physikstudium (Diplom) an der Carl von Ossietzky (CvO) Universität Oldenburg
08.2003 – 01.2004	Universität von Lund, Schweden
03.2007	Diplom in Physik, Diplomarbeit: "Ortsabhängige Messung der Temperaturfluktuationen in turbulenten Strömungen"
10.2007 – 12.2010	Promotion, CvO Universität Oldenburg

Berufliche Tätigkeit

04.2007 – 06.2007	Wissenschaftliche Hilfskraft, CvO Universität Oldenburg
07.2007 – 09.2007	Wissenschaftlicher Mitarbeiter, Alfred-Wegener-Institut Bremerhaven
10.2007 – 01.2011	Wissenschaftlicher Mitarbeiter, CvO Universität Oldenburg
seit 05.2011	Forschung und Entwicklung, Soltecture GmbH Berlin

Oldenburg, 29. September 2011

....
Florian Heidemann